UNIVERSITY OF SOUTHAMPTON
Faculty of Engineering, Science and Mathematics
Optoelectronics Research Centre

Cathodoluminescence and Phase-change Functionality of Metallic Nanoparticles

by
Andrey Igorevich Denisyuk

A thesis submitted for the degree of
Doctor of Philosophy

April 2009

UNIVERSITY OF SOUTHAMPTON

ABSTRACT

FACULTY OF ENGINEERING, SCIENCE AND MATHEMATICS
OPTOELECTRONICS RESEARCH CENTRE

Doctor of Philosophy

CATHODOLUMINESCENCE AND PHASE-CHANGE FUNCTIONALITY OF METALLIC NANOPARTICLES

by Andrey Igorevich Denisyuk

Nanoscale resolution cathodoluminescence (CL) has been used to demonstrate and investigate the functionality of nanoparticle-based components for future nanophotonic phase-change memory and optical antenna applications.

An integrated experimental system based on a scanning electron microscope was developed for the fabrication and *in situ* characterization of nanoparticles. It was equipped with an atomic beam source for gallium nanoparticle growth, a liquid-nitrogen-cooled cryostat to control substrate temperature in the range from 90 to 315 K and a spectroscopic CL detection system to enable the analysis of electron-beam-induced light emission from nanoparticles across the wavelength range from 350 to 1150 nm.

A new technique of light-assisted, size-controlled growth of gallium nanoparticles from an atomic beam has been developed. Through coupling to surface plasmons in nanoparticles, infrared radiation controls the adsorption/desorption rate of gallium atoms on the particles' surface. The experiments revealed a decrease in mean particle diameter (from 68 to 45 nm) with increasing infrared excitation intensity (from 160 to 630 $W \cdot cm^{-2}$) during deposition, and the production of larger particles with a narrower size distribution for longer deposition times.

Gallium nanoparticle phase-change memory provides an important possibility to achieve small element size and low energy consumption. For the first time, it has been shown that information can be written into the structural phase of bistable gallium nanoparticles by electron beam excitation and readout achieved via measurements of their CL emission. Change of up to 20 % in CL emission intensity was observed following low fluence (≥ 35 fJ/nm^2) electron-beam-induced, solid-to-liquid phase switching of a monolayer of 60 nm particles. Selective electron beam addressing and CL readout of individual memory elements (comprising less than 50 particles each), within a gallium nanoparticle film, have been also demonstrated. Numerical modeling of CL emission from gallium nanoparticles, performed using the boundary element method, qualitatively reproduces the experimentally observed effects.

Optical antennae are expected to become essential elements of future nanophotonic circuits. For the first time, it has been demonstrated that electron-beam-excited pairs of coupled gold nanorods can act as transmitting optical antennae; *i.e.* they can efficiently convert the energy from a nanoscale excitation (created by a focused 40 keV electron beam) into far-field visible radiation. Enhanced light emission was observed for electron beam injection points in the vicinity of the junction between coupled nanorods, illustrating the increased local density of electromagnetic states in such areas.

Contents

Declaration of authorship

I, **Andrey Igorevich Denisyuk**

declare that the thesis entitled

Cathodoluminescence and Phase-change Functionality of Metallic Nanoparticles

and the work presented in the thesis are both my own, and have been generated by me as the result of my own original research. I confirm that:

- this work was done wholly or mainly while in candidature for a research degree at this University;
- where any part of this thesis has previously been submitted for a degree or any other qualification at this University or any other institution, this has been clearly stated;
- where I have consulted the published work of others, this is always clearly attributed;
- where I have quoted from the work of others, the source is always given. With the exception of such quotations, this thesis is entirely my own work;
- I have acknowledged all main sources of help;
- where the thesis is based on work done by myself jointly with others, I have made clear exactly what was done by others and what I have contributed myself;
- parts of this work have been published as:

  [1] A. I. Denisyuk *et al.*, Appl. Phys. Lett. **92**(9), 093112 (2008).

  [2] A. I. Denisyuk *et al.*, Jpn. J. Appl. Phys. **48**(3), 03A065 (2009).

Signed: ……..

Date:…….

Acknowledgements

I would like to thank my supervisor Professor Nikolay I. Zheludev for his guidance, assistance, and encouragement throughout my time as a research student.

I would like to express my gratitude to Dr. Fredrik Jonsson for being my co-supervisor during the first part of my study and Dr. Kevin MacDonald for being my co-supervisor during the rest of my study. The both were very helpful in guiding my initial steps as a research student. I would also like to thank my friend and colleague Dr. Bruno Soares who as a final year research student gave me some practical advice on my work.

I would like to acknowledge those with whom I worked in Southampton and at other institutions, in particular M. Bashevoy, F. J. García de Abajo, Z. Webber, G. Adamo, M. D. Arnold, M. J. Ford, Y. Chen, M. Scully, V. Fedotov, Z. L. Sámson, and R. Fisher. I would like to give a special thank to Dr. Eleanor Tarbox for her assistance in the preparation this thesis.

Furthermore, I would like to thank the technical and administrative staff at the School of Physics and Astronomy, and at the Optoelectronics Research Centre for all the help and assistance they have given to me over the years.

I would like to acknowledge the Overseas Research Students Awards Scheme, School of Physics and Astronomy, and Optoelectronics Research Centre for providing my maintenance grant.

Finally, I would like to thank all of my family for their support and encouragement, in particular my father for valuable advice and my wife Anna for waiting for me while I was away.

Chapter 1

Introduction

1.1 Synopsis

This introductory chapter explains the motivation for the work and the physics background that needs to be better understood.

Section 1.2 describes the motivation for probing the surface plasmon modes of metallic nanoparticles with nanoscale resolution cathodoluminescence, and introduces some ideas for nanoparticle-based nanophotonic devices, such as phase-change memory and optical antennae.

After this general introduction, Section 1.3 explains the optical properties of metallic nanoparticles, in particular the behavior of isolated particles of various shapes, pairs of closely-spaced particles and nanoparticle films. Section 1.4 introduces the principles of phase transitions and phase-change memory; it describes the thermodynamics of phase transitions in the cases of bulk materials and nanoparticles, and finally gives an overview of phase-change recording materials. Section 1.5 introduces electron microscopy and describes various electron-specimen interactions. A simple semi-empirical model of electron scattering in solid targets is presented as well. Section 1.6 details various mechanisms of electron-induced light emission. Methods for the calculation of light emission are also given. Finally, Section 1.7 concludes this chapter by giving an overview of the remaining chapters in the thesis.

1.2 Introduction

The earliest known optical element, dated as early as 700 BC, is the Assyrian Nimrud lens. This plano-convex lens, 35×41 mm across and 6 mm at its thickest, could have been used as magnifying glasses or to concentrate the sun's rays. Since that time optical science has made significant progress.

Future optical (or photonic) elements and devices, which are being developed nowadays, have a feature size in the range of nanometers. Since the optical properties of nanoscale elements are sufficiently different from bulk ones the new term "nanophotonics" has been introduced. Due to the small size, nanophotonics elements cannot be probed by far-field optical microscopy, which has the resolution limit of about 150 nm. A scanning near-field optical microscope (SNOM) is a more suitable tool, although its resolution of 20–30 nm (up to 12 nm after data processing [1]) may still not be enough. Truly nanoscale resolution (down to a few nanometers) can be achieved by means of an electron microscope. While cathodoluminescence (CL, the emission of light by a material stimulated by energetic electrons) is one form of analysis. This analysis has been used for more than forty years for studying semiconducting materials and minerals. High spatial resolution CL maps can be obtained using an electron microscope working in the scanning mode, the technique known as *scanning electron microscopy cathodoluminescence* (SEM–CL). Quite recently, this technique was applied to study metallic nanostructures, in particular nanoparticles* [2], whose light emission has a completely different nature than in semiconductors and is explained by the collective response of conduction electrons. The conduction electron response plays the major role in the optical properties of metallic nanoparticles. These electrons move away from their equilibrium position when perturbed by an external electric field, while the Coulomb attraction between the electrons and the positively charged ions creates the restoring force (Figure 1.1).

* Nanoparticles are particles that have sizes in the range between one and several hundreds of nanometers

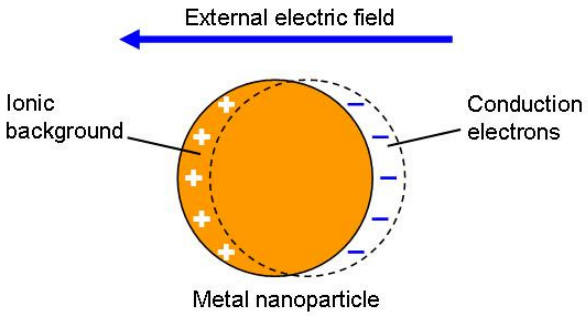

Figure 1.1. Schematic representation of a dipolar plasmon oscillation in a metallic nanoparticle.

The resulting conduction electron oscillations, the so-called *localized surface plasmons* (LSP), have a resonant character. For a spherical metallic nanoparticle in dielectric surroundings, the plasmon resonance occurs at the frequency for which the condition

$$\mathrm{Re}(\varepsilon_{int}) = -2\varepsilon_{ext} \tag{1.1}$$

is satisfied. Where ε_{int} and ε_{ext} are frequency-dependent dielectric functions of the nanoparticle and the surrounding medium, respectively. Localized surface plasmons in metallic nanoparticles can be effectively excited by incident light, if its frequency matches with the resonance frequency of the nanoparticles. The excited plasmons produce strong effects in the optical responses of a nanoparticle, such as dramatic increase of light absorption or an enhanced local field in the vicinity of the particle. High-energy electrons provide an alternative method for surface plasmon excitation, which causes light emission on the plasmon resonance frequency. Due to the electron beam's intrinsic ability to focus in the nanoscale range, SEM-CL analysis allows the study of the surface plasmon modes of metallic nanoparticles with nanoscale spatial resolution, which nowadays generates a great interest in this analytical tool.

The effects resulting from surface plasmons in metallic nanostructures have found numerous applications, such as plasmon waveguides, imaging, sensing, surface-enhanced Raman spectroscopy *etc* [3]. In this work just two potential applications of localized surface plasmons in metallic nanoparticles will be explored.

Consider that the dielectric function of a metallic nanoparticle changes by some mechanism, then the resonance condition (1.1) changes too. Thus, it is possible to effectively control the optical response of a nanoparticle and create a nanoscale optical switching device. A concept proposed in [4] suggests that such devices can be created by employing nanoparticles of metals (notable gallium) undergoing a light-induced transition between phases with different optical properties. Peculiarities of phase transitions in nanoparticles enable, under certain conditions, the achievement of either reversible or bistability phase switching. Thus, individual metallic nanoparticles can serve as key components of optical gates or memory elements [5].

Another idea emerges from the fact that a plasmon, localized on a metallic nanoparticle, creates a strong electromagnetic field near it surface. In the case of two closely-spaced nanoparticles, the field is concentrated in the gap between the particles. Thus, such a device, which is commonly called an "optical antenna", can efficiently couple the energy of free-space radiation to a confined region of subwavelength size. Optical antennae could be employed in single-molecule spectroscopy or as elements of future nanophotonic circuits [6].

In this work, SEM-CL is used to investigate the plasmonic properties of metallic nanoparticles with the aim to demonstrate the functionality of potential nanophotonic devices:

1. Gallium nanoparticle phase-change memory, where the addressing is achieved by the electron beam and readout is performed by measuring the particles' CL response (Chapter 3). The gallium nanoparticle growth process is studied as well (Chapter 2).
2. A transmitting optical antenna based on gold nanorods, which effectively converts the energy of a nanoscale source of excitation created by the electron beam to far-field radiation detected by means of CL (Chapter 4).

In order to perform this task an integrated experimental setup, based on a scanning electron microscope, was developed (Chapter 2). In the remaining part of this chapter the physics background of the effects that are briefly discussed above is presented in more detail.

1.3 Optical properties of metallic nanoparticles

1.3.1 Single and coupled nanoparticles

Optical behaviors of small particles are discussed in many sources [7, 8]. Since the introduction to the optical properties of metallic nanoparticles has been given in the previous section, this subsection details these properties.

The dipole moment of a nanoparticle, placed in a homogeneous electric field $\mathbf{E}_{ext}$, is defined as

$$\mathbf{p} = \varepsilon_0 \varepsilon_{ext} \alpha \mathbf{E}_{ext} \tag{1.2}$$

where ε_0 is the dielectric permittivity of a vacuum, ε_{ext} the dielectric constant of the surrounding medium, while α is the dipolar polarizability of the particle which has the dimension of volume. The polarizability of a particle depends on its size, shape, and the dielectric functions of the particle and the surrounding medium, ε_{int} and ε_{ext} respectively. An analytical solution for polarizability in the electrostatic limit can be found for a number of shapes. For instance a *spherical particle* with a radius *a* has dipolar polarizability that is defined by

$$\alpha = 4\pi a^3 \frac{\varepsilon_{int} - \varepsilon_{ext}}{\varepsilon_{int} + 2\varepsilon_{ext}} \tag{1.3}$$

The plasmon resonance is given by the zero of the denominator. If the surrounding medium is dielectric (ε_{ext} is real) then the condition for the resonance is defined by Expression (1.1).

The dipolar polarizability of an *ellipsoidal particle* with radii *a*, *b* and *c* along one of the principal axes *j* is given by

$$\alpha_j = 4\pi abc \frac{\varepsilon_{int} - \varepsilon_{ext}}{3\varepsilon_{int} + 3L_j(\varepsilon_{int} - \varepsilon_{ext})} \tag{1.4}$$

where L_j is the depolarization factor (in the case of a *sphere* $L_j = 1/3$). Since in the general case L_j is different for different axes, an ellipsoid will have three dipolar resonances. A spheroid (ellipsoid with axis symmetry) has just two dipolar resonances because L_j takes different values for its major and minor axes. A simple analytical solution for L_j can be found for spheroids.

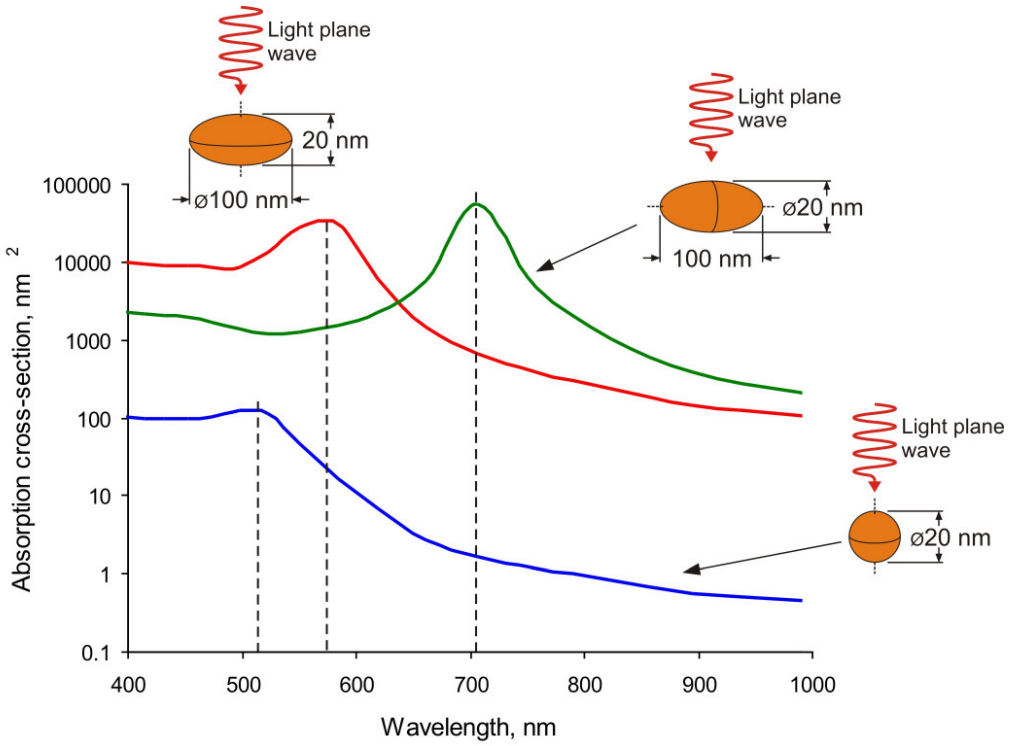

Figure 1.2. Absorption cross-section of gold nanoparticles for incident linear polarized light: spherical particle (blue line), oblate (red line) and prolate (green line) spheroids. The polarization plane of light is parallel to the major axes of the spheroids.

In the case of an *oblate spheroid* (with radii $a = b > c$, aspect ration $\gamma = a/c$) the depolarization factor along the major axes is

$$L_{a,b} = \frac{\gamma^2}{2\sqrt{(\gamma^2-1)^3}}\left[\frac{\pi}{2} - \frac{\sqrt{\gamma^2-1}}{\gamma^2} - \arctan\left(\frac{1}{\sqrt{\gamma^2-1}}\right)\right] \qquad (1.5)$$

In the case of a *prolate spheroid* or a *rod* (with radii $a > b = c$) the depolarization factor along the major axis (rotation axis) is

$$L_a = \frac{1-e^2}{e^2}\left[-1 + \frac{1}{2e}\ln\left(\frac{1+e}{1-e}\right)\right], \qquad e^2 = 1 - \frac{b^2}{a^2} \qquad (1.6)$$

The dipolar contribution to the absorption cross-section of a particle can be obtained from the polarizability α by the following expression:

$$\sigma_{abs} = \frac{2\pi\sqrt{\varepsilon_{ext}}}{\lambda}\mathrm{Im}(\alpha) \qquad (1.7)$$

Using the above expressions, the absorption cross-section was calculated for gold nanoparticles of spherical and spheroidal (oblate and prolate) shapes for a polarization of the incident light wave parallel to the major axes of the spheroids (Figure 1.2). The resonance wavelength is the one where the absorption cross-section of a particle reaches its maximum. Thus, it can be seen that the resonance wavelength of the spheroidal nanoparticles is redshifted in comparison with the spherical one, and the resonance of the prolate particle exhibits a stronger redshift than the oblate one with the same aspect ratio.

Dipolar plasmons in metallic nanoparticles are just the simplest type of localized surface plasmons. Multipole plasmons in nanoparticles will be considered for the example of nanorods, since the latter are cases of study in this work (see Chapter 4). Firstly, another type of plasmon, called *surface plasmon polaritons* (SPP) will be introduced, that will be useful for the interpretation of localized multipole plasmons in nanorods [9].

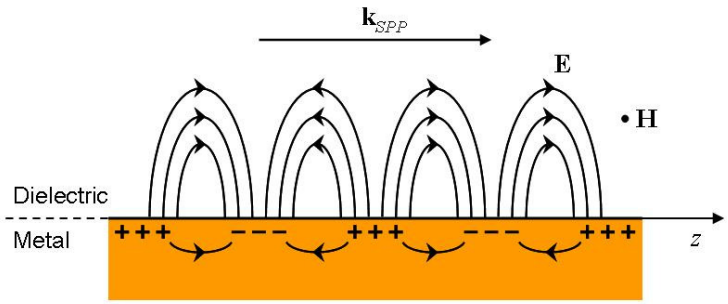

Figure 1.3. Schematic representation of a surface plasmon polariton (SPP) propagating along a metal–dielectric interface.

An SPP is a collective electron excitation at an interface formed by a metal and a dielectric (or vacuum), as schematically shown in Figure 1.3. This excitation can be interpreted as an electromagnetic wave (photon) which is trapped at the interface because of the presence of electrons provided by the metal. The result of photon-plasmon coupling is a quasiparticle called a polariton. This polariton propagates along the metal/dielectric interface until it decays. An SPP is

characterized with a wave vector and frequency, since the SPP dispersion relation $\omega = \omega(k)$ is nonlinear.

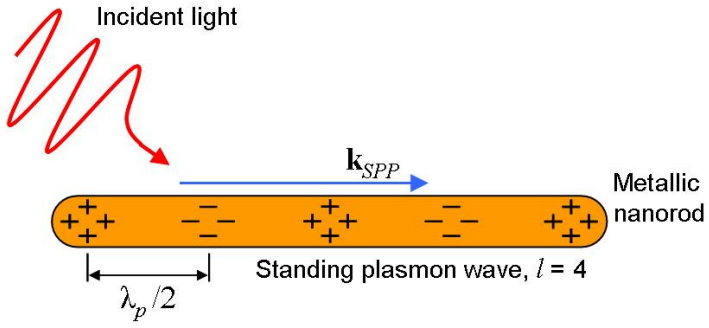

Figure 1.4. Schematic of the excitation of localized multipole plasmons (standing plasmon wave) in a metallic nanorod by P-polarized light at oblique incidence.

Multipole plasmons in metallic nanorods can be excited by P-polarized light at oblique incidence (Figure 1.4). In this case, the *x*- and *z*-components of the light wave's electric field effectively perturb electrons across and along the nanorod, thus inducing all kinds of possible electron oscillations. The result can be interpreted in terms of SPP waves propagating along the rod. However, due to the confined pass (length of the rod) the SPPs form a standing plasmon wave with the wavelength λ_p defined by the condition:

$$L = l\frac{\lambda_p}{2} \tag{1.8}$$

where l is the mode number (integer) and L is the length of the rod. The SPP wave number is then defined as $k_{SPP} = 2\pi/\lambda_p$, while the SPP frequency is equal to the frequency of the incident light.

The concept of standing plasmon waves explains well the behavior of localized multipole plasmons in a nanorod. Figure 1.5 shows the absorption cross-section of a gold nanorod for P-polarized light at 30º incidence. In this configuration, all kinds of localized surface plasmons, that are possible for this nanorod, are excited. The plasmon resonances define the maxima of absorption cross-section. Note that the longitudinal dipolar mode ($l = 1$) is the strongest.

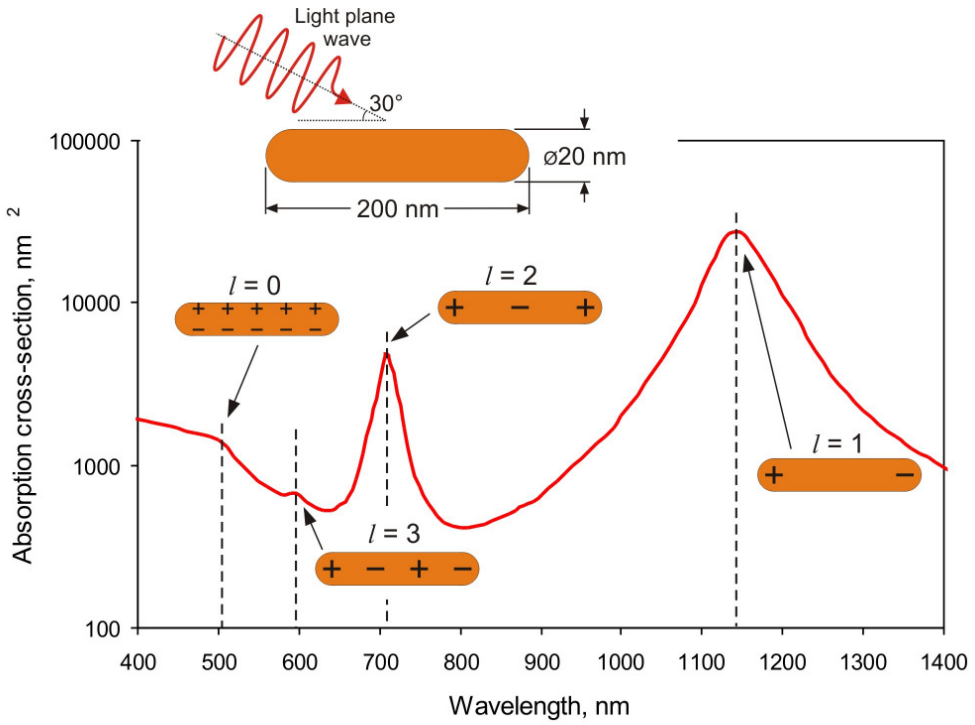

Figure 1.5. Absorption cross-section of a gold nanorod for P-polarized light at oblique incidence. In this configuration all kinds of localized plasmons (possible in this nanoparticle) are excited: dipolar transverse ($l = 0$), dipolar longitudinal ($l = 1$) and multipole plasmons ($l = 2$ and $l = 3$). The calculation is performed by the boundary element method (described in Subsection 1.6.3).

At the resonance frequency, the longitudinal dipolar plasmon in a nanorod creates a strong local electromagnetic field at the tips of the particle (see Figure 1.6a). The enhancement factor of the local field reaches 10–100. If there are two nanorods, whose tips are separated by a nanometer size gap, then the opposite charges are strongly localized to the ends of the rods at the gap (Figure 1.6b). This causes the enhancement factor of the local field in the gap to become as high as 10^3–10^4. In contrary, the charge at the outside ends of the rods is drawn closer to the gap, thus weakening the Coulomb restoring force inside each particle. This gives rise to a redshift of the plasmon resonance of the closely-spaced nanorods in comparison to the case of an isolated one. The localized surface plasmons of such closely-spaced rods are coupled; therefore, the nanorods are commonly called *coupled nanorods* [10, 11].

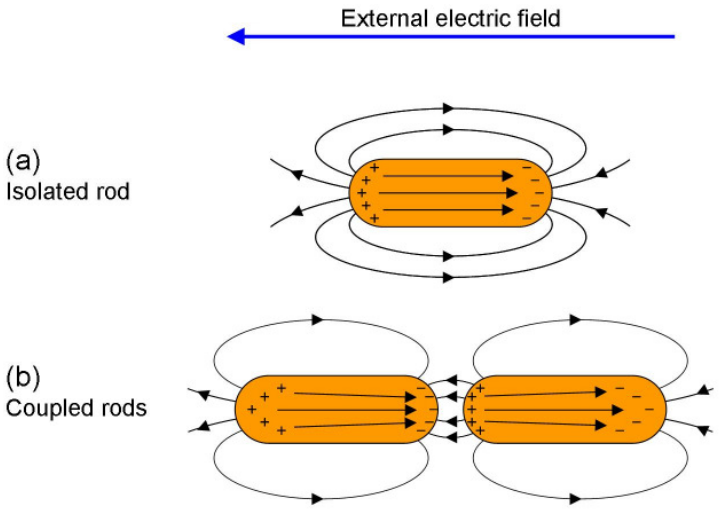

Figure 1.6. Schematic illustration of the polarization charges and electric fields of an isolated nanorod (a) and coupled nanorods (b). Following Aizpurua *et al.* [10] and Dahmen and von Plessen [11].

1.3.2 Nanoparticle arrays

Nanoparticle arrays embedded in a homogeneous matrix, or distributed on a surface, present effective properties which are a function of the component materials, filling fraction, particle size and shape and spatial distribution. The effective medium theory, developed by J. C. Maxwell-Garnett, gives effective optical properties for a three-dimensional distribution of spherical particles [12]. The theory for two-dimensional nanoparticle arrays (films) has been developed by T. Yamaguchi *et al.* for the case of disperse particles [13, 14] and quite recently extended to the case of closely packed particles by V. A. Fedotov *et al.* [15]. Here, both models are considered briefly.

Disperse nanoparticle film

A monolayer is composed of small spheroidal particles, with a radius r and height h, each distributed on the surface of a transparent substrate of dielectric constant ε_{sub} (Figure 1.7). Dielectric constants of the particles and the surrounding medium are ε_{int} and ε_{ext}, respectively. The dipole moment of each particle p and its mirror

image p', induced by the electric field of the incident wave parallel to the substrate, are connected to each other by

$$p' = -\frac{\varepsilon_{sub} - \varepsilon_{ext}}{\varepsilon_{sub} + \varepsilon_{ext}} p \tag{1.9}$$

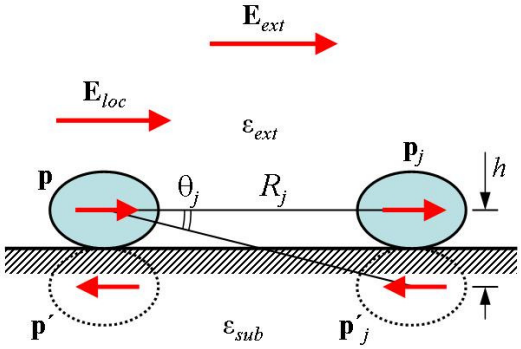

Figure 1.7. Schematic illustration of the dipole moment of a particle lying on a substrate surface, its mirror image and the dipoles of a neighboring particle and its image. After Fedotov *et al.* [Fedotov2004].

The local field acting on each particle, E_{loc}, is the sum of the applied external field, E_{ext}, and the additional fields (E_{img} and E_{sur}) produced by the image dipole, p', and by the dipoles and their images of the surrounding particles, p_j and p'_j:

$$E_{loc} = E_{ext} + E_{img} + E_{sur} \tag{1.9}$$

Dipole moments, and their images, of the surrounding particles are found by the assumption that the nanoparticle film is dispersed, *i.e.* $R_j >> h$ and $\theta_j \cong 0$. Then the dielectric constant, ε_{eff}, of a plane-parallel film (effective medium) equivalent to a monolayer of spheroidal nanoparticles is defined by:

$$\left(\varepsilon_{eff} - \varepsilon_{ext}\right) E_{ext} = q \frac{\varepsilon_{int} - \varepsilon_{ext}}{\varepsilon_{ext} + L\left(\varepsilon_{int} - \varepsilon_{ext}\right)} E_{loc} \tag{1.10}$$

where q is the packing factor of the particles, defined as $q = V / l^2 h$: V is the volume of each particle and l is the lattice constant of the nanoparticle film. The expression for L can be found from the equations presented in the previous section

for oblate (1.5) or prolate (1.6) spheroidal particles. Finally, the expression for the effective dielectric constant of the nanoparticle monolayer is defined as

$$\varepsilon_{eff} = \varepsilon_{ext}\left(q\frac{\varepsilon_{int}-\varepsilon_{ext}}{\varepsilon_{ext}+F\left(\varepsilon_{int}-\varepsilon_{ext}\right)}+1\right) \tag{1.11}$$

where the geometrical factor F is given by:

$$F = f+\varepsilon_0\varepsilon_{ext}\beta = f-\frac{\gamma^2}{24}\frac{\varepsilon_{sub}-\varepsilon_{ext}}{\varepsilon_{sub}+\varepsilon_{ext}}-0.719\left(\frac{6}{\pi}\right)^{1/2}\frac{\varepsilon_{ext}}{\varepsilon_{sub}+\varepsilon_{ext}}q^{3/2} \tag{1.12}$$

Closely packed nanoparticle film

The field produced by a uniformly polarized spheroid is equivalent to the field of a point dipole placed in the centre of the spheroid only at distances that are larger compared to the size of spheroid. This becomes especially noticeably as the shape of a fixed volume particle deviates from that of a sphere (aspect ratio increases). The major improvement of the model described in [15] is the replacement of the point dipole approximation by a more accurate one, which takes into account the exact local field of a spheroidal nanoparticle on a substrate. This led to the introduction of a modified effective geometrical factor:

$$F = f-\sum_{j=-2}^{2}\sum_{k=-2}^{2}A\left(j\sqrt{\frac{2\pi}{3q}},k\sqrt{\frac{2\pi}{3q}},0\right)-$$

$$-\frac{\varepsilon_{ext}-\varepsilon_{sub}}{\varepsilon_{ext}+\varepsilon_{sub}}\sum_{j=-2}^{2}\sum_{k=-2}^{2}A\left(j\sqrt{\frac{2\pi}{3q}},k\sqrt{\frac{2\pi}{3q}},\frac{2}{\gamma}\right)-\frac{2\varepsilon_{ext}}{\varepsilon_{ext}+\varepsilon_{sub}}\frac{0.177}{\gamma}\sqrt{\frac{3q^2}{2\pi}} \tag{1.13}$$

The expression for $A(x,y,z)$ is not presented because of its complexity. Expression (1.13) accurately accounts for the interaction of the nanoparticle (see Figure 1.8) with 24 nearest neighbors (second term) and their images and the image of the central particle itself (third term). The effect due to the rest of the particle film is accounted for by using the point dipole approximation (fourth term). The effective dielectric constant of the nanoparticle monolayer can then be found by the expression (1.11).

Once the effective dielectric constant is obtained by any of the two models, the particle layer can be treated as a plane-parallel film of thickness h and

its reflectance, transmittance and absorption can be calculated using standard thin film formulae [15].

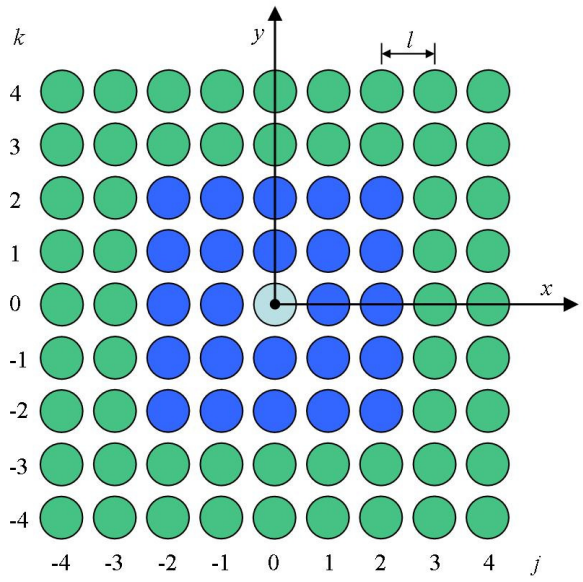

Figure 1.8. Square lattice of nanoparticles on the surface of a substrate. The exact fields from the central particle (light blue circles) mirror image and 24 nearest neighbors (dark blue circles) and their mirror images are calculated, while the contribution from the rest of the particles (green circles) and their images are taken into account by using the dipole approximation. After Fedotov *et al.* [15].

1.4 Phase-change functionality

1.4.1 Principles

Phase transition is the transformation of matter from one phase to another. In other words, it is a discontinuous (or continuous) change of some physical properties of the material (density, refractive index, permeability *etc*) due to a continuous change of external conditions (such as temperature, pressure *etc*). An example of such a transition is the transformation of ice to water (melting) or the opposite process (freezing). In this example the transition occurs between different states of matter (*i.e.* solid and liquid). However phase transitions are also possible within the same state of matter. For instance, if a solid exists in more that

one crystal form (such ability is called *polymorphism*) then the phase transition can occur between different crystalline structures (*structural phase transition*).

Phase transitions are usually divided into the transitions of *first order* and *second order*. First order phase transitions are those that involve a latent heat, a fixed amount of energy released or absorbed by the material during the transition. Classical examples are melting and freezing. Second order phase transitions have no associated latent heat. An example is the transition between ferroelectric and paramagnetic phases. However, the distinction between first and second order transitions disappears in some cases of structural transformations, in particular the transition in clusters (particles comprised of ten to a few hundreds of atoms) [16].

The idea of using the difference in the properties of a material undergoing a phase transition for memory applications was first developed in the 1960s by S. Ovshinsky [17]. In particular, it was demonstrated that differences in resistivity between the crystalline and amorphous phases of chalcogenide glass could be used to create memory devices. This idea was later extended to optical data storage where differences in optical properties are used for data readout.

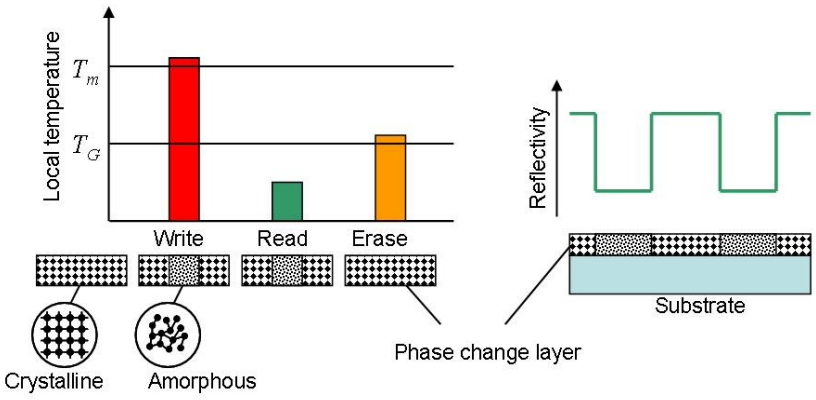

Figure 1.9. Schematic of a write-read-erase memory cycle with phase-change media. After Waser [18].

The principle of phase-change recording is schematically shown in Figure 1.9. To write a bit, an intense laser (or current pulse) heats and melts a local volume of the crystalline material. After the heat source is turned off, this molten material cools rapidly (cooling time of a few nanoseconds) and solidifies (or

'freezes') into a metastable amorphous state. To switch the material back into the crystalline state, a longer but less intense pulse heats the material above the glass transition temperature, thus the bit is erased. Readout of the recorded information is performed with light (or electric) pulses of much lower intensity.

1.4.2 Thermodynamics of phase transitions

Phase transitions in bulk materials

Thermodynamics of phase transitions in bulk materials will be considered by the example of transitions in a phase-change recording medium following [18]. A phase transition can proceed if it reduces the Gibbs free energy (G) of the system. Therefore the driving force of a phase transition is the difference (ΔG) of the Gibbs free energy of the two phases. The phase transitions are accompanied with the change of enthalpy ΔH (latent heat, absorbed or released by the system) and the change of entropy ΔS (the change of ordering of the system). So at a constant temperature, T, the change of Gibbs free energy during the phase transition is defined as:

$$\Delta G = \Delta H - T\Delta S \tag{1.14}$$

For $\Delta G < 0$ the transition is favored, for $\Delta G > 0$ it is not, and for $\Delta G = 0$ the system is in equilibrium. Gibbs free energy itself is determined by:

$$G = H - TS \tag{1.15}$$

For a given phase the temperature dependence of the enthalpy and the entropy can be neglected. The temperature dependence of the Gibbs free energy of a material with a crystalline, liquid and amorphous phase is shown in Figure 1.10, where T_m is the melting point and T_G is the glass transition temperature.

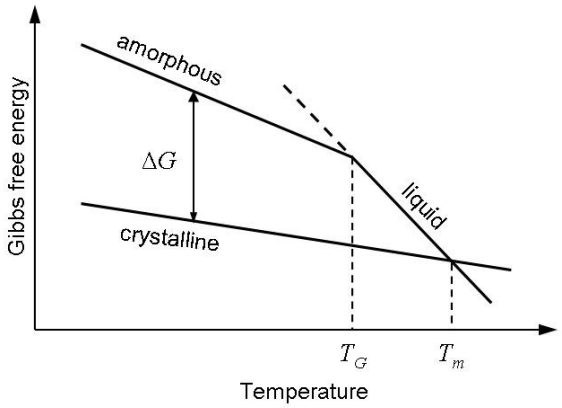

Figure 1.10. Schematic representation for the temperature dependence of the Gibbs free energy for a material in crystalline, amorphous and liquid phases. After Waser [18].

At the melting point $\Delta G = 0$ and hence $T_m = \Delta H / \Delta S$, where ΔH is the latent heat of melting. Therefore the driving force for the crystalline-to-liquid transition in the material is:

$$\Delta G = \Delta H \frac{T_m - T}{T_m} \tag{1.16}$$

For the amorphous-to-crystalline (crystallization) transition two situations are possible. For $T > T_G$ the driving force is:

$$\Delta G = \Delta H \frac{T_m - T}{T_m} \tag{1.17}$$

While for $T \leq T_G$ it is:

$$\Delta G = \Delta H_{ac} \left[1 - \frac{T}{T_G} \left(1 - \frac{\Delta H}{\Delta H_{ac}} \frac{T_m - T_G}{T_m} \right) \right] \tag{1.18}$$

where H_{ac} denotes the exothermic energy of transformation from the amorphous to crystalline phase.

The opposite process (crystallization) however requires the formation of crystallites (nucleation) in a previously amorphous (or liquid) surrounding. To create a nucleus of a different phase it is necessary to supply not only the energy difference ΔG, but also the energy to produce the phase boundary ΔG_{IF}. So the total energy change is:

$$\Delta G_{total} = \Delta G(T) + \Delta G_{IF} \tag{1.19}$$

The first term in Expression (1.19) is proportional to the volume V of the nucleus, while the second one is proportional to its surface area, A, so ΔG_{total} can be written as:

$$\Delta G_{total} = \Delta G_V(T) \cdot V + \sigma \cdot A \tag{1.20}$$

where $G_V(T)$ is the temperature dependent Gibbs free energy per volume and σ the surface tension. Thus ΔG_{total} for a spherical nucleus with radius r is:

$$\Delta G_{total} = \Delta G_V(T) \cdot \frac{4}{3}\pi r^3 + \sigma \cdot 4\pi r^2 \tag{1.21}$$

Figure 1.11 shows the dependence of ΔG_{total} upon the radius r of the nucleus for different temperatures.

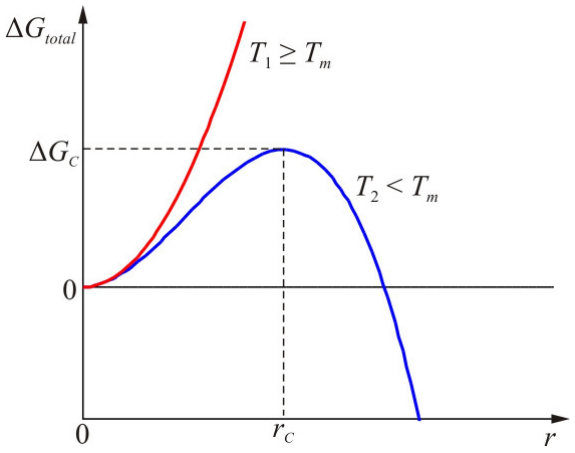

Figure 1.11. Dependence of the total Gibbs free energy ΔG_{total} necessary to create a nucleus of radius r for the temperatures above and below the melting point. After Waser [18].

For $T \geq T_m$ the creation of a stable nucleus is impossible since ΔG_{total} monotonically increases with r. Whereas for $T < T_m$ ΔG_{total} is non-monotonic and reaches the maximum ΔG_c at the critical radius r_c:

$$r_c = -\frac{2\sigma}{\Delta G_V} \tag{1.22}$$

and

$$\Delta G_c = \frac{16}{3}\pi \cdot \frac{\sigma^3}{\Delta G_V^2} \tag{1.23}$$

Therefore ΔG_c reflects an energy barrier that must be overcome to create a critical nucleus (with $r = r_c$) and proceed with crystallization. While crystallization may happen at any $T < T_m$ the process is subject to probability which is proportional to $\exp\left[-\left(W_A + \Delta G_c\right)/kT\right]$, where kT is the thermal energy. W_A represents the activation barrier for an atom to cross the interface between phases and join a crystalline nucleus. Therefore at room temperature ($T << T_G$) the ratio $\left(W_A + \Delta G_c\right)/kT$ becomes high and the probability of crystallization is low, thus the recorded data stability can be achieved.

Phase transitions in nanoparticles

For particles with the size of less than 100 nm (nanoparticles) the ratio of the number of surface to volume atoms is not small and therefore the effects of the surface on the properties of the particle cannot be neglected. The surface is a location for defects of a crystalline structure, since the atomic bonds are broken. Hence, the transitions from a high order phase (crystalline) to a low order phase (liquid) will start from the transformation of the surface and proceed inside the particle. This leads to size dependent melting point depression in small particles. The reverse phase transition requires the creation of crystalline nuclei. Since the volume of a nanoparticle is limited, the probability of nucleation is lower than in bulk. Thus, the reverse transition will only occur after sufficient overcooling and a thermal hysteresis appears as a result.

Before considering thermodynamic models of phase transitions, it is important to specify the smallest size of a nanoparticle for which a thermodynamical description remains valid and atomic cluster behaviors do not take over. Theoretical analysis [19] suggests that a particle should consist of at least 1000 atoms. This means that, for instance, the overall diameter of a gallium nanoparticle should be larger than 3–4 nm.

The thermodynamic model of melting, considered in [20], describes the Gibbs free energy for a nanoparticle of N atoms as:

$$NG = NG_{\infty} + fN^{2/3}\gamma \tag{1.24}$$

where f is a geometrical factor depending on the shape of a particle, γ is the surface energy related to one atom (γ remains nearly constant when temperature varies). The term $fN^{2/3}$ is equal to the number of surface atoms. G and G_{∞} are the nanoparticle and the bulk Gibbs free energies per atom, respectively.

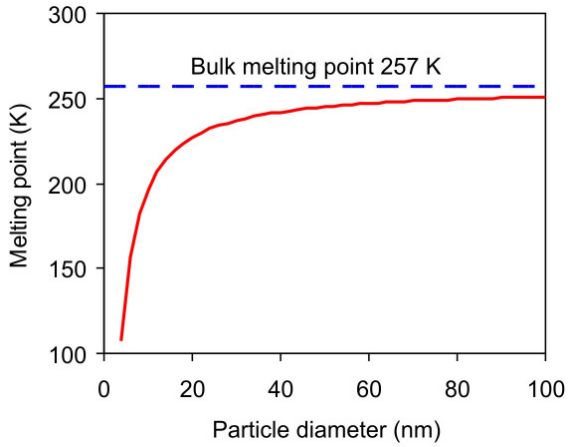

Figure 1.12. Dependence of melting point of a gallium nanoparticle on its diameter.

At a fixed temperature, the change of Gibbs free energy of a particle during the process of melting is defined as:

$$N \cdot \Delta G = N \cdot \Delta G_{\infty} + f \cdot N^{2/3}\Delta\gamma \tag{1.25}$$

The melting point is calculated by taking $N\Delta G = 0$. By inserting Expression (1.14), which defines ΔG_{∞}, into (1.24) the expression for the melting temperature of a nanoparticle is obtained:

$$T_m = T_{m,\infty} + \frac{f \cdot \Delta\gamma}{\Delta S \cdot N^{1/3}} \tag{1.26}$$

where $T_{m,\infty}$ is the bulk melting temperature of the material. The term $f/N^{1/3}$ is directly proportional to the ratio of surface to volume atoms. Therefore expression (1.26) can be rewritten as:

$$T_m = T_{m,\infty} + \frac{A}{d} \tag{1.27}$$

The melting temperature depression for a nanoparticle is $\Delta T_m = A/d$, where d is the diameter of the particle and A is a constant for a given material. For instance, in the case of gallium nanoparticle melting (the transition from β-solid to liquid phase) $A \cong 600\ \mathrm{K \cdot nm}$ [21]. The dependence of melting point of a gallium nanoparticle on its size is shown in Figure 1.12.

The previous reasoning was based on the assumption that there is no phase separation and segregation. In fact, this is not justified in the case of a nanoparticle where phase separation takes place, for example by obtaining a core-shell structure. The thermodynamics of the transition between some the low temperature phase (phase '0') and the high temperature phase (phase '1') in a spherical nanoparticle with radius R (volume $V = \frac{4}{3}\pi R^3$) is considered following the reasoning in [20]. Initially, the single phase '1' occupies the entire particle at high T. During the decrease of T, the nucleus of the new phase '0' with radius r (volume $V_n = \frac{4}{3}\pi r^3, \quad r < R$) appears inside the particle. In the case of a nanoparticle the effect of depletion of volume $(V_0 - V_n)$ of the parent phase '1' with the formation and growth of the nucleus of a new phase '0' cannot be neglected. The expression for the change of the Gibbs free energy for a nanoparticle undergoing the phase transition can then be written as

$$\Delta G_{total} = \Delta G_{V,n}(T) \cdot V_n + \Delta G_{V,p}(T,r) \cdot (V - V_n) - \Delta G_V(T) \cdot V + \sigma \cdot 4\pi r^2 \tag{1.28}$$

The expression shows that the formation of the core of the new phase '0' (term 1) and the shell of the parent phase '1' (term 2) occurs from the parent phase '1' initially occupying the entire particle (term 3). The term 4 accounts for the energy to produce the phase boundary (where σ is the surface tension). $\Delta G_{V,n}(T)$, $\Delta G_{V,p}(T,r)$ and $\Delta G_V(T)$ are the temperature dependent Gibbs free energies per volume of the new core phase '0', parent shell phase '1' and parent initial phase '1', respectively, note that $\Delta G_{V,p}(T,r)$ also depends on the nucleus radius r.

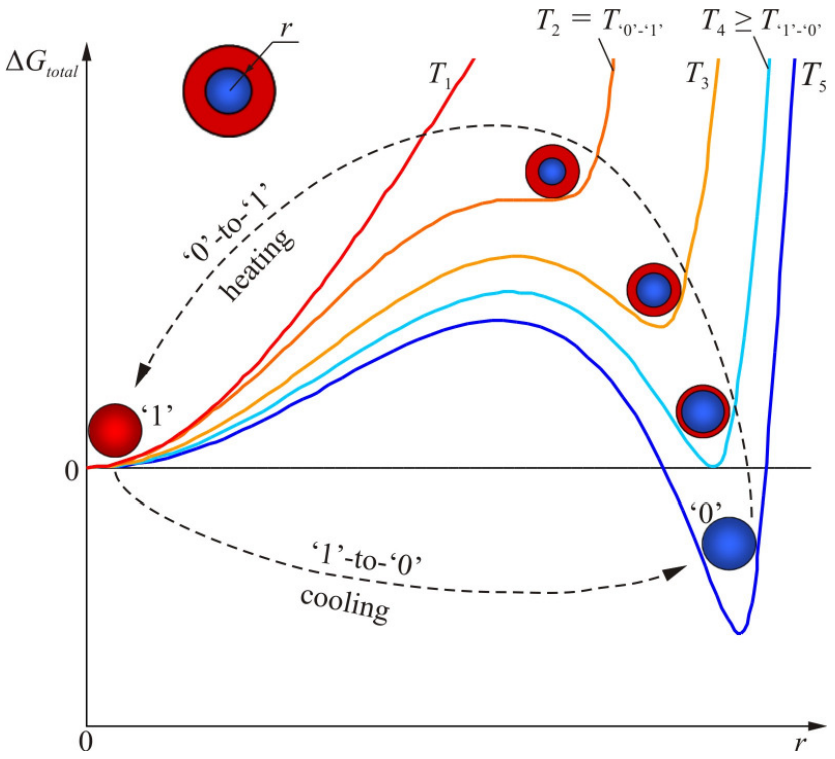

Figure 1.13. Dependence of the total Gibbs free energy ΔG_{total} necessary to create a nucleus of radius r in a nanoparticle for a set of temperatures. Following Shirinyan and Wautelet [20].

Figure 1.13 shows the dependence of ΔG_{total} for a particle upon the radius r of the nucleus for a set of temperatures (it can be compared with Figure 1.11 for bulk). At the temperature T_1 the particle is fully occupied by the phase '1'. At this temperature the ΔG_{total} monotonically increases with r, thus no stable nucleus of the new phase '0' can be formed. During the decrease of T, the dependence of ΔG_{total} on r changes to the non-monotonic curves with one maximum and two minima (curves T_3 – T_5). Of particular importance is the situation at T_4. This corresponds to the separation limit. Any further decrease of temperature leads to $\Delta G_{total} < 0$ for $r > 0$ thus the transition to '0' phase becomes favorable (in fact the phase '0' will occupy the core with radius r, which is covered with the shell of phase '1'). Therefore, at the temperature T_4, or lower, '1'-to-'0' phase transition can occur.

If the nanoparticle is in the phase '0' (covered with the shell of phase '1') at low T ($T = T_5$), during the temperature increases the volume of phase '0' decreases, while the volume of shell of phase '1' increases. The energy barrier prevents the core from being consumed by the phase '1'. Nevertheless, at T_2, the barrier disappears and the transition will take place. The temperature T_2 is the temperature of '0'-to-'1' phase transition ($T_{\text{'0'-'1'}}$).

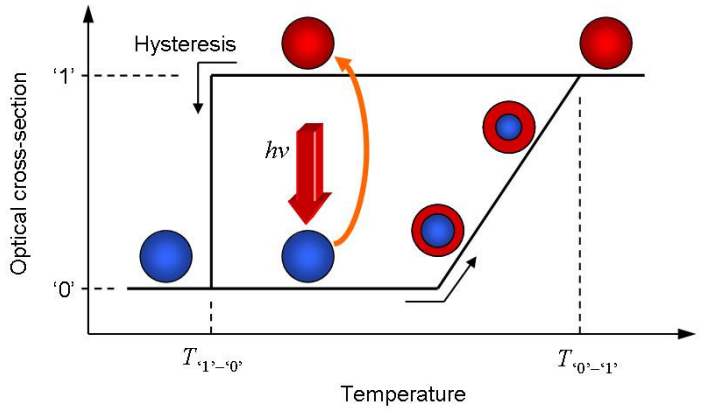

Figure 1.14. Dependence of optical cross-section on temperature for a nanoparticle undergoing a phase transition between phases '0' and '1' (Schematic based on experimental work [22]). The phase transition '0'-to-'1' can be induced by external optical energy excitation, thus providing a way for nanoparticle phase-change memory functionality (see Chapter 3).

Note that the temperature of the reverse phase transition $T_{\text{'1'-'0'}}$ is lower then the temperature of the straight phase transition $T_{\text{'0'-'1'}}$. So the phase transitions in nanoparticles are characterized by a thermal hysteresis and in the temperature region $T_{\text{'1'-'0'}} < T < T_{\text{'0'-'1'}}$ both phases are stable. If the two phases involved possess different optical properties, the phase bistability provides the basis of nanoparticle memory functionality (Figure 1.14): a phase transition can be induced by external optical energy excitation and readout achieved by optical methods.

1.4.3 Phase-change materials

Conventional materials: chalcogenide glass

Nowadays chalcogenide glass (most often Ge-Sb-Te alloys), undergoing a reversible transformation between the crystalline and amorphous state, is commonly used as an active medium in phase-change data storage. A rewritable storage medium has to fulfill five main data storage requirements. It has to enable writing of data (*writability*). The recorded information has to be stable (*archival storage*) and readable (*readability*). The information should be erasable (*erasability*) and the material should allow numerous write/erase cycles (*cyclability*) [18].

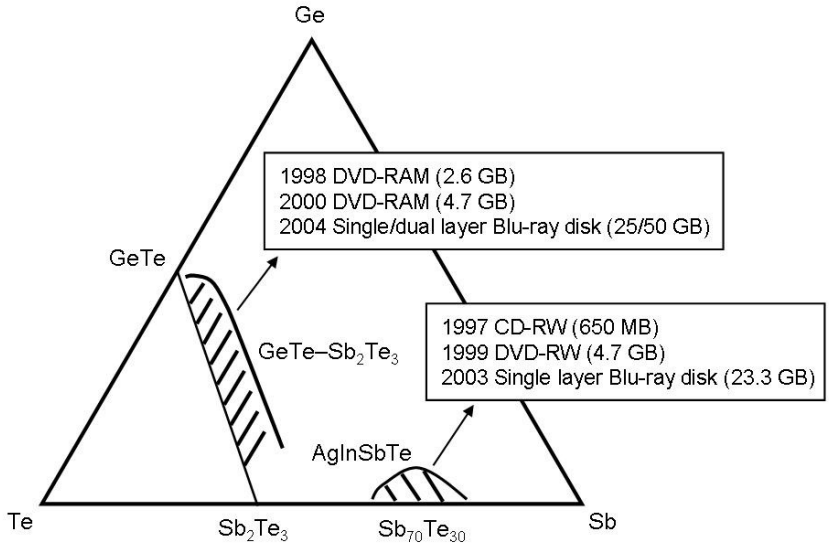

Figure 1.15. Different phase-change alloys of the GeSbTe family and their use in different optical storage products. After Wutting and Yamada [23].

Writability implies that the material should have a relatively low melting point of around 500 ºC. For the recorded information to be stable, the amorphous state needs to be stable, *i.e.* there should be high activation energy for crystallization W_A. At room temperature the amorphous regions should be stable for at least 10 years; this implies that the activation energy is higher than 1 eV/atom. On the contrary, too high an activation energy does not allow fast erasure at elevated temperature. The stored information should also be read easily

which implies that there should be a large signal-to-noise ratio. To improve the ratio, the contrast between the properties of the crystalline and the amorphous states should be as large as possible. The final requirement is cyclability. The degradation of a phase-change memory device occurs mainly due to the change of the compound concentration in the active medium alloy. The problem is especially important in electronic phase-change cells where the electromigration mechanism is present [23]. The change of the active medium composition influences, for instance, on the crystallization rate. Another problem is the formation of voids due to cyclical thermal stress. Such voids complicate the detection of the recorded information by optical means [24]. The goal is to achieve at least 10^7 cycles [18].

The desired properties are found for Ge-Sb-Te alloys along the line GeTe – Sb_2Te_3 and composites $Sb_{70}Te_{30}$ doped with Ag and In (see Figure 1.15). While achieving an amorphization time of order of 10 ns is not a problem, these materials are characterized by a relatively fast crystallization of a few tens of nanoseconds. Currently these alloys are used for phase-change memory applications, for instance as storage media in compact (CD), digital-versatile (DVD) and Blu-ray optical disks and non-volatile RAM memory in electronics. In the Blu-ray disk, with the wavelength of 405 nm, the minimum bit length is 150 nm and the data storage density is 0.015 Tbit/in^2 [25].

Metals: Gallium

Chalcogenide glass is used in today's phase-change memory devices. However, there are some prospective phase-change materials, which are being studied nowadays. One of such materials is metal gallium. Investigation of phase-change functionality in gallium was initially triggered by the possibility of achieving large optical nonlinearities via light-induced structural phase transitions in this metal [26]. Remarkable changes of optical properties created by structural phase transition in gallium enable the modulation of optical signals on a nanoscale, thus nanophotonics switches can be built [4, 5]. Since the current work is partially dedicated to the investigation of phase-change functionality in gallium (see Chapter 3), properties of this metal shall now be considered.

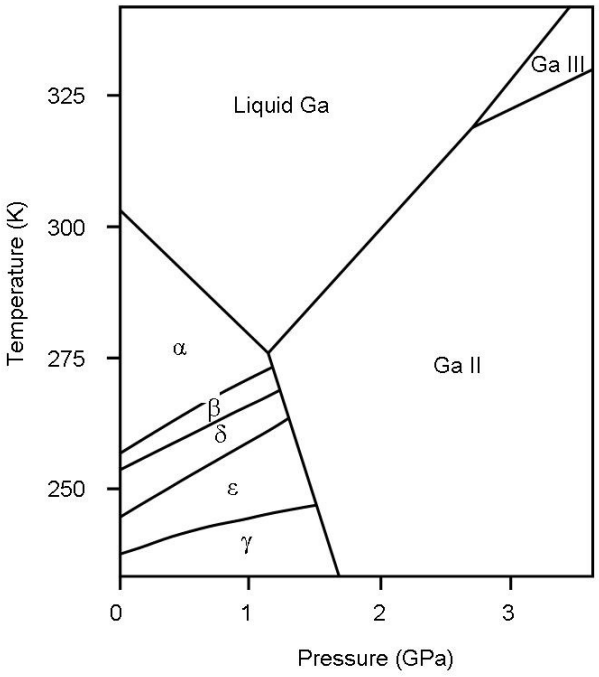

Figure 1.16. Gallium phase diagram. After Bosio [27].

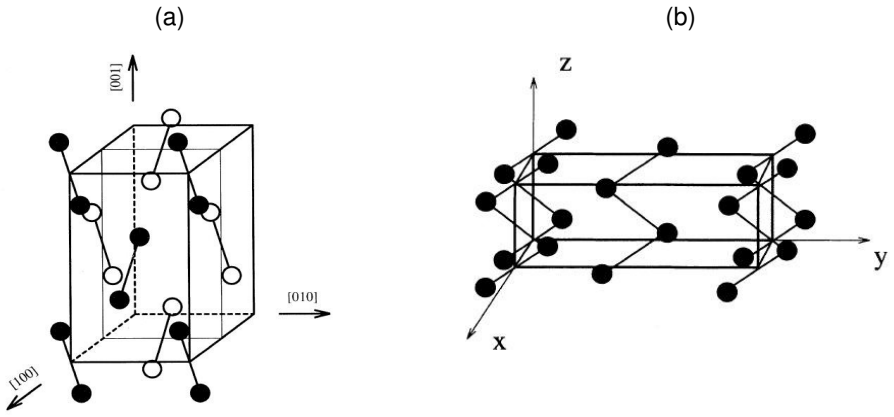

Figure 1.17. (a) Orthorhombic cell of α-Ga: each site is occupied by a Ga_2 dimer. (b) Monoclinic cell of β-Ga: the nearest-neighbor atoms form chains. After Bernasconi *et al.* [28].

Gallium was discovered spectroscopically by Lecoq de Boisbaudran in 1875 by its characteristic spectrum in compounds. Before its discovery, most of its properties had been predicted and described by Dmitri Ivanovich Mendeleev

on the basis of its position in the periodic table. Later Boisbaudran obtained the free metal by electrolysis of its hydroxide. Gallium is a soft metal with a silver colour. Gallium has atomic number 31, its atomic weight is 69.7 g/mol and the electronic configuration is $3d^{10}4s^{2}4p^{1}$. At atmospheric pressure, gallium melts at 29.8 ºC (302.9 K) and has a boiling point of 2204 ºC.

Table 1.1. Thermodynamic and crystallographic properties of different phases of gallium. After Defrain [30].

Phase name	Liquid or amorph.	α	β	δ	ε	γ
Melting Point, T_m (K) at P=0	–	302.9	256.9	253.8	244.6	237.6
Latent heat of fusion, L (J/g) at T_m at P=0	–	79.8	38.0	37.0	36.2	34.9
Heat capacity, C_p (J/Kmol)	28.0 at 300 K 30.0 at 200 K	26.6 at 303 K	28.0 at 256 K	–	–	26.8 at 237 K
Gibbs free energy difference to α-phase per atom, ΔG ($\times 10^{-2}$ eV)	–	0	2.23	2.26	–	2.44
Density, ρ (kg/m^3) at T_m at P=0	6095 at 303 K 6135 at 256.9 K 6153 at 237.6 K	5904	6220	6210	–	6200
Crystallographic system	–	Orthor.	Monocl.	Rhomb.	–	Orthor.
Atoms per cell	–	8	4	22	–	40

Gallium is known for its polymorphism and has a rather complicated phase diagram with many stable and metastable crystalline phases [27] (see Figure 1.16). At low pressure, gallium exists in the stable α-phase, which has an orthorhombic cell with each site occupied by Ga_2 dimer, thus α-solid Ga is a semi-metal [28]. On the contrary, gallium in liquid phase has a metallic behavior [29]. Two phases, GaII and GaIII, are only stable at high pressure. Also, at low pressure, there are a number of metastable phases called β-, δ-, ε- and γ-Ga. The probability of obtaining metastable phases in bulk gallium samples, even after

sufficient overcooling, is rather small and of order of 1/10, 1/100, 1/1000 and 1/10000 for β-, γ-, δ- and ε-phase, respectively [30]. This fact makes the investigation of the properties of gallium metastable phases rather complicated. However, in small gallium particles, the metastable phases (β, δ, ε, and γ) become stable, while the solid α-phase is not present [31]. Some known thermodynamic and crystallographic properties of different phases of gallium are summarized in Table 1.1. and the crystallographic cell structures of α- and β-Ga are shown in Figure 1.17.

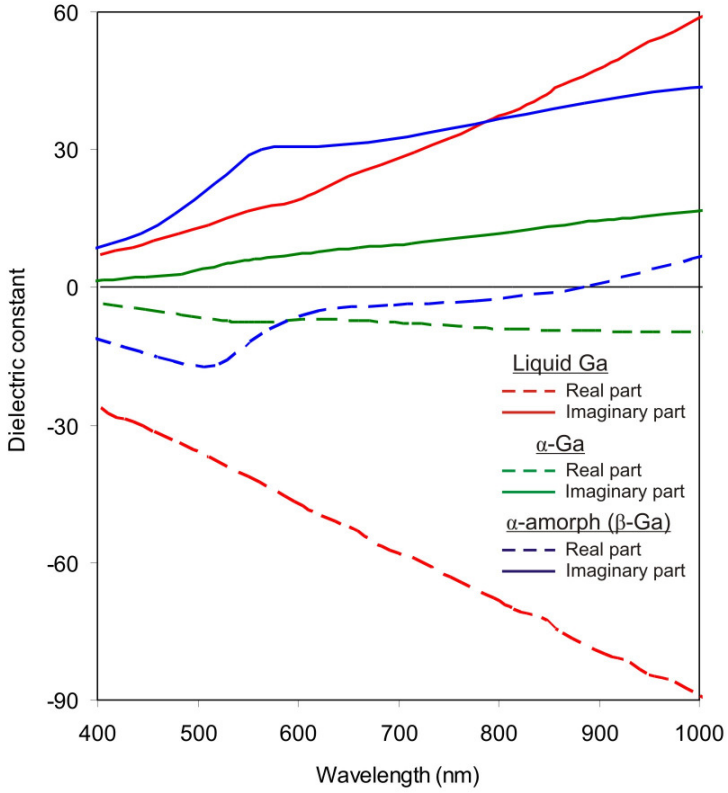

Figure 1.18. Dielectric constants of liquid gallium, α-Ga and fractionally disordered α- Ga (as a forced replacement for β-Ga).

Optical data for all gallium phases are not available in the literature. Dielectric constants for α-solid and liquid phases of gallium are known [32, 33]. Dielectric constants for β-Ga are not available apart from the optical conductivity given in [34]. The same source presents the dielectric constants for fractionally

disordered α-Ga; its optical conductivity is similar to that of β-Ga. Therefore dielectric constants for β-Ga are presumed to be similar to fractionally disordered α-Ga. Figure 1.18 summarizes all available dielectric constants for gallium in liquid, α-solid and fractionally disordered α-solid phases.

Strongly correlated electron insulators

Finally, one other class of phase-change materials, known as strongly correlated electron insulators [35–37], will be considered. Examples of such insulators are vanadium dioxide VO_2 and perovskite* manganites $R_{1-x}A_xMnO_3$ (where R is a rare earth element and A is an alkaline earth element, such as $Pr_{0.7}Ca_{0.3}MnO_3$). Both materials have similar electronic structures: each vanadium atom in the vanadium dioxide is bound to two oxygen atoms, leaving V^{4+} cations; each manganese atom in the perovskite is surrounded by an oxygen octahedron (6 atoms), leaving either Mn^{3+} or Mn^{4+} ions. Because of strong electron–electron and/or electron–lattice interactions, these materials possess rich phase diagrams and are extremely sensitive to external stimuli. For instance, photo-excitation of a low temperature phase of vanadium dioxide or perovskite manganites causes photocarrier generation, which results in ultrafast (femtosecond time scale) insulator-to-metal transformation. Thus, these materials can have a potential application in all-optical ultrafast switching. Moreover, phase transitions in perovskite manganites may be also induced by a magnetic field, x-rays, electron beams and current injection. Also perovskite manganites (as well as other perovskite materials) are known for such features as colossal magnetoresistance, ferroelectricity and spin dependent transport. So perovskites are candidates for magnetic memory devices and spintronics applications.

* Perovskites are a class of materials with a general chemical formula ABX_3, where A and B are cations and X is an anion that bonds to both.

1.5 Electron-specimen interaction

1.5.1 Optical and electron microscopy

Electron microscopy and electron-specimen interaction are described in many books [38, 39].

In far-field *optical microscopy* the absolute resolution due to the diffraction limit can be defined by Rayleigh's criterion:

$$r = \frac{0.61\lambda}{n\sin\alpha} \tag{1.29}$$

where λ is wavelength of the illuminant. The product $n\sin\alpha$ is called the *numerical aperture* (NA) of the objective lens, where α is the half-angle subtended by the objective lens at the object and n is the refractive index of the medium in the space between the object and objective lens. With high refractive liquids as a medium, the NA can be as high as 1.5. Therefore the resolution limit using blue light (λ = 400 nm), is about 150 nm. According to equation (1.29), a better resolution can be achieved by using an illumination source with a shorter wavelength. Such an illumination source is accelerated electrons.

The history of *electron microscopy* begins from the discovery of electrons by Sir Joseph John Thomson in 1896. The next crucial step towards electron microscopy was performed in 1924 by Louis de Broglie, who theoretically predicted that a moving electron has a dual identity. It can be regarded either as a moving charged particle or as radiation with an associated wavelength, which is:

$$\lambda = \frac{h}{p} = \frac{h}{m\upsilon} \tag{1.30}$$

where h is the Planck constant and $p = m\upsilon$ is the momentum of an electron with mass m moving with velocity υ. The velocity υ of an electron, accelerated by the voltage V, is

$$\beta = \frac{\upsilon}{c} = \sqrt{1 - \frac{1}{\left(1 + eV/m_e c^2\right)^2}} \tag{1.31}$$

where e and m_e are respectively the charge and rest mass of an electron. While the electron mass is defined as:

$$m = \frac{m_e}{\sqrt{1-(\upsilon/c)^2}} \tag{1.32}$$

Table 1.2 demonstrates the variation of electron velocity and wavelength with accelerating voltage (or kinetic electron energy).

Table 1.2. Variation of electron velocity and wavelength with accelerating voltage (or kinetic electron energy).

Accelerating voltage, kV or electron energy, keV	Electron velocity, in units of speed of light (β)	Electron wavelength, nm
1	0.062	0.0388
20	0.272	0.0086
50	0.413	0.0054
200	0.695	0.0025

In 1927 Hans Busch discovered that a magnetic coil can focus electrons just like an optical lens focuses light. This discovery opened a new field of electron optics and enabled electron microscopy.

The first electron microscope prototype was built in 1931 by Ernst Ruska and Max Knoll. Nowadays electron microscopy refers to a large family of instruments. In general, the electron microscope family can be divided into *transmission electron microscopes* (TEM) and *scanning electron microscopes* (SEM). All instruments have an *electron gun*, a system of lenses, and some sort of signal detector. An electron gun creates a stream of electrons from a *cathode* (a heated tungsten filament in the simplest case) and accelerates it to form an electron beam that has a precise kinetic energy.

The TEM involves a high voltage electron beam of 50–400 keV and a condenser lens to illuminate a specimen. After passing through the specimen the *transmitted electrons* are focused by the objective and projector lenses to a magnified image on a viewing screen. Due to the high electron kinetic energies (and the small wavelength) the resolution of TEM can be as high as sub-angstrom which makes the TEM a perfect tool for elemental and crystallographic microanalysis. Nevertheless the TEM has a requirement for a specimen to be transparent for electrons. This limits the specimen thickness to 100–500 nm.

In the SEM* the electrons are accelerated to energies in the range of 1–50 keV and the ways in which images are produced and magnified are entirely different in comparison to the TEM technique. In the SEM the electron beam is focused by the condenser and objective lenses at the surface of the specimen and scanned by the scan coils across it in a raster. Simultaneously, the detectors count generated electrons (or photons), given off from each point on the surface, to plot a raster image on a monitor screen. Depending on the SEM instrument, the resolution can be somewhere between 2 nm and 10 nm. The SEM is primarily used to study surface, or near surface, structure of specimens.

1.5.2 Electron-specimen interactions

Interaction of an incident electron with a specimen leads to a number of different effects, which makes electron microscopy a very powerful analytical system.

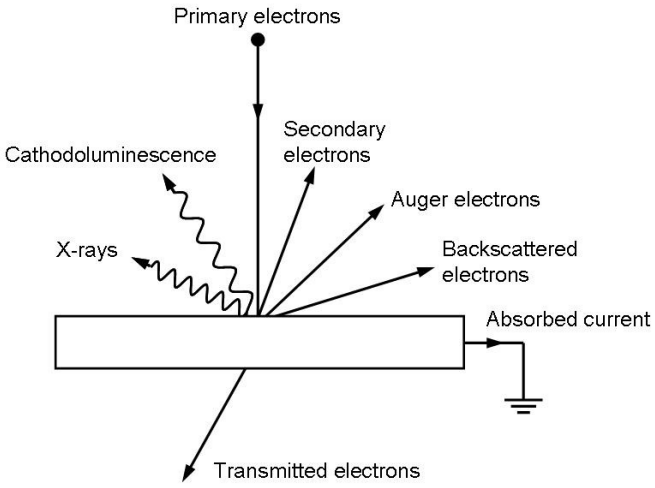

Figure 1.19. Schematic diagram of types of interactions resulting from electron bombardment of the specimen.

In general an incident (primary) electron scatters on specimen atoms *elastically*, when the electron is deflected (up to 180º) but no energy interchange occurs, or *inelastically*, when the electron interacts with the atom and supplies

* The SEM instrument used in the current work is described in Section 2.3.1

energy for a further process to occur, resulting in emission of an electron and/or electromagnetic radiation. A primary electron scatters inelastically when colliding with atomic electrons, whereas colliding with atomic nuclei causes nearly elastic scattering. Various effects resulting from electron-specimen interaction are detailed below (see Figure 1.19).

Backscattered or reflected electrons

Backscattered electrons are electrons from the primary electron beam which have been deflected by collisions with a specimen atomic nucleus and have turned back out of the specimen. Backscattering electron intensity increases with the increasing atomic number of specimen atoms. The mean energy of backscattered electrons is a fraction of the incident electron energy and its value also increases with increasing atomic number. The backscattered electrons can be collected with a backscattered electron detector to form images which show contrast between areas of a specimen with different chemical compositions.

Secondary electrons

An inelastic collision of primary electrons and the outer shell of electrons of the specimen atoms can result in outer electrons being detached from specimen atoms. These detached electrons are called *secondary electrons*. They have low kinetic energy, less then 50 eV, and can be captured by nearby ionized atoms. Nevertheless secondary electrons which are created near the specimen surface (about 10 nm of depth) can be emitted in a vacuum. The emitted secondary electrons can be collected with a secondary electron detector to form high-resolution surface images in the SEM which show the relief of the specimen surface.

Auger electrons

Auger electrons are ejected electrons resulting from inelastic collisions of primary electrons and the inner shell of electrons around an atomic nucleus in the specimen. Auger electrons have energies of up to 1-2 keV which are characteristic of specimen elements. Therefore, Auger electrons may be used for the elemental analysis of a specimen surface.

X-ray photons

There are a number of processes which cause *X-rays* to be emitted during electron-specimen interactions. The ejection of an Auger electron from an inner electron shell causes a vacancy to appear. This vacancy can be filled by an electron from one of the higher energy shells. Because of the difference between the energy states in the two shells, the process is accompanied by radiation of a *characteristic X-ray photon*.

Another process is *bremsstrahlung* (or braking) radiation. A primary electron that is deflected by an atomic nucleus may decelerate. This is accompanied by an emission of a photon with energy equal to the kinetic energy the electron has lost during deceleration. Since electron microscopy deals with electrons of 10–100 keV energy the maximum energy of bremsstrahlung photons will be in the X-ray part of the spectrum. Nevertheless, because of the individual deceleration history of each primary electron in the incident electron beam, the spectrum of bremsstrahlung radiation is continuous.

Radiated X-ray photons have enough energy to act as primary electrons, as described above, *i.e*. to eject electrons (photo-electrons) from the inner shells of specimen atoms which causes the emission of characteristic secondary X-rays or *fluorescent X-rays.*

Transmitted electrons

If the specimen is thin enough some incident electrons penetrate through it and emerge as *transmitted electrons*. Transmitted electrons can be separated into three groups:

Elastically scattered electrons have been deflected by interactions with the nucleus of specimen atoms. They have suffered zero, or very small, energy loss in the scattering process.

Inelastically scattered electrons have lost varying amounts of energy in collisions with the specimen. Their energy loss is characteristic of the atoms of the specimen therefore these electrons can be used for elemental analysis – *electron energy loss spectroscopy (EELS).*

Unscattered electrons have suffered no energy loss or deflection. They give no useful information on the specimen but can be easily separated.

Cathodoluminescence[*]

An incident electron can result in the promotion of specimen electrons from the valence band to the conduction band, thus creating electron-hole pairs. Recombination of an electron-hole pair may result in a photon being emitted. This phenomenon is called *cathodoluminescence* (CL) and it is typically observed in semiconductors and insulators. The phenomenon gave the name to the technique: *Scanning electron microscopy cathodoluminescence* (SEM-CL) [40].

CL is not the only phenomenon of light emission induced by electron bombardment (other phenomena are described in detail in Section 1.4); although any emitted light can be detected with the SEM-CL. In order to distinguish between the phenomenon "cathodoluminescence" and the technique with the same name, throughout this work the word "cathodoluminescence" is used to mean the technique, whereas the word "recombination emission" is for the phenomenon.

Absorbed current

Electrons (primary and secondary) which lost all their kinetic energy during collision, but did not escape the specimen, flow to the earth forming the *absorbed (specimen) current*. Therefore, if the specimen is not grounded, or it is an electrical insulator, these electrons will charge the specimen negatively. Electron microscopy is then no longer possible (unless other methods to remove the charge are used).

1.5.3 Semi-empirical model of electron scattering in solid targets

Elastic and inelastic scattering of the incident electron in the specimen can be modeled in the Monte Carlo simulation [39] or estimated analytically [42]. Simple equations which can be obtained from an analytical model would be helpful to understand the electron scattering process and give an estimate of such parameters

[*] The phenomenon cathodoluminescence was observed as early as the 1850-s by a number of researchers independently. However, the understanding of the effect came later. In fact, electrons (or cathode rays as they were originally known), that were detected by means of cathodoluminescence emission, were distinguished as unique particles by J. J. Thomson only in 1896 [39].

as electron beam maximum penetration depth or deposited energy in the specimen layer.

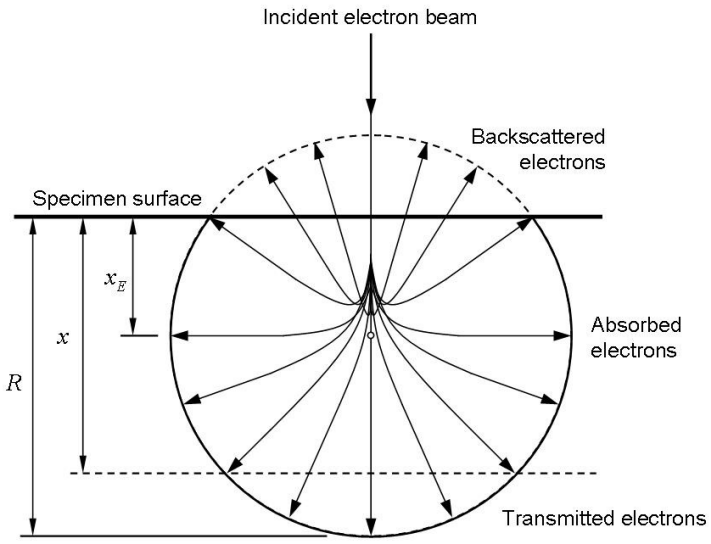

Figure 1.20. Model of electron beam scattering in the specimen: R is the maximum penetration depth; x_E the maximum energy dissipation depth; transmitted electrons at the depth x; absorbed electrons in the layer of the specimen between the surface and depth x. After Kanaya and Okayama [42].

A semi-empirical model of electron scattering in solids will be considered following the work of Kanaya and Okayama [42]. In the model, the incident electrons are supposed to travel straight into the specimen, suffering energy loss due to collisions with atomic electrons, and to be deflected due to collisions with atomic nuclei in the specimen (Figure 1.20). The cross-sections of the elastic nuclear and inelastic electronic collision are derived from an atomic model represented by the power potential $V(r) = Ze^2 a^{s-2} / sr^8$, where a and Z are, respectively, the atomic radius and atomic number of the specimen, and s = 6/5 is an empirical value.

The maximum penetration depth of the electron beam, derived from the cross-section for energy loss due to electronic collisions, is:

$$R = \frac{5.025 \cdot 10^{-12} A E_0^{5/3}}{\lambda_S Z^{8/9} \rho \cdot 1000} \tag{1.33}$$

where A and ρ are, respectively, the atomic weight [g/mol] and density [kg/m^3] of the specimen material, and E_0 is the energy of incident electrons [eV], while λ_S = 0.182 is an empirical parameter.

The energy loss due to electronic collisions also determines the energy E of the incident electrons at the depth x (expressed in terms of the reduced depth $y = x/R$):

$$E(y) = (1-y)^{3/5} E_0 \tag{1.34}$$

The fraction, η_T, of the incident electrons which is transmitted into the forward hemisphere on the depth y is

$$\eta_T = \exp\left(-\frac{\gamma y}{1-y}\right) \tag{1.35}$$

where the parameter $\gamma = 0.187 Z^{2/3}$ accounts for multiple electronic and nuclear collisions of the incident electrons. The fraction of backscattered electrons, η_B, is

$$\eta_B = \frac{6}{5}\int_0^y \frac{\gamma_B}{(1-y)^{7/6}} \exp\left(-\frac{\gamma_B y}{1-y}\right) dy - \frac{6}{5\times 2^{5/6}}\left\{1-\exp\left(-\frac{\gamma_B y}{1-y}\right)\right\} \tag{1.36}$$

where $\gamma_B = 1.9\gamma$. Therefore the fraction, η_A, of the electrons absorbed in a layer of the specimen between the surface and depth x is given by

$$\eta_A = 1 - (\eta_T + \eta_B) \tag{1.37}$$

The fraction of absorbed energy, E_A, from the incident electron energy, E_0, is defined as

$$\frac{E_A}{E_0} = 1 - \eta_T \frac{E(y)}{E_0} - \eta_B \frac{E_B}{E_0} \tag{1.38}$$

The fractional energy of backscattered electrons E_B/E_0 increases steadily with the increase of atomic number Z of the specimen. An interpolation curve E_B/E_0 against Z, based on experimental results from different sources, is shown in [42]. According to the curve, gallium (Z = 31) and gold (Z = 79), for example, have E_B/E_0 of 0.68 and 0.78, respectively.

According to the model the distribution of the electrons scattered in the specimen is represented by a sphere with the centre at the depth x_E called the maximum energy dissipation depth:

$$x_E = \frac{R\left(1+2\gamma-0.21\gamma^2\right)}{2\left(1+\gamma\right)^2} \tag{1.39}$$

1.6 Light emission induced by electron bombardment

1.6.1 Mechanisms of the induced light emission

Light emission induced by the passage of a fast electron through (or in the vicinity of) a specimen can occur via different mechanisms that include such phenomena as Cherenkov radiation, transition radiation, plasmon-mediated emission, recombination emission, and bremsstrahlung radiation [38, 39, 43, 44]. Here, all these phenomena will be described but paying more attention to the ones that are predominant in the case of SEM-CL analysis of metals and metallic nanostructures [44], since these are the samples studied in this work.

Cherenkov radiation

Cherenkov radiation (Figure 1.21) is emitted when an electron passes through a medium at a speed greater than the speed of light in that medium:

$$\upsilon > \frac{c}{n(\lambda)} \tag{1.40}$$

where υ is the speed of the electron, c is the speed of light and $n(\lambda)$ is the wavelength-dependent refractive index of the medium.

When an electron travels within the medium its moving electro-magnetic field induces a time-dependent polarization in the medium, which causes the emission of photons. However, when the electron travels at a speed less than the speed of light, these photons destructively interfere with each other and no radiation is detected. In contrast, when the electron travels faster than light, propagating through the medium, the photons constructively interfere resulting in

radiation. Cherenkov radiation can hardly be observed by means of SEM-CL since the velocity of electrons in an SEM is not high enough ($\upsilon/c < 0.4$).

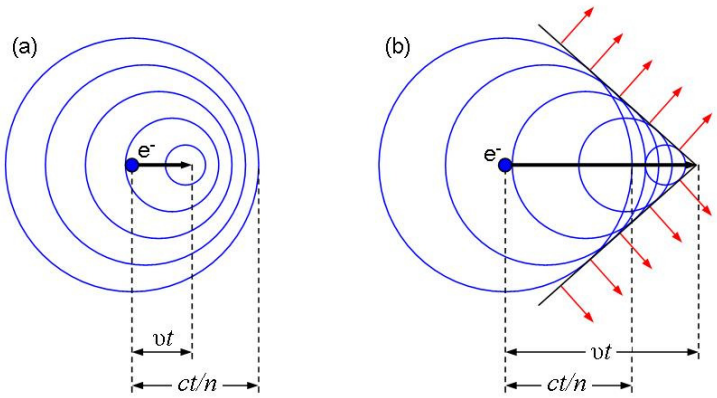

Figure 1.21. Cherenkov radiation. Spherical wavefronts of fields of an electron (e^-) travelling less (a) and greater (b) than the speed of light in the medium. Cherenkov radiation is emitted in the case (b).

Transition radiation

Transition radiation (Figure 1.22) is produced when an electron (travelling with any velocity) crosses the interface of two media of different dielectric constants.

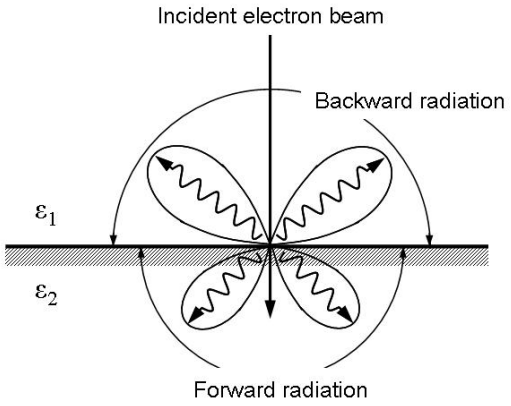

Figure 1.22. Generation of transition radiation from a single boundary and its angular distribution (butterfly shape in plane). Forward transition radiation is directed in a hemisphere along the electron velocity, backward transition radiation is directed in a hemisphere opposite to the electron velocity.

The case of an electron passing from a medium to a vacuum is most easy to understand. When an electron travels through the medium at a speed less than the speed of light, its moving electro-magnetic field induces a time dependent polarization in the medium, which causes the emission of photons. Nevertheless these photons destructively interfere with each other and no radiation occurs. When the electron travels through a vacuum, no polarization is induced. Therefore, photons induced in the medium near the medium/vacuum interface will not be compensated (since no photons are induced in a vacuum), but will give rise to transition radiation.

Plasmon-mediated emission

The field of an electron passing through (or in the vicinity of) the metal specimen perturbs conduction electrons. In the case of metallic nanoparticles, this perturbance causes oscillation of the conduction electrons, *i.e.* localized surface plasmons (discussed in Section 1.2 and Subsection 1.3.1). Localized surface plasmons may cause light emission (Figure 1.23).

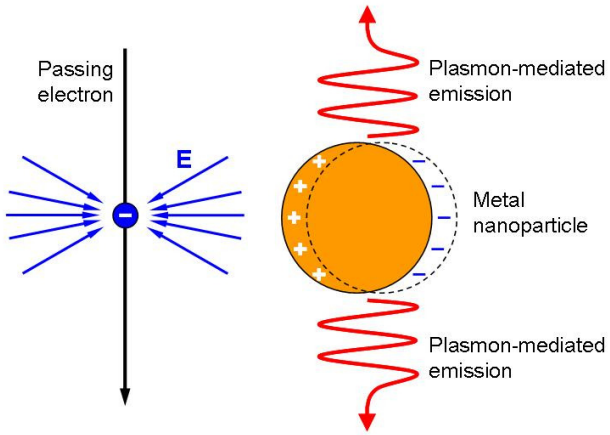

Figure 1.23. Schematic representation of plasmon-mediated emission. Electric field from the passing electron acts on the metal nanoparticle creating a localized surface plasmon. This plasmon may cause light emission.

Recombination emission

Recombination emission (Figure 1.24) induced by electron bombardment was described in Section 1.3.2.

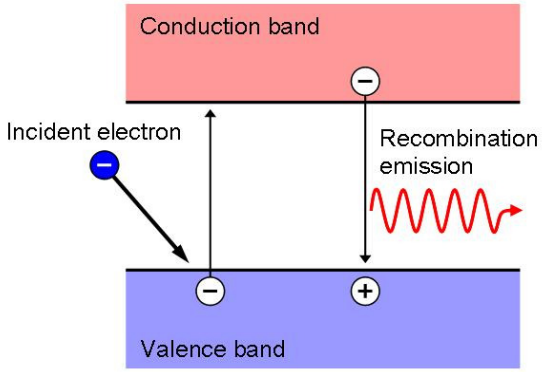

Figure 1.24. Recombination emission. An incident electron promotes a specimen electron from the valence to the conduction band, thus creating an electron-hole pair. Recombination of an electron-hole pair may result in a photon being emitted.

This type of light emission is predominant for semiconductors and insulators and is not possible in free-electron metals since the latter do not have a band structure. Nevertheless many metals in the visible and near IR region do not behave like free electron ones, which enables interband transitions and therefore recombination emission. For instance, optically excited recombination emission (photoluminescence) in noble metals is well known [45].

Bremsstrahlung radiation

Bremsstrahlung radiation (Figure 1.25) was described in Section 1.3.2. The spectrum of bremsstrahlung radiation is continuous, with a maximum in the X-ray region, although some contribution may be observed in the visible range. However, in the case of metals, bremsstrahlung radiation plays the minor role in total the light emission in visible and IR spectral range and is much fainter than the transition radiation [46].

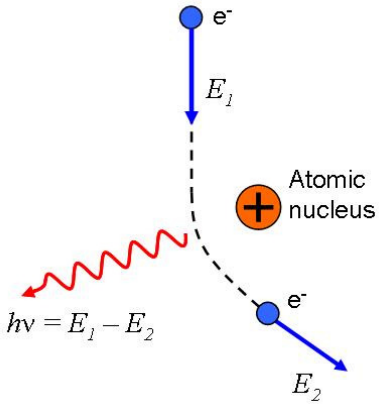

Figure 1.25. Bremsstrahlung radiation. An incident electron (e^-) deflected by an atomic nucleus may decelerate. This is accompanied by an emission of a photon with energy equal to the kinetic energy the electron has lost during deceleration.

1.6.2 Transition radiation from plane interfaces

Transition radiation was theoretically predicted by I. Frank and V. Ginsburg in 1945 by considering the case of an electron crossing the boundary between two media [46]. Later V. Pafomov and I. Frank obtained the solution for the problem of the radiation from a charged particle, which passes through three media separated by plane boundaries [47]. Here the latter case will be considered since it is a more general one.

The electron (charge e) moves with a speed υ (or $\beta = \upsilon/c$) perpendicular to the bounding surfaces (in a positive z direction) from medium 1 through a layer of thickness d of medium 2, and then into medium 3. The media 1, 2, and 3 are described by complex refractive indices $\tilde{n}_1$, $\tilde{n}_2$, and $\tilde{n}_3$ respectively. The radiation is considered in medium 3 in the wave zone at a point A at the angle θ_3. The point A is at a sufficiently large distance R from the points where the electron passes through boundaries, so that the entire radiation field at A forms a spherical wave. The field of a moving charge can be represented as a field of a system of fixed dipoles. So the field at the point A is found by integrating the field produced by all of the dipoles located in media 3, 2, and 1.

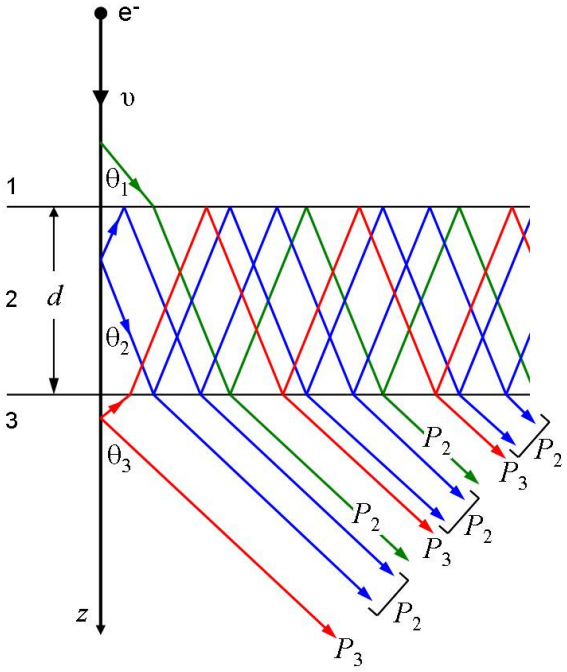

Figure 1.26. Light emission by an electron passing through a plate material, consisting of radiation from three regions, indicated schematically as P_1, P_2 and P_3. After Pafomov and Frank [47].

The result for the radiated energy in a unit solid angle $d\Omega$ and unit frequency range $d\omega$ is:

$$\frac{d^2E}{d\omega d\Omega} = \frac{e^2\upsilon^2}{4\pi^2 c^3}\left|P_1 + P_2 + P_3\right|^2 n_3 \sin^2\theta_3 e^{-\alpha_3 R} \tag{1.41}$$

Here n_3 is the real part of the refractive index and α_3 is the absorption coefficient of the waves in medium 3 (if medium 3 is vacuum then $e^{-\alpha_3 R} = 1$). The quantities P_1, P_2, and P_3, which make up the amplitude, are determined by the fields generated by the electron in its paths in the respective media 1, 2, and 3 (Figure 1.26). They are given by the formulas:

$$P_1 = \frac{n_3}{n_1} f_{32} f_{21} \alpha(r,d) \frac{1}{1-\beta\tilde{n}_1\cos\theta_1} \exp\left(-i\frac{\omega}{\upsilon}d + i\frac{\omega}{c}\tilde{n}_2 \cdot d\cos\theta_2\right) \tag{1.42}$$

$$P_2 = \frac{\tilde{n}_3}{\tilde{n}_2} f_{32}\alpha(r,d)\left\{\frac{1}{1-\beta\tilde{n}_2\cos\theta_2}\left[1-\exp\left(-i\frac{\omega}{\upsilon}d + i\frac{\omega}{c}\tilde{n}_2 \cdot d\cos\theta_2\right)\right]+\right.$$

$$+\frac{r_{21}}{1+\beta\tilde{n}_2\cos\theta_2}\left[\exp\left(i\frac{\omega}{c}\tilde{n}_2 2d\cos\theta_2\right)-\exp\left(-i\frac{\omega}{\upsilon}d+i\frac{\omega}{c}\tilde{n}_2\cdot d\cos\theta_2\right)\right]\Bigg\} \qquad (1.43)$$

$$P_3=-\frac{1}{1-\beta\tilde{n}_3\cos\theta_3}-\frac{\alpha(r,d)}{1+\beta\tilde{n}_3\cos\theta_3}\left[r_{32}+r_{21}\exp\left(i\frac{\omega}{c}\tilde{n}_2\cdot 2d\cos\theta_2\right)\right] \qquad (1.44)$$

where f_{ik} and r_{ik} are the Fresnel coefficients for refraction and reflection respectively:

$$f_{ik}=\frac{2\tilde{n}_i\cos\theta_i}{\tilde{n}_k\cos\theta_i-\tilde{n}_i\cos\theta_k} \qquad r_{ik}=\frac{\tilde{n}_k\cos\theta_i+\tilde{n}_i\cos\theta_k}{\tilde{n}_k\cos\theta_i-\tilde{n}_i\cos\theta_k} \qquad (1.45)$$

The coefficient $\alpha(r,d)$ takes account of multiple reflection in medium 2:

$$\alpha(r,d)=\left[1-r_{21}r_{23}\exp\left(i\frac{\omega}{c}\tilde{n}_2 2d\cos\theta_2\right)\right]^{-1} \qquad (1.46)$$

The angle θ_i (i = 1, 2) is defined by Snell's law $\theta_i=\arcsin\left(n_3\sin\theta_3/n_i\right)$.

Expression (1.41) is written in the CGS unit system (the other equations are invariant in any unit system). Throughout this work radiation is defined in Joules per nanometer (J/nm), therefore, Expression (1.41) will take the form:

$$\frac{d^2E}{d\lambda d\Omega}=\frac{\alpha\cdot\beta^2}{\pi^2\lambda^2}\cdot\frac{hc}{10^{-9}}\cdot\left|P_1+P_2+P_3\right|^2 n_3\sin^2\theta_3 e^{-\alpha_3 R} \qquad (1.47)$$

where $\alpha = 1/137$ is the Sommerfeld fine-structure constant, h is Planck's constant and λ is wavelength in (nm).

The equations above give the solution for *forward transition radiation* (radiation is directed in a hemisphere along the electron velocity). The solution for *backward transition radiation* (radiation is directed in a hemisphere opposite to the electron velocity) is obtained by the replacement of the electron velocity, υ, by the velocity, $-\upsilon$, in Expressions (1.42–1.44). Total energy radiated in unit wavelengths in a forward (backward) hemisphere is obtained by integration (1.47) over the solid angle of 2π:

$$\frac{dE}{d\lambda}=\int\frac{d^2E}{d\lambda d\Omega}d\Omega=2\pi\int_0^{\pi}\frac{d^2E}{d\lambda d\Omega}\sin\theta_3 d\theta_3 \qquad (1.48)$$

By taking $\tilde{n}_2=\tilde{n}_3$ ($\tilde{n}_1=\tilde{n}_2$) the solution of the radiation from an electron crossing the boundary between two media (single interface) is obtained.

1.6.3 Solution of Maxwell's equations for electron-beam-induced light emission

Electron-induced light emission can be found by solving Maxwell's equations, which was performed by F. J. García de Abajo and A. Howie [48, 49]. The underlying procedure is presented in this subsection; all equations here are given in Gaussian atomic units.

A passing electron creates the electromagnetic field (external field) $\mathbf{E}^{ext}$, $\mathbf{H}^{ext}$ which scatters on the object and gives rise to the scattered or induced electromagnetic field $\mathbf{E}^{ind}$, $\mathbf{H}^{ind}$ (see Figure 1.27).

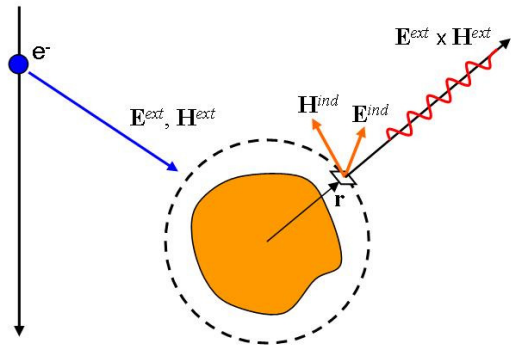

Figure 1.27. Schematic representation of the geometry under study: a passing electron creates an external electromagnetic field which scatters on the object giving rise to the scattered or induced electromagnetic field. The induced field may give rise to radiating emission.

In this case the radiated energy can be calculated by integrating the Poynting vector normal to an arbitrary large sphere centered around the object, that is

$$\Delta E^{rad} = \frac{c}{4\pi}\int dt \int d\Omega_{\mathbf{r}} \cdot r^2 \left[\mathbf{E}^{ind}(\mathbf{r},t)\times\mathbf{H}^{ind}(\mathbf{r},t)\right]\cdot\mathbf{r} \qquad (1.49)$$

where $\mathbf{r}$ points to the surface of the sphere and the integral over the time is included. Expressing the fields in terms of their frequency components gives

$$\Delta E^{rad} = \int_0^\infty \omega d\omega \int d\Omega_{\mathbf{r}} \cdot \Gamma^{rad}(\omega,\Omega_{\mathbf{r}})$$

where

$$\Gamma^{rad}(\omega,\Omega_{\mathbf{r}}) = \frac{cr^2}{4\pi^2\omega}\mathrm{Re}\left\{\left[\mathbf{E}^{ind}(\mathbf{r},t)\times\mathbf{H}^{ind}(\mathbf{r},t)\right]\cdot\mathbf{r}\right\} \tag{1.50}$$

is the probability of emitting a photon of energy ω per unit energy range and unit solid angle around the direction $\Omega_{\mathbf{r}}$.

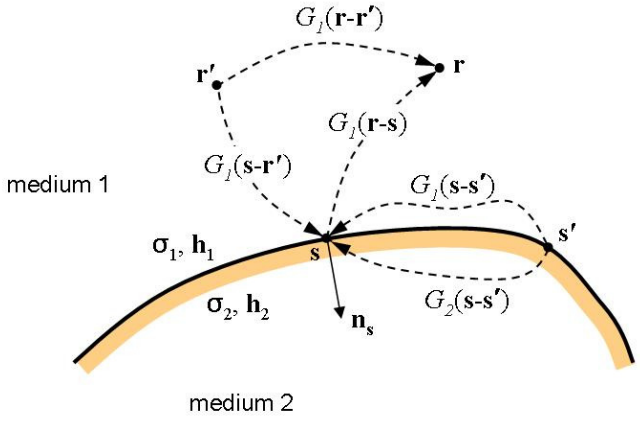

Figure 1.28. Schematic representation of the elements involved in the solution of Maxwell's equations by means of the boundary element method (BEM). The interface shown in the figure (solid curve) separates medium 1 from medium 2. The interface normal $\mathbf{n}_\mathbf{s}$ at a given interface point $\mathbf{s}$ is chosen to be directed towards medium 2. The interaction between different points within a given medium j is described by means of the Green function G_j. The induced electromagnetic field at $\mathbf{r}$ (within j = 1 in the figure) is expressed in terms of the external source (located at $\mathbf{r}'$ in the figure) plus some equivalent boundary charges and currents, $\sigma_j(\mathbf{s})$ and $\mathbf{h}_j(\mathbf{s})$, respectively, which accounts for the action of any external and induced sources beyond the boundary surface. After García de Abajo and Howie [49].

The induced electric and magnetic fields, $\mathbf{E}^{ind}$ and $\mathbf{H}^{ind}$, can be found by the *boundary element method* (BEM) [49]. Maxwell's equation in frequency space are:

$$\nabla\cdot\mathbf{D} = 4\pi\rho\,, \qquad \nabla\times\mathbf{H} + ik\mathbf{D} = \frac{4\pi}{c}\mathbf{j}\,, \tag{1.51}$$

$$\nabla\cdot\mathbf{B} = 0\,, \qquad \nabla\times\mathbf{E} - ik\mathbf{B} = 0 \tag{1.52}$$

where $k = \omega / c$, $\mathbf{D} = \varepsilon \mathbf{E}$ is the electric displacement, $\mathbf{B} = \mu \mathbf{H}$ is the magnetic induction, ρ and $\mathbf{j}$ are density of charge and density of current, respectively. The dielectric function $\varepsilon(\mathbf{r}, \omega)$ and the magnetic permeability $\mu(\mathbf{r}, \omega)$ might depend upon space $\mathbf{r}$ and frequency ω. Equations (1.52) enable the expression of the electric and magnetic fields $\mathbf{E}$ and $\mathbf{H}$ in terms of scalar and vector potentials φ and $\mathbf{A}$ as

$$\mathbf{E} = ik\mathbf{A} - \nabla\varphi \tag{1.53}$$

and

$$\mathbf{H} = \frac{1}{\mu} \nabla \times \mathbf{A} \tag{1.54}$$

The Lorentz gauge condition $\nabla \cdot \mathbf{A} = ik\varepsilon\mu\varphi$ will be adopted here.

Then, Equations (1.51) can be recast as

$$\left(\nabla^2 + k^2 \varepsilon\mu\right)\varphi = -4\pi\left(\frac{\rho}{\varepsilon} + \sigma_S\right) \tag{1.55}$$

and

$$\left(\nabla^2 + k^2 \varepsilon\mu\right)\mathbf{A} = -\frac{4\pi}{c}\left(\mu\mathbf{j} + \mathbf{m}\right) \tag{1.56}$$

where $\sigma_S = \frac{1}{4\pi}\mathbf{D} \cdot \nabla\frac{1}{\varepsilon}$ and $\mathbf{m} = -\frac{1}{4\pi}\left[i\omega\varphi\nabla(\varepsilon\mu) + c\mathbf{H} \times \nabla\mu\right]$.

The above expressions remain valid for any arbitrary spatially-dependent dielectric function, ε, and magnetic permeability, μ. Here, the case of abrupt interfaces that separate two homogeneous media, labeled as 1 and 2 is considered. The media 1 and 2 are characterized by frequency-dependent response functions (ε_1, μ_1) and (ε_2, μ_2), respectively. A schematic representation of the different elements involved in the theory is shown in Figure 1.28.

The solution of Equations (1.55) and (1.56) for $\mathbf{r}$ (induced electromagnetic field at $\mathbf{r}$) inside each medium *j* is

$$\varphi(\mathbf{r}) = \frac{1}{\varepsilon_j(\omega)} \int d\mathbf{r}' G_j\left(|\mathbf{r} - \mathbf{r}'|\right)\rho(\mathbf{r}') + \int_{S_j} d\mathbf{s} G_j\left(|\mathbf{r} - \mathbf{s}|\right)\sigma_j(\mathbf{s}) \tag{1.57}$$

and

$$\mathbf{A}(\mathbf{r}) = \frac{\mu_j(\omega)}{c}\int d\mathbf{r}' G_j(|\mathbf{r}-\mathbf{r}'|)\mathbf{j}(\mathbf{r}') + \int_{S_j} d\mathbf{s} G_j(|\mathbf{r}-\mathbf{s}|)\mathbf{h}_j(\mathbf{s}) \tag{1.58}$$

where S_j refers to the boundary of the medium j = 1,2; and $G_j(r) = e^{ikjr}/r$ is the Green function which describes interaction between different points within a medium j. The external source located at $\mathbf{r}'$ (created by a passing electron in the present case) is introduced in terms of density of charge and density of current, $\rho(\mathbf{r}')$ and $\mathbf{j}(\mathbf{r}')$, respectively. Therefore, the induced electromagnetic field at $\mathbf{r}$ is expressed in terms of the external source plus some equivalent boundary charges and currents, $\sigma_j(\mathbf{s})$ and $\mathbf{h}_j(\mathbf{s})$, respectively, which account for the action of any external and induced sources. The boundary charges and currents can be determined upon the solution of a set of four Equations (1.59–1.62) implied by the boundary conditions.

The continuity of the tangential electric field and the normal magnetic induction at the interface is guaranteed by the continuity of the potentials, φ and $\mathbf{A}$, which leads to:

$$G_1\sigma_1 - G_2\sigma_2 = \varphi_2^e - \varphi_1^e \tag{1.59}$$

$$G_1\mathbf{h}_1 - G_2\mathbf{h}_2 = \mathbf{A}_2^e - \mathbf{A}_1^e \tag{1.60}$$

where $\varphi_j^e(\mathbf{r}) = \frac{1}{\varepsilon_j(\omega)}\int d\mathbf{r}' G_j(|\mathbf{s}-\mathbf{r}'|)\rho(\mathbf{r}')$ and $\mathbf{A}_j^e(\mathbf{s}) = \frac{\mu_j(\omega)}{c}\int d\mathbf{r}' G_j(|\mathbf{s}-\mathbf{r}'|)\mathbf{j}(\mathbf{r}')$ are equivalent boundary sources, which would be created at the interface points by the external source located at $\mathbf{r}'$.

The continuity of the tangential magnetic field potential and the vector potential (in the nonmagnetic case) implies:

$$\begin{aligned} &H_1\mathbf{h}_1 - H_2\mathbf{h}_2 - ik\mathbf{n}_s(G_1\varepsilon_1\mu_1\sigma_1 - G_2\varepsilon_2\mu_2\sigma_2) = \\ &= (\mathbf{n}_s\cdot\nabla_{\mathbf{s}})(\mathbf{A}_2^e - \mathbf{A}_1^e) + ik\mathbf{n}_s(\varepsilon_1\mu_1\varphi_1^e - \varepsilon_2\mu_2\varphi_2^e) \end{aligned} \tag{1.61}$$

where H_j is the normal derivative of the Green function G_j.

Finally, the continuity of the normal electric displacement leads to:

$$\begin{aligned} &H_1\varepsilon_1\sigma_1 - H_2\varepsilon_2\sigma_2 - ik\mathbf{n}_s(G_1\varepsilon_1\mathbf{h}_1 - G_2\varepsilon_2\mathbf{h}_2) = \\ &= \mathbf{n}_s\cdot\left[\varepsilon_1(ik\mathbf{A}_1^e - \nabla_{\mathbf{s}}\varphi_1^e) - \varepsilon_2(ik\mathbf{A}_2^e - \nabla_{\mathbf{s}}\varphi_2^e)\right] \end{aligned} \tag{1.62}$$

Upon the discretization of the interface (surface of the object) using parameterization points Equations (1.59–1.62) can be solved numerically and the boundary charges and currents, $\sigma_j(\mathbf{s})$ and $\mathbf{h}_j(\mathbf{s})$ can be found at each point on the interface. The scalar and vector potentials, $\varphi(\mathbf{r})$ and $\mathbf{A}(\mathbf{r})$, can then be found for any arbitrary point $\mathbf{r}$ using Equations (1.57) and (1.58). The induced electric and magnetic fields, $\mathbf{E}^{ind}(\mathbf{r})$ and $\mathbf{H}^{ind}(\mathbf{r})$, can be obtained for each point $\mathbf{r}$ by Expressions (1.53) and (1.54). The photon emission probability (electron-induced photon emission in the present case), $\Gamma^{rad}(\omega, \Omega_{\mathbf{r}})$, is then found by Expression (1.50).

The numerical technique described above is complicated for 3D objects, while the solution for axially-symmetric objects is much simpler. The latter was implemented by F. J. García de Abajo *et al.* in the form of the BEMAX (boundary element method for axial-symmetry electromagnetism) program. The program allows for the calculation of electron-induced photon emission from non-magnetic, axially-symmetric objects of arbitrary shape using frequency-dependent complex dielectric functions of the object's media. The program gives the solution of photon emission probability in photons per eV of photon energy range per incoming electron. The light emission, in J/nm, can be found by multiplying the photon emission probability in photon/eV on the term $\left(\frac{ch}{10^{-9}}\right)^2 \cdot \frac{1}{e \cdot \lambda^3}$, where λ is wavelength in nm.

The boundary element method described above accounts for the following types of electron-induced photon emission: Cherenkov radiation, transition radiation and plasmon-mediated emission.

The described method can be used to define interactions of objects with light as well. In this case the external electromagnetic field is the one produced by the incident light wave, while the procedure for determination of the induced electromagnetic field is essentially the same.

1.7 Thesis plan

Following this introductory chapter, this thesis consists of three chapters, each describing an original piece of work, and a concluding chapter:

Chapter 2 describes an integrated experimental setup developed for nanostructured sample preparation and characterization. The setup was used for the investigation of gallium nanoparticle preparation based on the light-assisted deposition technique.

Chapter 3 reports on the CL detection of gallium nanoparticle phase state, which offers a route for the readout of high-density phase-change memories. Also selectively electron beam addressed, erasable memory functionality is demonstrated in gallium nanoparticle films.

Chapter 4 reports on the demonstration of functionality of a transmitting optical antenna based on a pair of closely-spaced gold nanorods. The antenna effectively couples the energy of a nanoscale source of excitation, created by the focused electron beam, to far-field radiation detected by means of CL.

Chapter 5 concludes the thesis with a summary of the results reported in previous chapters and provides a discussion of potential research work.

The work reported in this thesis was carried out while the author was registered as a postgraduate student within the School of Physics and Astronomy and the Optoelectronics Research Centre at the University of Southampton, UK. It is, unless otherwise indicated, the original work of the author.

1.8 References

[1] E. Betzig, J. K. Trautman, T. D. Harris, J. S. Weiner, and R. L. Kostelak, *"Breaking the diffraction barrier: Optical microscopy of a nanometric scale,"* Science **251,** 1468 (1991).

[2] N. Yamamoto, K. Araya, F. J. García de Abajo, *"Photon emission from silver particles induced by a high-energy electron beam,"* Phys. Rev. B **64**, 205419 (2001).

[3] S. A. Maier, *"Plasmonics: fundamentals and applications,"* New-York: Springer, 2007.

[4] N. I. Zheludev, *"Nonlinear optics on the nanoscale,"* Contemp. Physics **43**, 365 (2002).

[5] N. I. Zheludev, *"Single nanoparticle as photonic switch and optical memory element,"* J. Opt. A **8**, S1 (2006).

[6] M. L. Brongersma, *"Engineering optical nanoantennas,"* Nat. Photonics **2**, 270 (2008).

[7] C. F. Bohren and D. R. Huffman, *"Absorption and scattering of light by small particles,"* Weinheim: Wiley-VCH, 2004.

[8] H.C. van de Hulst, *"Light scattering by small particles,"* New York: Dover Publications, Inc., 1987.

[9] G. Schider, J. R. Krenn, A. Hohenau, H. Ditlbacher, A. Leitner, F. R. Aussenegg, W. L. Schaich, I. Puscasu, B. Monacelli, and G. Boreman, *"Plasmon dispersion relation of Au and Ag nanowires,"* Phys. Rev B **68**, 155427 (2003).

[10] J. Aiapurua, G. W. Bryant, L. J. Richter, F. J. García de Abajo, B. K. Kelly, and T. Mallouk, *"Optical properties of coupled metallic nanorods for field-enhanced spectroscopy,"* Phys. Rev. B **71**, 235420 (2005).

[11] C. Dahmen and G. von Plessen, "Optical effects of metallic nanoparticles," Aust. J. Chem. **60**, 447 (2007).

[12] V. Myroshnychenko, J. Rodríguez-Fernández, I. Pastoriza-Santos, A. M. Funston, C. Novo, P. Mulvaney, L. M. Liz-Marzán, and F. J. García de Abajo, *"Modelling the optical response of gold nanoparticles,"* Chem. Soc. Rev. **37**, 1792 (2008).

[13] T. Yamaguchi, S. Yoshida, and A. Kinbara, *"Anomalous optical absorption of aggregated silver films,"* Thin Solid Film **21**, 173 (1974).

[14] T. Yamaguchi, S. Yoshida, and A. Kinbara, *"Optical effect of the substrate on the anomalous absorption of aggregated silver films,"* Thin Solid Film **21**, 173 (1974).

[15] V. A. Fedotov, V. I. Emel'yanov, K. F. MacDonald, and N. I. Zheludev, *"Optical properties of closely packed nanoparticle films: spheroids and nanoshells,"* J. Opt. A **6**, 155 (2004).

[16] R. S. Berry and B. M. Smirnov, *"Phase stability of solid clusters,"* J. Chem. Phys. **113**, 728 (2000).

[17] S. R. Ovshinsky, *"Reversible electrical switching phenomena in disordered structures,"* Phys. Rev.Lett. **21**, 1450 (1968).

[18] R. Waser, *"Nanoelectronics and information technology,"* 2nd edition, Weinheim: Wiley-VCH, 2005.

[19] M. Wautelet, *"Estimation of the variation of the melting temperature with the size of small particles, on the basis of a surface-phonon instability model,"* J. Phys. D **24**, 343 (1991).

[20] A. S. Shirinyan and W. Wautelet, *"Phase separation in nanoparticles,"* Nanotechnology **15**, 1720 (2004).

[21] E. V. Charnaya, C. Tien, K. J. Lin, and Yu. A. Kumzerov, *"X-ray and resistance studies of the melting and freezing phase transitions for gallium in an opal,"* J. Phys. **10**, 7273 (1998).

[22] B. F. Soares, M. V. Bashevoy, F. Jonsson, K. F. MacDonald, and N. I. Zheludev, *"Polymorphic nanoparticles as all-optical memory elements,"* Opt. Express **14,** 10652 (2006).

[23] L. Goux, D. T. Castro, G. A. M. Hurkx, J. G. Lisoni, R. Delhougne, D. J. Gravesteijn, K. Attenborough, and D. J. Wouters, *"Degradation of the reset switching during endurance testing of a phase-change line cell,"* IEEE Trans. Elect. Devices **56,** 354 (2009).

[24] A. E. T. Kuiper, D. Pasquariello, C. W. T. Bulle-Lieuwma, M. Kaiser, M. A. Verheijen, H. A. G. Nulens, L. van Pieterson, and G. J. Y. Zhong,

"Analysis of the Degradation Mechanism during Repeated Overwrite of Phase-Change Discs," Jpn. J. Appl. Phys. **46,** 1037 (2007).

[25] M. Wutting and N. Yamada, *"Phase-change materials for rewriteable data storage,"* Nat. Mater. **6**, 824 (2007).

[26] P. J. Bennett, S. Dhanyal, P. Petropoulos, D. J. Richardson, N. I. Zheludev, and V. I. Emelyanov, *"A photonic switch based on a gigantic, reversible optical nonlinearity of liquefying gallium,"* Appl. Phys. Lett. **73**, 1787 (1998).

[27] L. Bosio *"Crystal structure of Ga(II) and Ga(III),"* J. Chem. Phys. **68**, 1221 (1978).

[28] M. Bernasconi, G. L. Chiarotti, and E. Tosatti, *"Ab initio calculations of structural and electronic properties of gallium solid-state phases,"* Phys. Rev. B **52**, 9988 (1995).

[29] N. R. Comins, *"The optical properties of liquid metals,"* Phil. Mag. **25**, 817 (1972).

[30] A. Defrain, *"Etats metastables du gallium, surfusion et polymorphisme,"* J. Chim. Phys. **74**, 851 (1977).

[31] A. Di Cicco, *"Phase transitions in confined gallium droplets,"* Phys. Rev. Lett. **81**, 2942 (1998).

[32] R. Kofman, P. Cheyssac, and J. Richard, *"Optical properties of Ga monocrystal in the 0.3–5-eV range,"* Phys. Rev. B **16,** 5216 (1977).

[33] R. S. Teshev and A. A. Shebzukhov, *"Electronic characteristics and dispersion of optical constants of liquid gallium in the 0.4–2.5-μm spectral region,"* Opt. Spectrosc. **65**, 693 (1988).

[34] O. Hunderi and R. Ryberg, *"Amorphous gallium – a free electron metal,"* J. Phys. F **4**, 2096 (1974).

[35] A. Cavalleri, M. Rini, and R. W. Schoenlein, *"Ultra-broadband femtosecond measurements of the photo-induced phase transition in VO_2: From the mid-IR to the hard X-rays,"* J. Phys. Soc. Jpn. **75**, 011004 (2006).

[36] Y. Tokura, *"Critical features of colossal magnetoresistive manganites,"* Rep. Prog. Phys. **69**, 797 (2006).

[37] D. Polli, M. Rini, S. Wall, R. W. Schoenlein, Y. Tomioka, Y. Tokura, G. Cerullo, and A. Cavalleri, *"Coherent orbital waves in the photo-induced insulator–metal dynamics of a magnetoresistive manganite,"* Nat. Mater. **6**, 643 (2007).

[38] I. M. Watt, *"The principles and practice of electron microscopy,"* 2nd edition, Cambridge: Cambridge University Press, 1997.

[39] P. J. Goodhew, J. Humphreys, and R. Beanland, *"Electron microscopy and analysis,"* 3rd edition, London and New York: Taylor & Francis, 2001.

[40] D. R. Vij, *"Luminescence of solids,"* New York: Plenum Press, 1998.

[41] E. N. Harvey, *"A history of luminescence: From the earliest times until 1900,"* Philadelphia: American Philosophical Society, 1957.

[42] K. Kanaya and S. Okayama, *"Penetration and energy-loss theory of electrons in solid targets,"* J. Phys. D. **5**, 43 (1972).

[43] J. D. Jackson, *"Classical electrodynamics,"* 3rd edition, Wiley, 1962.

[44] N. Yamamoto, K. Araya, A. Toda, and H. Sugiyama, *"Light emission from surfaces, thin films and particles induced by high-energy electron beam,"* Surf. Interface Anal. **31**, 79 (2001).

[45] P. Apell, R. Monreal, and S. Lundqvist, *"Photoluminescence of noble metals,"* Phys. Scr. **38**, 174 (1988).

[46] I. Frank and V. Ginsburg, *"Radiation of a uniformly moving electron due to its transition from one medium into another,"* J. Phys. **9,** 353 (1945).

[47] V. E. Pafomov and I. M. Frank, *"Transition radiation at two parallel interfaces,"* Sov. J. Nucl. Phys. **5,** 448 (1967).

[48] F. J. García de Abajo, *"Relativistic energy loss and induced photon emission in the interaction of a dielectric sphere with an external electron beam,"* Phys. Rev. B **59,** 3095 (1999).

[49] F. J. García de Abajo and A. Howie, *"Retarded field calculation of electron energy loss in inhomogeneous dielectrics,"* Phys. Rev. B **65,** 115418 (2002).

Chapter 2
Integrated experimental setup and gallium nanoparticle growth

2.1 Synopsis

This Chapter is mostly dedicated to the description of the integrated experimental setup developed for nanostructured sample preparation and characterization.

The setup, described in Section 2.3, was based on a modified scanning electron microscope (SEM) equipped with an effusion cell for gallium nanoparticle growth, a liquid-nitrogen cooled cryostat to control sample temperature and a spectroscopic cathodoluminescence (CL) measurement system. The SEM, the cryostat and the effusion cell are described in Subsection 2.3.1, while the CL system and related hyperspectral imaging techniques are detailed in Subsection 2.3.2.

The experimental setup was used for the preparation of gallium nanoparticles. The introduction to the metallic nanoparticle preparation is given in Section 2.2. An investigation of the gallium nanoparticle formation process, based on the light-assisted deposition technique, is detailed in Section 2.4.

2.2 Introduction

For the purposes of nanoparticle preparation and characterization an experimental setup was developed (Figure 2.1). The setup was based on a scanning electron microscope (SEM) as it allows for imaging with nanoscale resolution. The SEM

was additionally equipped with an effusion cell for gallium nanoparticle growth, a liquid-nitrogen cooled cryostat to control sample temperature and a spectroscopic CL measurement system. The setup is described in Section 2.3 of this Chapter. Let us here concentrate on some scientific aspects of metallic nanoparticle preparation.

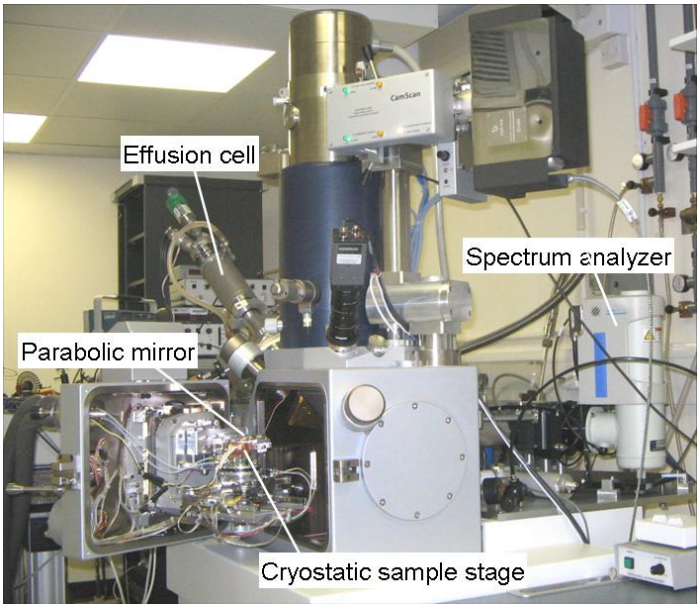

Figure 2.1. Photograph of the integrated system for growth, imaging, cathodoluminescence (CL) study, and optical interrogation of nanoparticles.

Aside from the phase-change memory application that will be discussed in Chapter 3, the preparation of metallic nanoparticles is a technologically important issue for such applications as field-enhanced spectroscopy, catalysis, magnetic nanoparticle memory, and cancer treatment [1–4]. Because the optical and thermodynamic properties of metallic nanoparticles are strong functions of their size [5, 6] it is critical that their production is precisely controlled and highly reproducible.

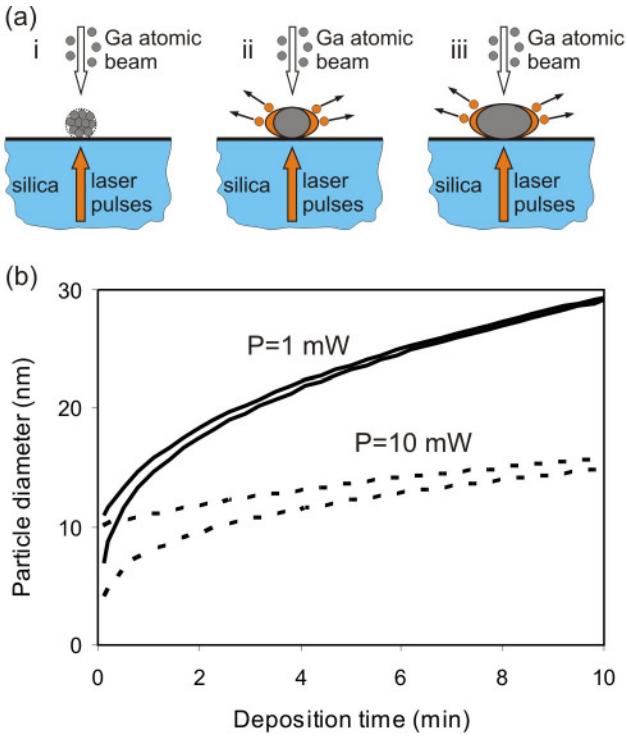

Figure 2.2. (a) Schematic illustration of the light-assisted self-assembly process for gallium nanoparticles: [i] formation of a small cluster, which does not interact with incident IR laser light; [ii] strength of interaction with optical radiation increases with particle aspect ratio, activating selective light-enhanced desorption and light-suppressed adsorption mechanisms; [iii] particle size is controlled by the temperature-, laser power- and atomic beam flux-dependent balance between absorption and desorption. (b) Growth of gallium nanoparticles controlled by light-suppressed adsorption (after Fedotov *et al.* [16]). The dependence of particle diameter on deposition time for 1 and 10 nm seed diameters and laser powers of 1 mW (solid lines) and 10 mW (dashed lines).

Chemical techniques for the preparation of colloidal metallic nanoparticles [7] cannot be used for the fabrication of gallium nanoparticle films because small gallium particles are liquid at room temperature [8]. Epitaxial deposition can typically produce particles with narrow size distributions but only up to a mean diameter of around 5 nm, for larger particles the size distribution is found to be bimodal [9, 10]. A laser-assisted technique for nanoparticle size manipulation, based on surface plasmon excitation and ablation, has been suggested for the post-growth size reduction of sodium particles [11]. Later, this method was developed

to enable the control of nanoparticle size, shape and size distribution using high-power pulsed lasers [12, 13]. Recently, it has also been shown that low power optical excitation can be used to control nanoparticle growth processes. For example, illumination with light at wavelengths in the near-UV to visible range can control the growth of colloidal silver nanoprisms [14], and pulsed IR excitation has been found to control the growth of substrate-supported gallium nanoparticles from an atomic beam [15].

The light-assisted self-assembly process for gallium particles, subject to pulsed infrared laser excitation, proceeds as follows [15, 16]: Deposition from an atomic beam onto a silica substrate cooled to 100 K results in the growth of solid phase nanoparticles. Atomic clusters are initially formed (Fig. 2.2a[i]) and, because gallium wets silica rather well, these grow preferentially across the substrate surface, increasing their diameter-to-height aspect ratio. The IR absorption cross-section of the particles depends strongly on their size and aspect ratio so as they grow the strength of their interaction with the incident laser light increases (Fig. 2.2a[ii]). This increasing absorption activates two processes – 'light-enhanced desorption', whereby IR excitation promotes desorption of atoms from particles' surfaces by breaking bonds within the metal's solid structure, and 'light-suppressed adsorption', whereby the probability of successful binding for new atoms arriving from the atomic beam is reduced in optically excited particles (Fig. 2.2b). The dynamic balance between these processes, which depends on substrate temperature, laser power and atomic beam flux, controls the size and narrows the size distribution of particles during growth (Fig. 2.2a[iii]).

A systematic study of the light-assisted gallium nanoparticle formation process has been conducted in Ref. [17] (detailed in Section 2.4), focusing in particular on the influence of laser power, deposition time and substrate temperature on the size and geometry of the particles obtained.

2.3 Integrated experimental setup for nanoparticle growth and characterization

2.3.1 Modified scanning electron microscope

Scanning electron microscope (SEM)

The experimental setup was based on a scanning electron microscope CamScan CS3200LV (Figures 2.1 and 2.3). The SEM vacuum chamber was under high vacuum pressure: a rotary pump provided rough vacuum, and the pressure of 10^{-6} mbar was achieved with a turbomolecular pump.

The electron gun of the SEM was equipped with an LaB_6 (lanthanum hexaboride) crystal cathode, heated by a current of about 2 A. An LaB_6 cathode provides a more localized source of electrons (which determines the resolution), higher electron emission intensity and extended lifetime in compare with a tungsten cathode. The electron gun produces an electron beam that has a precise kinetic energy (in the range of 1–50 keV) and current (in the range of 20 pA – 10 μA). The electron beam was focused by the system of electron lenses to the spot at the surface of the sample (mounted on an *xyz* translation stage) and scanned by the scan coils across it in a raster (*scanning mode*). Simultaneously the detectors count generated electrons (or photons) given off from each point on the surface to plot a raster image on a monitor screen. The SEM was originally equipped with a secondary electron detector and a backscattered electron detector. All electron images in this work were produced with the secondary electron detector, as it was found to be more suitable for the samples studied in this work. The original cathodoluminescence (CL) system, comprising of a narrow angle light collection mirror and a photomultiplier, was replaced with a self-made CL system, as described in Subsection 2.3.2.

In optional *spot mode* the electron beam is stationary, focused on the sample surface, and can be repositioned manually to allow targeted impact on specific areas of the sample.

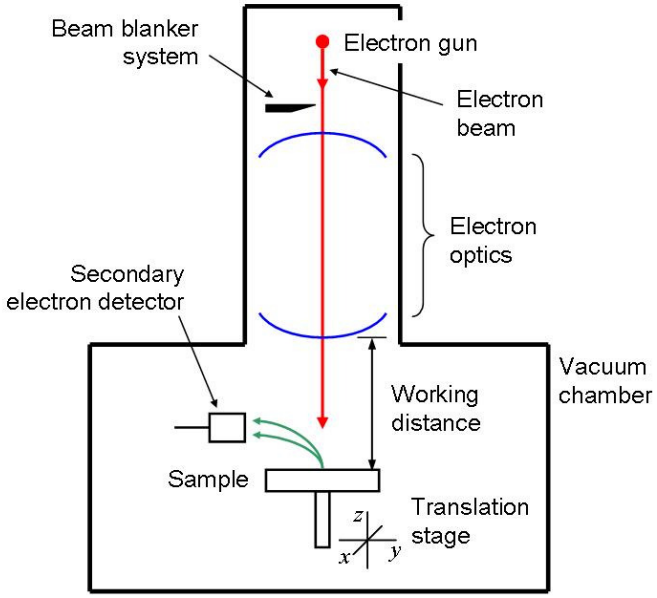

Figure 2.3. Schematic of the SEM.

The current of the electron beam before it hits the specimen could be determined using a retractable Faraday cup. The electron beam could optionally be blanked at a given frequency with the beam blanker system; this facility was used to produce electron beam pulses (Chapter 3).

Spatial resolution of the SEM

The resolving power of an SEM is a function of many parameters, which are required to be optimized to achieve the best resolution. The spot size of the focused electron beam decreases with the increase of kinetic energies of the electrons and the decrease of the electron beam current and the working distance (the distance between the last objective lens and the focal plane). Nevertheless, the detected secondary and backscattered electrons originate from a region larger than the size of the incident electron beam. The size of this region (see interaction volume, Subsection 1.3.1) increases with the increase of the electrons' kinetic energy. In addition, the sensitivity of the electron and photon detectors does not allow using too small an electron beam current.

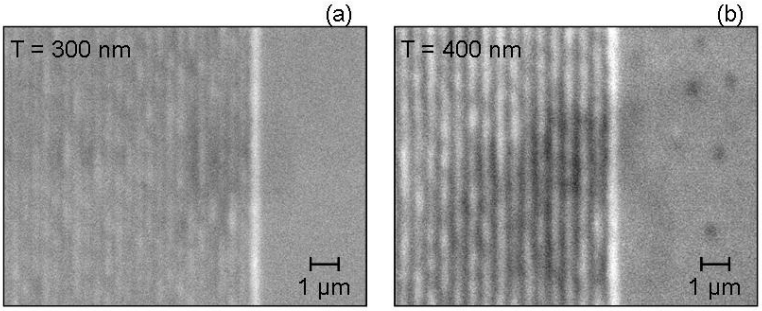

Figure 2.4. Determination of the spatial resolution of the SEM with a 2 keV electron beam (current 390 pA) by imaging gold gratings with the period of 300 nm (a) and 400 nm (b). The image of the 300 nm grating is smoothed while the image of the 400 nm grating shows ribs clearly, therefore the resolution (and electron beam spot size) is about 350 nm.

According to the specification, the ultimate resolution of the CS 3200 microscope with an LaB_6 cathode and secondary electron detector can be up to 2.5 nm. However the samples studied in this work were semi-conductive which reduces the electron imaging resolution somewhat. So the best resolution achieved with a 20 keV electron beam and a current of 50 pA, using a secondary electron detector, was only at the range of 10 nm (this value is approximate since there was no a structure to determine the resolution correctly). The resolution deteriorates further when detecting the CL response. Since the photon yield from metallic nanostructures is not high (in comparison with semiconductor ones) a high electron beam current was required to obtain sufficient photon emission for detection. Also the usage of the light collection mirror increased the working distance. So the resolution with high-energy electrons (20 keV) and the current in the range of nA was about 50 nm, while the resolution with low-energy electrons (2 keV) was above 100 nm. The resolution of this range can be determined correctly using metallic gratings. For instance, the images of two gold gratings with a rib height of 50 nm and a period of 300 and 400 nm, obtained with a 2 keV electron beam (current 390 pA), are shown in Figure 2.4. The image of the 300 nm grating is smoothed and individual ribs can hardly be resolved, while the image of the 400 nm grating shows the ribs clearly, therefore the spatial resolution

is about 350 nm. For low-energy (2 keV) electrons the interaction volume is small and the resolution is equal to the electron beam spot size.

Effusion cell

An CreaTec DFC-40-12 dual filament inverted effusion cell (see Figure 2.5) attached to the SEM was used for the evaporation of gallium for the purpose of the gallium nanoparticle growth. The benefit of an inverted effusion cell (also denoted as "looking-down" type) is that the deposition can be performed with a target directed upwards, hence using the imaging capability of the SEM.

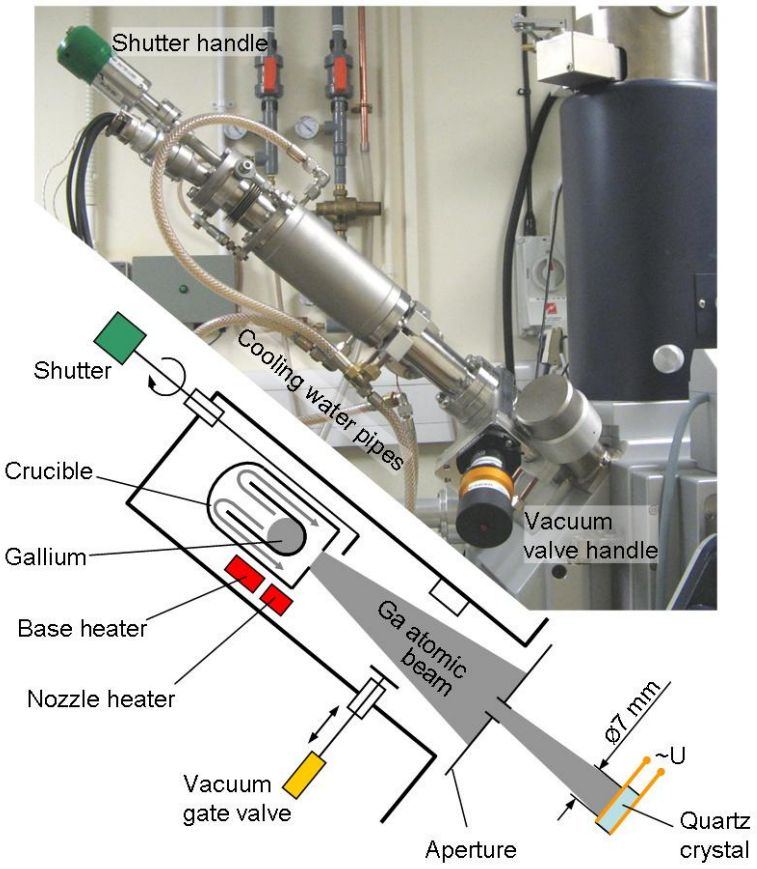

Figure 2.5. Photograph and schematic of the effusion cell and the monitoring quartz crystal microbalance.

The effusion cell contained a crucible made of pyrolytic boron nitride (PBN) where gallium (volume of about 100 mm^3) was loaded. Under the high vacuum the crucible could be heated to temperature of up to 1400 ºC (temperature of the base) with a heating filament, so loaded gallium evaporated slowly (gallium boiling point 2204 ºC). An additional heating filament heated the crucible nozzle to prevent condensation of gallium vapour on it. An aperture, after the effusion cell, formed a narrow gallium atomic beam with a diameter of less than 7 mm on the target in the SEM chamber. The atomic beam could be blocked with a shutter and the effusion cell could be isolated from the SEM chamber with a vacuum gate valve. The crucible was thermally isolated from the other parts of the effusion cell, which were additionally cooled by a water cooling system.

Testing of the effusion cell included the determination of the gallium deposition rate performed with a quartz crystal microbalance*. For a number of temperatures of the base in the range of 1120–1260 ºC the thickness of the gallium layer deposited for 15 min was determined. The deposition rate (nm/min) at each temperature is then found by dividing the determined layer thickness by the deposition time (Figure 2.6a). At the temperature of the base of 1220 ºC the deposition rate was found to be ~0.3 nm/min. This rate is suitable for the growth of gallium nanoparticles [15]. To establish whether the effusion cell's operation was stable at this temperature, the measurement of deposited layer thickness was repeated over a longer period of more than 60 minutes (Figure 2.6b). The

* Quartz crystal microbalance (QCM) is an ultra-sensitive mass sensor [18]. The main part of a QCM is a quartz crystal, which experiences the piezoelectric effect (the production of mechanical stress when an electric field is applied). Applying alternating voltage to the quartz crystal plate induces mechanical oscillation of the quartz crystal. The frequency of oscillation is partially dependent on the thickness of the crystal plate. As some material is deposited on the surface of the crystal, the thickness increases, consequently the frequency of oscillation decreases from the initial value. The frequency change can be correlated precisely to the mass of the deposited material. The thickness of the deposited material can be calculated if the density of the material and the deposited area are known.

experiments revealed the linear dependence of deposited gallium thickness on time. The slope of the linear trend line gives the deposition rate, which was found to be 0.304 nm/min.

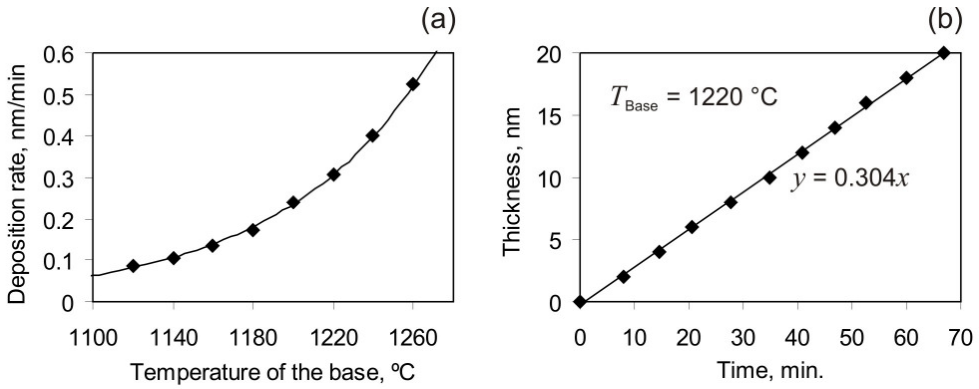

Figure 2.6. Testing of the effusion cell loaded with gallium. (a) Deposition rate versus the temperature of the base (the temperature of the nozzle is 40 ºC higher), approximated with an exponential curve. (b) Deposited gallium thickness versus time at a base temperature of 1220 ºC. The slope of the trend line gives the deposition rate at this temperature.

Cryostat and optical fibre

For the purpose of controlling sample temperature in the range of 90-315 K a Gatan C1003 cryostat (Figure 2.7) was installed in the SEM chamber on the sample translation stage. The cryostat was cooled by externally cooled nitrogen gas via flexible tubing, and the temperature monitoring, tuning and stabilization was achieved by means of a heating element and a platinum resistance temperature sensor controlled by a Gatan ITC-502 temperature controller. Low temperatures were required for the growth and study of gallium nanoparticles which were prepared in the cleaved end face of an optical fibre tip attached to the cryostat (as described in the Section 2.4). The fibre was single mode optical fibre SMF-28, with diameter of core and cladding of 9 and 125 μm, respectively. Before cleaving, the end of the fibre was sputtered with gold to a thickness of 9 nm. It was then cleaved through the gold coating to leave a fibre with a clean end face for gallium deposition and an electrically conductive outer surface to enable SEM imaging without sample charging.

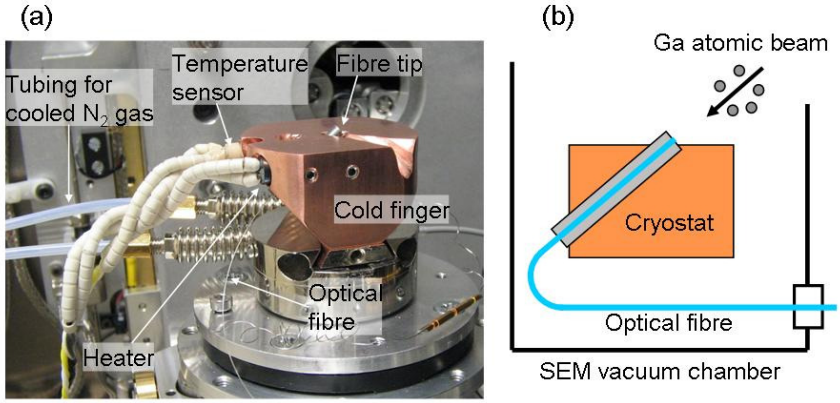

Figure 2.7. Photograph (a) and schematic (b) of the cryostat with optical fibre.

An early stage of the initial testing showed that cooling the sample caused its contamination by moisture condensation, resulting in a thin film of water appearing on the end face of the fibre, which affected the nanoparticles' growth process. A special copper cold finger, with a fibre holder, was fabricated to solve this problem, in such a way that the massive cold finger cooled slower than the lower part of the cryostat, which accepted most of the condensed water. The rest of water condensed on the large surface of the copper cold finger. In addition, the end face of the fibre was sited deepener inside the holder, and hence was shielded from condensation of water.

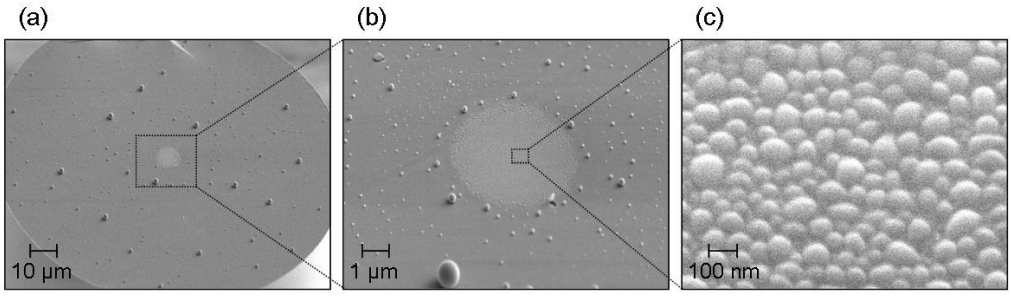

Figure 2.8. Secondary electron images of the cleaved fibre end after a light-assisted gallium deposition. (a) General view; (b) close view of the core area; (c) Inside the core area.

A fibre-based optical diagnostic system (described in detail in Sections 2.4), entering the SEM chamber via a self-made vacuum feedthrough, provided for optical excitation and probing of samples at 1310 and 1550 nm wavelengths.

An example of light-assisted gallium deposition on the end of the optical fibre kept at the temperature of 100 K is given on the Figure 2.8. The scientific aspects of gallium nanoparticle growth are discussed in Section 2.4.

2.3.2 Cathodoluminescence system

In order to be able to monitor light emitted from the sample, while under electron bombardment, a cathodoluminescence (CL) system was used. The original CL system, supplied with the SEM, consisted of a parabolic mirror which collected the emitted light from the sample and directed it (through a transparent mirror in the SEM chamber) to a photomultiplier. Nevertheless the original CL system did not satisfy the requirements for the planned experiments. The mirror had two disadvantages:

1. Narrow light collection angle (solid angle of about 0.1π sr), and hence poor light collection efficiency.
2. Having large height the original mirror did not allow for working distances smaller than about 30 mm, hence greatly reducing the spatial resolution in the imaging.

The photomultiplier did not allow spectral measurements to be performed. Therefore the original CL system was changed to a new one (Figure 2.9), which consisted mainly of a small, wide-angle, parabolic mirror[*] (see Figure 2.10) and a Horiba Jobin Yvon spectrometer.

The new mirror collected backward emitted light[†] over a solid angle of 1π sr, and the working distance was reduced to 15 mm. Due to the smaller depth of field of the mirror its positioning became an important issue. Therefore the mirror was mounted on an *xyz* translation stage: *xy* adjustments were manual, while more

[*] The mirror was designed by M. Bashevoy and manufactured in the Mechanical Workshop, School of Physics and Astronomy, University of Southampton.

[†] Backward direction relative to the electron trajectory

important z adjustment was motorized (taken from the translation stage of the original mirror). The emitted light collected by the mirror (from the area of approximately 100×100 μm^2 on the sample surface) was directed through the transparent window of the SEM to the system of lenses, which focused it on the slit of the spectrometer. The system of lenses was suspended on an xy translation stage. The spectrometer was mounted on a shield attached to the back of the SEM. The spectrometer consisted of a CP140 spectrograph with a concave holographic grating and a Symphony 1024×256 pixels liquid nitrogen-cooled CCD array, allowing the acquisition of spectra in the wavelength region from 350 to 1150 nm. The spectrograph had a nearly linear dispersion of 30 nm/mm on average. The slit width was 0.1 mm, so *the spectral resolution* of the spectrometer was 3 nm.

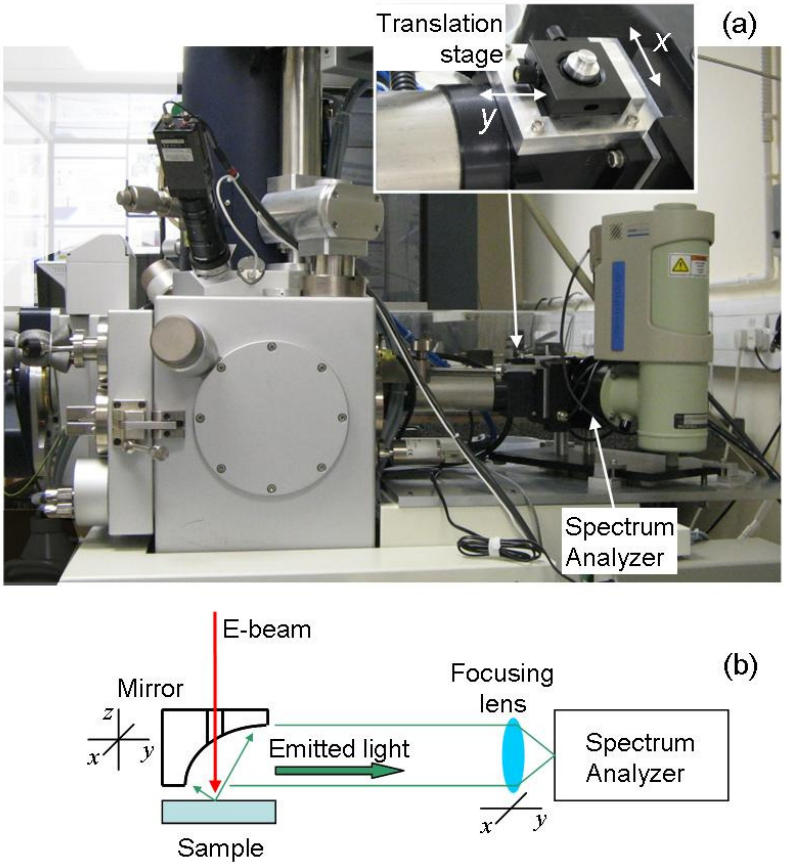

Figure 2.9. Photograph (a) and schematic (b) of the CL system of the SEM.

Before performing any measurements, the CL system required careful positioning of the mirror and the system of lenses to achieve the maximum light collecting efficiency. This alignment was performed using a phosphor screen, which has a high CL emission yield (emission peak at the wavelength of 470 nm) when bombarded with electrons

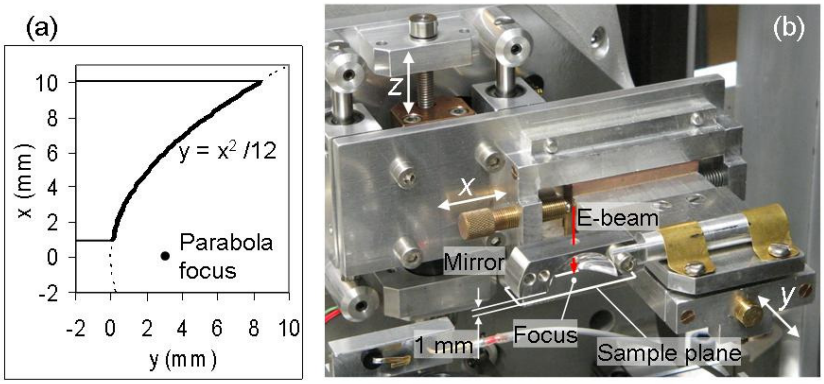

Figure 2.10. Wide-angle parabolic mirror. Surface function in plane (a). Photograph of the mirror mounted on the *xyz* translation stage (b).

Spectral efficiency of the CL system

The spectrometer output signal was measured in counts of the CCD array, therefore the *spectral efficiency* of the CL system was required to determine the actual optical energy emitted by the sample. The efficiency of the CL system mainly depends on the *spectral sensitivity* of the spectrometer. The latter is determined by the efficiency of the grating $E_{Grating}(\lambda)$ and the quantum efficiency of the CCD array $QE_{CCD}(\lambda)$. Both functions were known (Figure 2.11) for the spectrometer. So the spectral sensitivity (in counts/J: counts of CCD array per optical energy in Joules) can be calculated as:

$$E_{Spectrometer}(\lambda) = E_{Grating}(\lambda) \cdot QE_{CCD}(\lambda) / E_{Photon}(\lambda) \qquad (2.1)$$

where $E_{Photon}(\lambda)$ (J) is the energy of a single photon.

Determination of the actual spectral efficiency (intensity calibration) of the entire CL system is a more complicated task. It requires mainly the knowledge of the exact emission spectra from a calibrating sample. N. Yamamoto *et al.* have demonstrated [19] that Drude-like metals (such as aluminum) can be used as

calibrating samples since their light emission, induced by high-energy electron bombardment, is mainly transition radiation which can be precisely calculated.

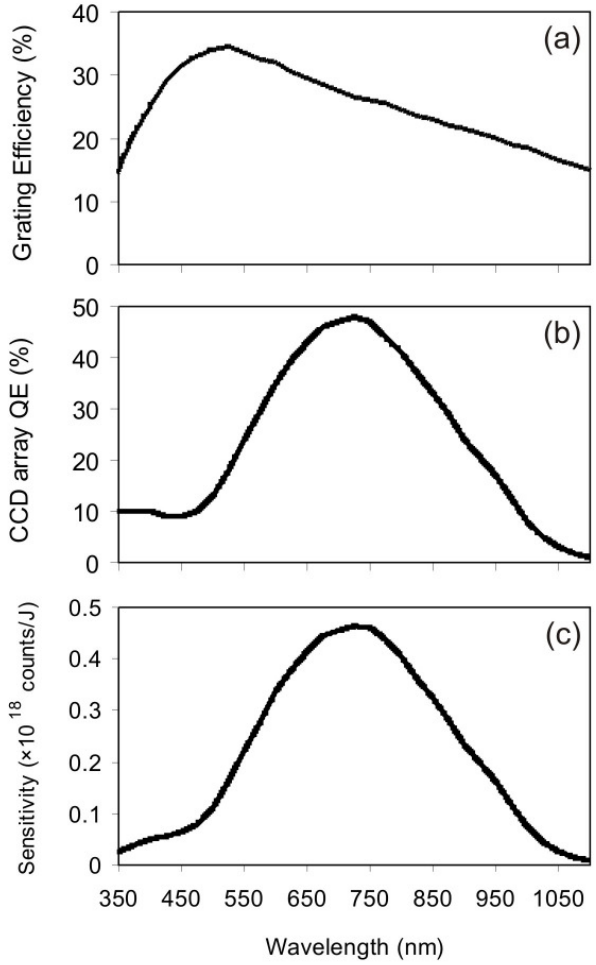

Figure 2.11. (a) Efficiency of the grating. (b) Quantum efficiency of the CCD array. (c) Calculated spectral sensitivity of the spectrometer.

An aluminum film with a thickness of 150 nm (no light can pass through, and the film can be treated as a single vacuum-aluminum interface) was used as a calibrating sample. Its emission spectrum (in counts) was taken on bombardment with 45 keV electron (current of I_b = 2 nA) for t = 30 seconds (Figure 2.12a). The backward transition radiation ($dE/d\lambda$) from the aluminum surface, induced by one incident 45 keV electron (Figure 2.12b), was calculated by formulas given in Subsection 1.3.4. So the relative spectral efficiency of the CL system can be

calculated by simply dividing the observed emission spectrum by the calculated one. The relative spectral efficiency of the CL system is similar to the spectral sensitivity of the spectrometer (Figure 2.12c). Throughout this work all the presented CL spectra are obtained by dividing the observed spectra by the relative spectral efficiency curve of the CL system, so the true CL spectra have units proportional to J/nm.

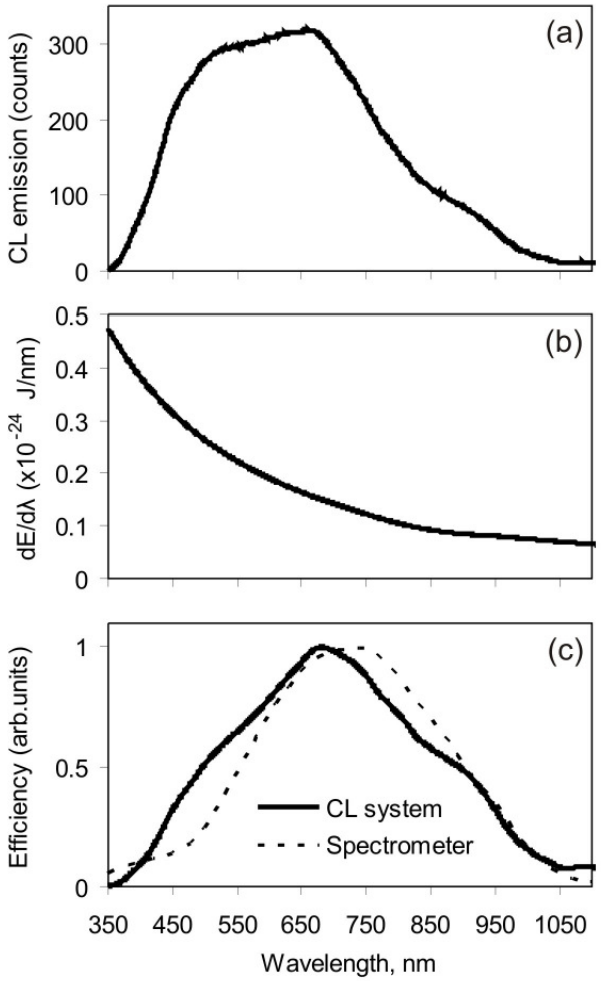

Figure 2.12. (a) Emission spectra from an aluminum film taken at 45 keV. (b) Backward transition radiation from an aluminum surface induced by one incident 45 keV electron. (c) Relative spectral efficiency of the CL system (solid line) compared with the spectral sensitivity of the spectrometer (dashed line) from Figure 2.8c.

The maximum spectral efficiency occurs at the wavelength of 680 nm. To obtain the absolute efficiency of this wavelength it is necessary to calculate the energy of the backward transition radiation emitted within the wavelength range of $\Delta\lambda_{CCD}$ = 0.8 nm (spectral range corresponding to a single CCD element with a length of 26 μm) induced by the same number of electrons as used in the experiment $(I_b t/e)$:

$$E = \frac{dE}{d\lambda}\frac{I_b t}{e}\Delta\lambda_{CCD} = 45\times10^{-15}\,\mathrm{J} \qquad (2.2)$$

The signal from a single CCD element, corresponding to the wavelength of 680 nm, is 310 counts; therefore the *absolute efficiency* of the CL system at 680 nm is about 7×10^{15} counts/J (or 2×10^{-3} counts/photon).

Hyperspectral imaging technique

Hyperspectral imaging (HSI) is a technique for collecting information as a set of images, where each image represents a spectral band. The technique is compatible with scanning electron microscopy where the electron beam scans the sample's surface in a raster while the emission spectra are simultaneously acquired at each point (Figure 2.13).

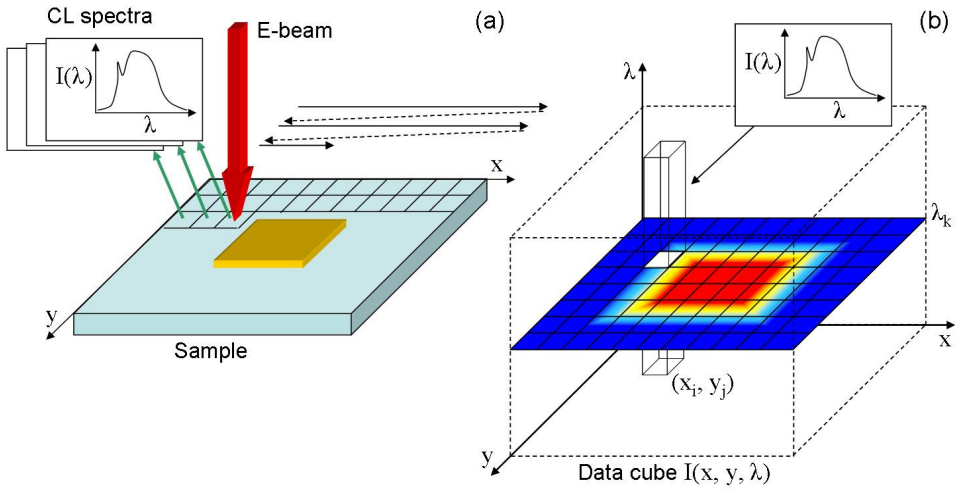

Figure 2.13. Schematic of hyperspectral imaging acquisition (a) and examples of data presentation: plotting emission maps and extracting emission spectra (b).

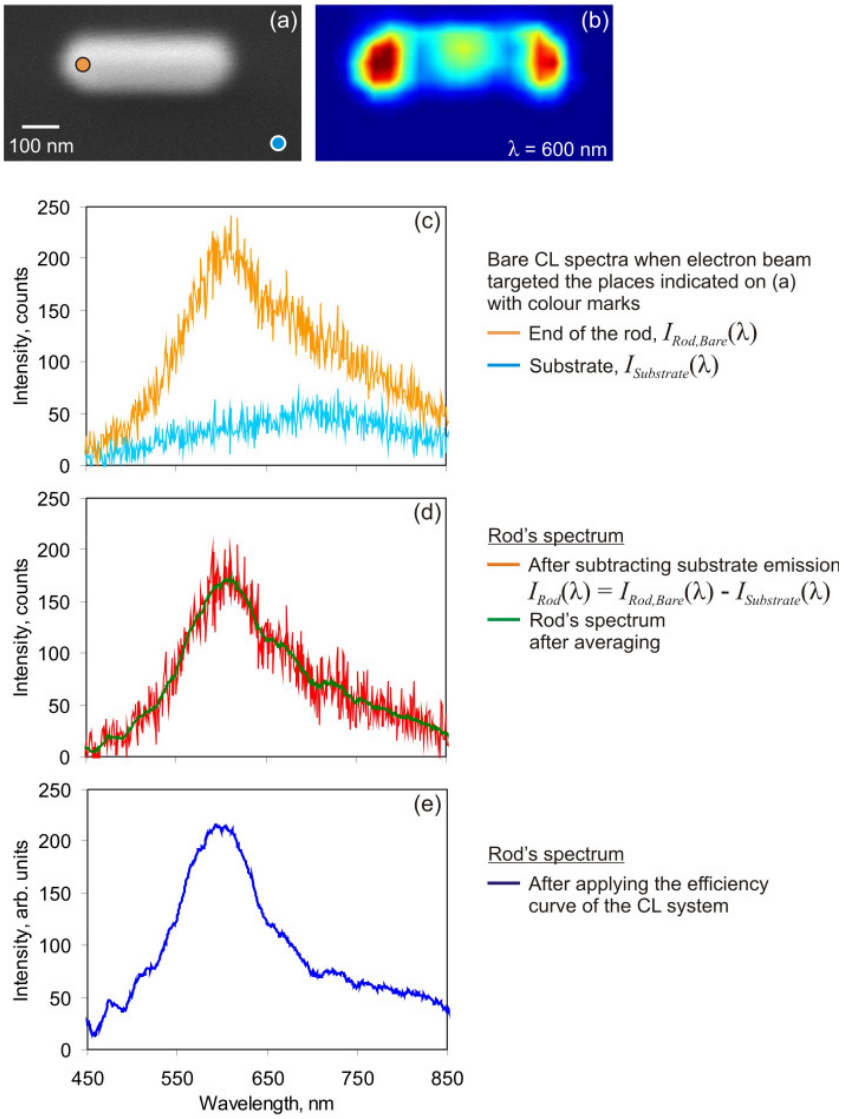

Figure 2.14. An example of a hyperspectral image of a gold nanorod on a silicon substrate. (a) Electron image of the nanorod. (b) CL emission map at the wavelength of 600 nm (intensity integrated in the range of 590–610 nm). (c-e) CL spectra at different stages of processing (CL emission collected for electron beam injection points, marked on (a) with colours.

The sampling of spectra needs to be synchronized with the positioning of the electron beam. In order to achieve this functionality, a LabView control program* was written. The LabView program acquired a hyperspectral image and

* The LabView program was developed by Dr. F. Jonsson.

recorded it to a data file. A specially developed MathLab program* processed the data file to plot emission maps or extract emission spectra.

The maximum acquisition time of an SEM image had a limit of less than about 10 minutes, imposed by the stability of the electron beam and the position of the sample on a nanoscale. This time limited the maximum pixel resolution of a hyperspectral image. Let us estimate this resolution. In the visible and near IR range, the energy emitted per unit wavelength from metallic nanostructures is about 10^{-24} J/nm per incident electron of the keV energy range. With the electron beam current of order of nA, and the efficiency of the CL system specified above, the intensity detected on a single element of the CCD array was not more than 200 counts/sec. The signal-to-noise ratio was sufficient when the number of counts was above 200. Therefore the dwell time of the hyperspectral image is about 1 s, which allows only an image of 26×21 pixels to be acquired.

An example of a hyperspectral image of a gold nanorod on silicon substrate is shown on the Figure 2.14.

2.4 Gallium nanoparticle size control

The setup described in the previous Section allows gallium nanoparticles to be prepared by a light-assisted deposition technique [15]. A systematic study of the gallium nanoparticle formation process was performed, focusing on the influence of the operation parameters on the nanoparticle growth [17].

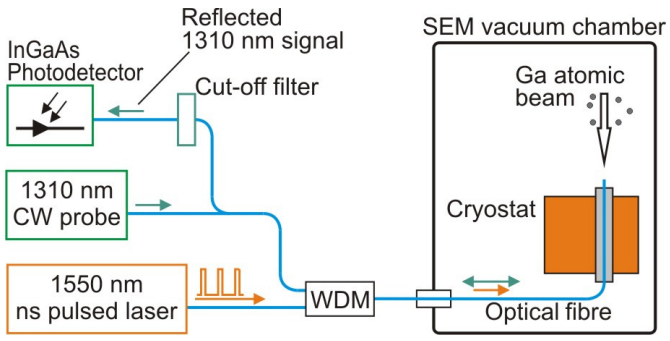

Figure 2.15. Schematic of the setup for gallium nanoparticle growth.

* The MathLab program was developed by Mr. M. Bashevoy

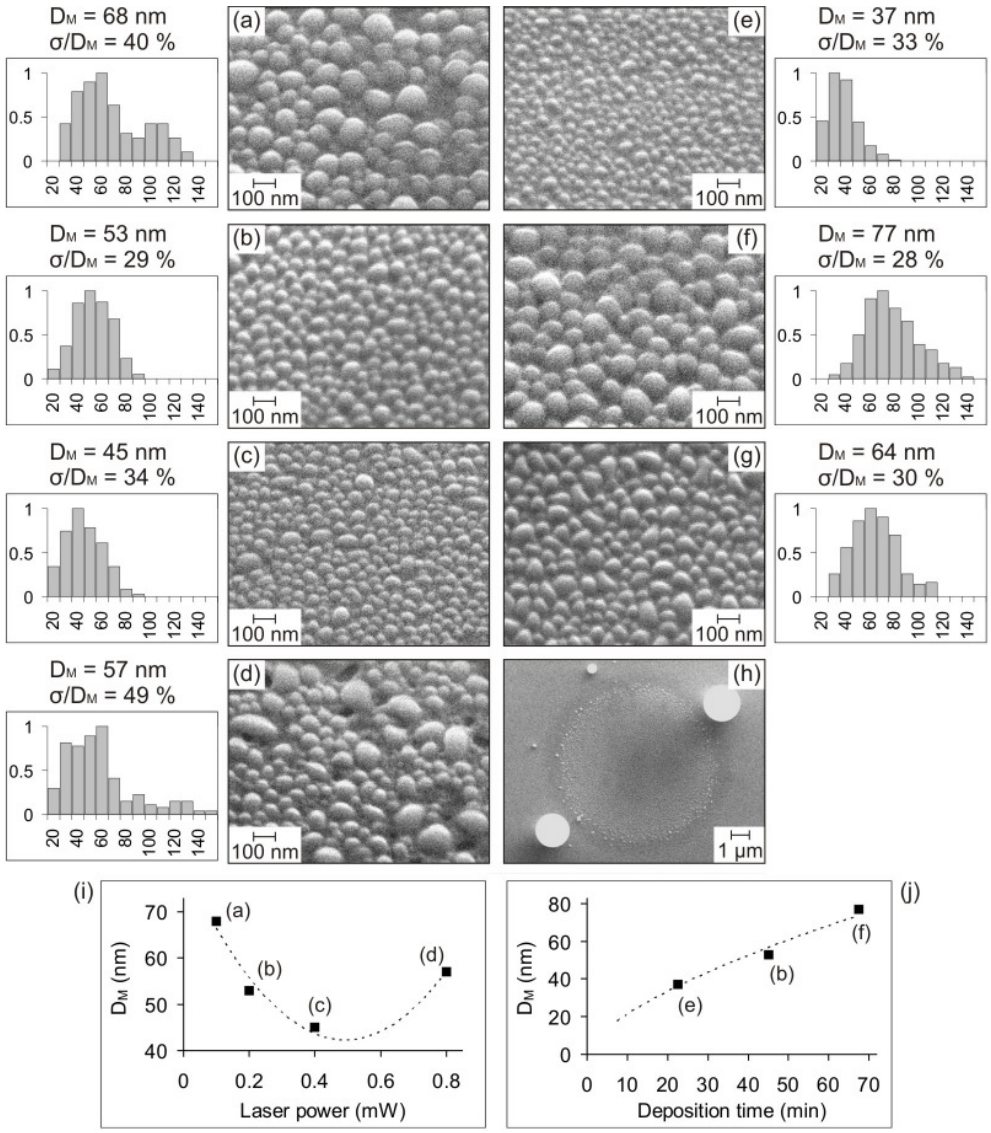

Figure 2.16. Secondary electron images of gallium nanoparticle films obtained under varying conditions of average incident laser power, substrate temperature and deposition time: (a) 0.1 mW, 90 K, 45 min; (b) 0.2 mW, 90 K, 45 min; (c) 0.4 mW, 90 K, 45 min; (d) 0.8 mW, 90 K, 45 min; (e) 0.2 mW, 90 K, 22.5 min; (f) 0.2 mW, 90 K, 67.5 min; (g) 0.2 mW, 105 K, 45 min with corresponding histograms of particle size distribution (diameter in nanometers), mean diameters (D_M), and standard deviations (σ) as a percentage of mean diameter. (h) A typical lower magnification image showing the core area of a fibre tip. (i) Dependence of nanoparticle mean diameter on laser power. (j) Dependence of nanoparticle mean diameter on deposition time.

Nanoparticles were grown for between 22.5 and 67.5 minutes with an atomic beam flux of 0.3 nm/min on the end face of a cleaved single-mode optical fibre kept at a temperature of 90 or 105 K. During growth, the particles were exposed (via the fibre, see Figure 2.15) to light from a pulsed 1550 nm erbium-doped fibre laser producing 3 ns pulses at a repetition rate of 20 kHz with an average power of between 0.1 and 0.8 mW. The reflectivity of the film was monitored using a low power (0.5 mW) continuous-wave 1310 nm diode laser and an InGaAs photodetector. The WDM (Wavelength Division Multiplexer) combined/split signals at different wavelengths. An optical shortpass interference filter stopped the reflected light at 1550 nm from reaching the photodetector.

After growth, the sample stage was brought to room temperature and images of the particle film were acquired (Fig. 2.16). A number of depositions were performed for 45 minutes with a cryostat temperature of 90 K, with average laser powers ranging from 0.1 to 0.8 mW (average intensities of 160 to 1260 $W \cdot cm^{-2}$ in the fibre core, Fig. 2.16a-d). It was found that for laser powers up to 0.4 mW (intensity 630 $W \cdot cm^{-2}$) the mean diameter of the nanoparticles obtained decreased with increasing power (from 68 nm at 0.1 mW to 45 nm at 0.4 mW), in keeping with the theoretical model described in Section 2.1 and in [16]). The size distribution histograms also show that the nanoparticle films obtained at 0.2 and 0.4 mW are considerably more monodisperse than that obtained at 0.1 mW, which has a bimodal size distribution.

Further increasing the incident optical power to 0.8 mW (an average intensity of 1260 $W \cdot cm^{-2}$) produces a disorganized film of partially merged nanoparticles with a median diameter of 57 nm. This is explained by the heating effect of the laser light (not accounted for in the theoretical model): at 0.8 mW it is sufficient to melt the particles during growth, allowing them to coalesce.

At fixed of temperature of 90 K and average laser power of 0.2 mW, further depositions were performed with durations of 22.5 min (0.5 times the 45 min employed above) and 67.5 min (1.5 times 45 min, Figures 2.16e and f). The mean particle diameter is found to increase with deposition time (from 37 nm at 22.5 min to 53 nm at 45 min and 75 nm at 67.5 min), and at the same time the size

distribution narrows (standard deviation as a percentage of mean diameter changes from 33 to 28 %). The theoretical model predicts both of these trends.

An additional deposition was performed at an average laser power of 0.2 mW for 45 min but with an increased substrate temperature of 105 K (Figure 2.16g). While the theoretical model (which assumes solid phase growth) predicts a decrease in particle size with increasing temperature, in the present case it is found that the mean diameter increases from 53 nm at 90 K to 64 nm at 105 K. It is noticeable that the 105 K film contains numerous non-spheroidal particles, this suggests that at this temperature they grew in the liquid phase and were able to begin coalescing (as described above for the 90 K deposition with 0.8 mW laser excitation).

Outside the core area of the fibre, where deposited material is not exposed to laser radiation, the growth process is uncontrolled. Fig. 2.10h shows the core and surrounding area of a typical fibre end face after gallium deposition – in this case a number of large, micrometer size particles are formed outside the core.

2.5 Conclusions

For the purposes of nanoparticle preparation and characterization an integrated experimental setup was developed wherein samples could be prepared under high vacuum, temperature-controlled conditions, then imaged and probed by both optical and electron beams *in situ*. The setup was based on a modified scanning electron microscope equipped with an effusion cell for gallium nanoparticle growth, a liquid nitrogen cooled cryostat to control sample temperature in the 90-315 K range and a spectroscopic CL measurement system.

The described setup was used for the growth and imaging of gallium nanoparticles to study the nanoparticle formation process. An investigation of the factors affecting the formation of gallium nanoparticles, from an atomic beam by light-assisted self-assembly, has been performed. In keeping with a model based on a combination of light-enhanced desorption and light-suppressed adsorption, experiments reveal a decrease in mean particle diameter (from 68 to 45 nm) with increasing infrared substrate excitation intensity (from 160 to 630 $W \cdot cm^{-2}$) during

deposition, and the production of larger particles with a narrower size distribution for longer deposition times.

2.6 References

[1] G. Scmid, *"Nanoparticles: From theory to application,"* Wiley-VCH, 2004.

[2] C. Dupas, P. Houdy, and M. Lahmani, *"Nanoscience: nanotechnologies and nanophysics,"* New York: Springer, 2007.

[3] N. Sanvicens and M. P. Marco, *"Multifunctional nanoparticles – properties and prospects for their use in human medicine,"* Trends in Biotechnology **26**, 425 (2008).

[4] R. Ferrando, J. Jellinek, and R. L. Johnston, *"Nanoalloys: From theory to applications of alloy clusters and nanoparticles,"* Chem. Rev. **108**, 845 (2008).

[5] M. Wautelet, *"Estimation of the variation of the melting temperature with the size of small particles, on the basis of a surface-phonon instability model,"* J. Phys. D **24,** 343 (1991).

[6] P. C. Wu, T. Kim, A. S. Brown, M. Losurdo, G. Bruno, and H. O. Everitt, *"Real-time plasmon resonance tuning of liquid Ga nanoparticles by in situ spectroscopic ellipsometry,"* Appl. Phys. Lett. **90,** 103119 (2007).

[7] G. A. Ozin, *"Nanochemistry: a chemical approach to nanomaterials,"* Cambridge: RSC publishing, 2005.

[8] A. Di Cicco, *"Phase transitions in confined gallium droplets,"* Phys. Rev. Lett. **81**, 2942 (1998).

[9] E. Sondergård, R. Kofman, P. Cheyssac, and A. Stella, *"Production of nanostructures by self-organization of liquid Volmer-Weber films,"* Surf. Sci. **364,** 467 (1996).

[10] H. Brune, *"Microscopic view of epitaxial metal growth: nucleation and aggregation,"* Surf. Sci. Rep. **31,** 125 (1998).

[11] W. Hoheisel, U. Schulte, M. Vollmer, R. Weidenauer, and F. Träger, *"Ablation of metal particles by surface plasmon excitation with laser light,"* Appl. Surf. Sci. **36**, 664 (1989).

[12] T. Wenzel, J. Bosbach, A. Goldmann, F. Stietz, and F. Träger *"Shaping nanoparticles and their optical spectra with photons,"* Appl. Phys. B **69**, 513 (1999).

[13] J. Bosbach, D. Martin, F. Stietz, T. Wenzel, and F. Träger *"Laser-based method for fabricating monodisperse metallic nanoparticles,"* Appl. Phys. Lett. **74**, 2605 (1999).

[14] R. Jin, Y. W. Cao, C. A. Mirkin, K. L. Kelly, G. C. Schatz, J. G. Zheng, *"Photoinduced conversion of silver nanospheres to nanoprisms,"* Science **294**, 1901 (2001).

[15] K. F. MacDonald, V. A. Fedotov, S. Pochon, K. J. Ross, G. C. Stevens, N. I. Zheludev, W. S. Brocklesby, and V. I. Emel'yanov, *"Optical control of gallium nanoparticle growth,"* Appl. Phys. Lett. **80,** 1643 (2002).

[16] V. A. Fedotov, K. F. MacDonald, V. I. Emel'yanov, and N. I. Zheludev, *"Light-controlled growth of gallium nanoparticles,"* J. Appl. Phys. **93,** 3540 (2003).

[17] A. I. Denisyuk, K. F. MacDonald, N. I. Zheludev, and F. J. García de Abajo, *"Towards femtojoule nanoparticle phase-change memory,"* Jpn. J. Appl. Phys. **48**, 03A065 (2009).

[18] J. W. Grate, *"Acoustic wave microsensor arrays for vapor sensing,"* Chem. Rev. **100,** 2627 (2000).

[19] N. Yamamoto, H. Sugiyama, and A. Toda, *"Cherenkov and transition radiation from thin plate crystals detected in the transmission electron microscope,"* Proc. R. Soc. Lond. A **452,** 2279 (1996).

Chapter 3
Gallium nanoparticle as a memory element

3.1 Synopsis

Electron beam addressed nanoparticle phase-change memory has been demonstrated: the digital information is written in the phase state of gallium nanoparticles by electron beam excitation, and readout via measurements of their cathodoluminescent (CL) emission.

An introduction to nanoparticle-based switches and memory elements, as well as discussion of the potential of CL as a probing tool, is given in Section 3.2. The study of CL properties of bulk gallium in solid and liquid phases is described in Section 3.3. It is demonstrated in Section 3.4 that the phase state of bistable gallium nanoparticles, controlled by optical or electron beam excitations, can be identified via measurements of their CL emission. Selective addressing of 50-particle elements within a nanoparticle film is demonstrated in Section 3.5. A suggestion to enhance CL readout contrast for the nanoparticle phase-change memory by employing nanoshells, as opposed to homogenous nanoparticles, is proposed in Section 3.6.

3.2 Introduction

The ultimate goal of nanophotonics, and its sub-field of plasmonics, is to create devices smaller than, or comparable in size to, the wavelength of the signals they

handle (a relationship of proportions that is easily achieved in microelectronics). This goal is particular important for data processing and transport applications [1–4]. Such technologies will obviously require nanoscale components for optical switching and data storage.

Numerous approaches have been considered to realize such functionalities. For switching and signal modulation these range from photoinduced carrier excitation in quantum dots [5] to third order nonlinear switching augmented by plasmonic resonances in metallic nanoparticles [6], and enhanced photoinduced effects in nanoparticle composite media [7, 8].

The optical data storage industry is currently dominated by chalcogenide phase-change media (which can be switched between optically distinguishable crystalline and amorphous states using laser pulses) in the form of CD, DVD and Blu-ray disks. There is now rapidly growing interest in phase-change materials for next-generation nanoscale optical and electronic switching and memory applications due to their potential to address growing challenges of size and power consumption, and to enable innovative photonic and plasmonic functionalities [9–11].

Encoding information in a nanoscale volume of material requires a significant change in the absorption or refraction of that volume in response to external control excitations and such changes can be achieved in certain materials via a phase-change. For instance, vanadium dioxide nanoparticles are found to show a photoinduced insulator-to-metal transition within a time scale of about 100 fs [12]. Light induced phase-change switching has also been demonstrated using gallium nanoparticles [13]. Indeed, gallium can exist in several phases with markedly different optical properties, ranging from those of the almost semiconductor-like, partially covalent solid α phase, to those of the highly metallic liquid [14, 15]. The solid α phase is not normally found in nanoparticles [16], but these exist in a variety of other crystalline phases known as β, δ, ε and γ gallium, which have optical properties between those of the α and liquid phases [17] (see Section 1.4.3).

Phase transitions in nanoparticles require low energy. For example, to convert a spherical 50 nm diameter gallium particle from the β(solid) to the liquid

phase requires energies in the femtojoule range (based on latent heat values from [17]). Even less energy is required for solid-to-solid structural transformations in gallium. Indeed, the δ and β crystalline phases are only separated by 3×10^{-4} eV/atom [17], which suggests the possibility of few- or even single-photon per particle switching [10].

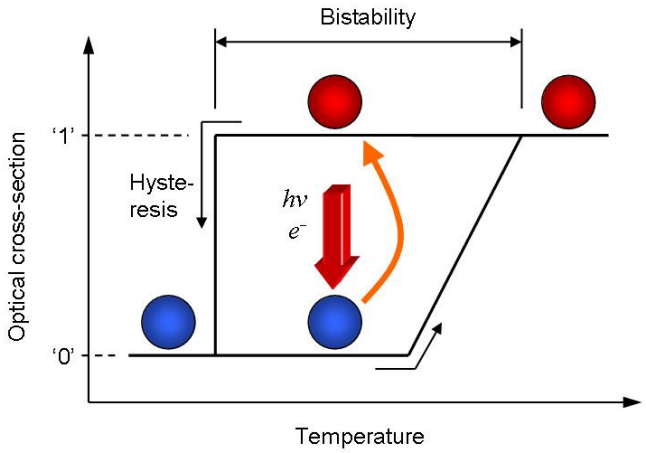

Figure 3.1. Phase-change optical functionality in a nanoparticle: schematic dependence of optical cross-section on temperature for a nanoparticle undergoing a phase transition between states '0' and '1'. The bistability required for memory applications results form a broad thermal hysteresis in the transition. A particle that is within the hysteresis loop can undergo excitation-induced phase transitions.

Of crucial importance to the memory functionality of metallic nanoparticles is the nature of the phase transition process itself (Figure 3.1). In contrast to bulk materials, phase transitions in nanoparticles are characterized by a wide thermal hysteresis where 'reverse' transitions from high- to low-temperature phases occur at lower temperatures than the corresponding 'forward' transitions, thus creating a region where both phases are stable [18–20] (see Subsection 1.4.2). In the case of gallium nanoparticles this region of bistability can be up to 100 degrees wide, providing a solid base for phase-change memory functionality [21].

Another important question is that of the minimum particle size for which 'conventional' phase transitions remain (before atomic cluster behaviors take over). The theoretical lower limit for gallium particle diameter is 3–4 nm [22]. At

this size, if each particle within a close-packed planar array could be addressed individually as binary memory elements, a storage density approaching 50 Tbit/in^2 could be achieved (for comparison, Blu-ray disks offer 0.015 Tbit/in^2).

Binary all-optical memory functionality has recently been demonstrated using a gallium nanoparticle film (with the whole film of some 10000 of particles on the end face of a single mode optical fibre core acting as a single memory element [21]). Also, a higher-base logic quaternary all-optical memory has been demonstrated for a single 100 nm gallium nanoparticle isolated in a nano-aperture at the tip of a tapered, metal-coated optical fibre [23]. In these schemes, single laser pulses (~1 pJ energy per particle) induce lower- to higher-temperature structural transformations in the particles (at a temperature within the hysteresis loop) to 'write' information to the memory element, and 'readout' is achieved through reflective measurements of the particles' linear or nonlinear optical properties.

An electron beam, which can be focused on the nanoscale (far below the diffraction limit for an optical beam), might be used to address individual particles within a nanoparticle film, providing energy to record data by inducing structural transitions and enabling readout via measurements of CL emission (Figure 3.2). Indeed, luminescent detection of phase state is used for insulator materials [24] and CL has been used to probe electron beam induced memory effects in semiconductors [25, 26].

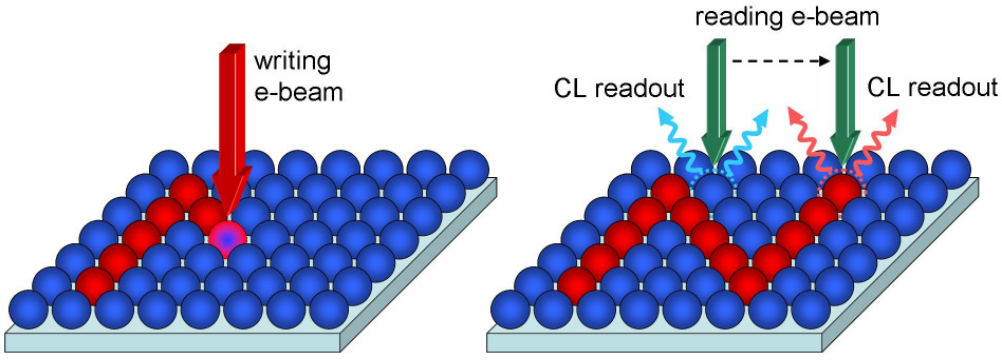

Figure 3.2. Schematic illustration of (a) writing and (b) CL readout processes in high-density electron beam addressed phase-change nanoparticle memory. Phase switching is induced using a higher energy electron beam; CL emission is excited at lower energy.

The electron beam induced switching of a large planar ensemble of gallium nanoparticles (~10000 particles over an area of 60 μm^2), and associated CL identification of their phase (memory) state has recently been demonstrated in [27] (detailed in Section 3.4). A further study of electron beam addressed gallium nanoparticle phase-change memory, published in [28], includes the bulk gallium's CL emission characteristics and the demonstration of selectively addressed 50-particle memory elements within a nanoparticle film (Sections 3.3 and 3.5, respectively). The following section details the investigation of the bulk gallium's CL properties. All experiments reported in this Chapter were performed on the integrated setup described in Section 2.3.

3.3 Cathodoluminescence of bulk gallium

A preliminary investigation of electron beam induced light emission from bulk gallium was performed. With a deposition rate of less than 1 nm/min, the effusion cell was not suitable for the fabrication of a bulk sample. Therefore such a sample was prepared by placing a 1 mm diameter droplet of high-purity (99.9999%) liquid gallium (melting point = 303 K) on the surface of the SEM's cryostatic sample stage (see Figure 3.3a). Under vacuum conditions, the stage was cooled to 253 K to solidify the droplet and then heated at a rate of 2.5 K/min. Between 283 and 313 K, CL emission spectra were continuously recorded by scanning a 12×9.6 μm^2 region of the droplet with a 40 keV, 2.9 nA electron beam. At the 303 K melting point of the metal's solid α phase an increase in light emission at all wavelengths (up to 50 % in the 550-650 nm range) was observed. Figure 3.3a shows representative CL emission spectra for the solid and liquid phases.

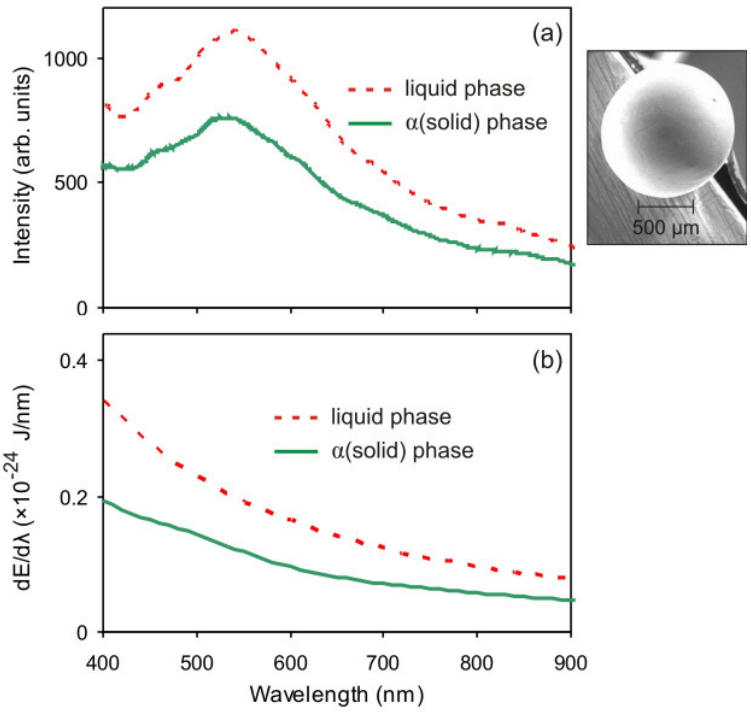

Figure 3.3. (a) Experimental CL emission spectra (obtained with a 40 keV electron beam) for bulk gallium in the solid α (blue line) and liquid (red dashed line) phases. Secondary electron image of the gallium droplet is shown on the right. (b) Calculated transition radiation spectra (emitted energy induced by one incident electron) for a 40 keV electron travelling perpendicular to α and liquid gallium/vacuum interfaces.

In metals, transition radiation plays the major role in light emission induced by electron bombardment. Plasmon emission, decoupled by surface roughness features, can also contribute [29]. In the case of gallium there may also be a contribution from recombination emission, since the solid α phase shows interband transitions via which light can be emitted between 520 and 1000 nm (2.4–1.25 eV), with a maximum at 540 nm (2.3 eV) [30]. Liquid gallium retains some atomic order similar to that of the solid phase [17] and may therefore possess transition bands at similar wavelengths.

Calculations of transition radiation emission, integrated over a hemispherical solid angle of 2π in the backward direction relative to the electron trajectory, were performed using formulae [31] that were described in Subsection 1.6.2 for 40 keV electrons travelling perpendicular to solid and liquid

gallium/vacuum interfaces (Fig. 3.3b). Dielectric functions used in the calculations were obtained from [32] for α-gallium and from [33] for liquid Ga (presented in Subsection 1.4.3). In keeping with the experimental results, the calculated emission spectra show markedly higher emission from the liquid phase at all wavelengths and reproduce the observed increasing strength of emission with decreasing wavelength. The experimentally observed emission peak at 550 nm does not appear and perhaps is associated with recombination emission resulting from interband transitions around this wavelength.

Note that, while the maximum penetration depth of 40 keV electrons into gallium is around 7 μm (calculated using the model [34] described in Subsection 1.5.3), light emission can only come from a surface layer with a thickness limited by the optical skin depth, which is 15 nm for α-gallium and 7 nm for the liquid phase in the 500–550 nm wavelength range. This fact is crucial to the functionality of individual nanoparticles as memory elements.

3.4 Luminescence readout of nanoparticle phase state

Films of gallium nanoparticles were grown on the end faces of cleaved single-mode fibres using the light-assisted self-assembly technique [35] (detailed in Section 2.4). With the fibre tip held at a temperature of 100 K, gallium was deposited at 0.3 nm/min for 50 min (giving a mass thickness of 15 nm) while 1 μs pulses from a 1550 nm FP (Fabry-Perot) diode laser (19 mW, 1 kHz repetition rate) were launched into the fibre from outside the SEM chamber (see Figure 3.4a). This process produces a monolayer of particles with a mean diameter of 60 nm on the optical core area of the fibre end face (see Figures 3.4b and 3.4c). The integrated experimental system then allows for the particles to be imaged *in situ* by the SEM and for their CL to be probed. Furthermore, the nanoparticle films' reflective optical properties can be studied via the fibre, and phase transitions can be stimulated in the particles by both optical and electron beam excitations.

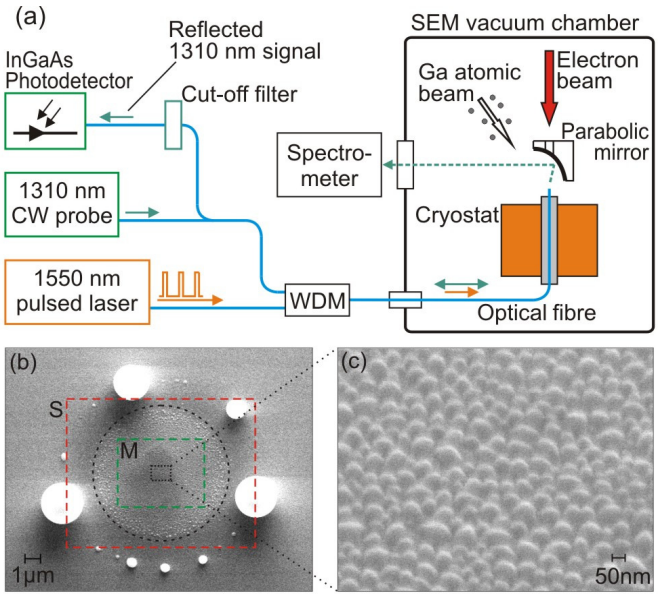

Figure 3.4. (a) Integrated system for growth, imaging, CL study, and optical interrogation of gallium nanoparticle films. (b) Secondary electron image of a fibre end face showing the optical core area (dashed circle) where 60 nm particles, shown at higher magnification in (c), are formed during deposition. The dashed squares indicate the areas exposed to electron beam excitation for CL measurements (M) and to achieve phase switching (S).

For the purpose of encoding information in the structural phase of nanoparticles, excitation-induced phase switching is most efficiently performed in the proximity of the phase transition temperature. To identify this temperature for the present case, the reflectivity of the nanoparticle film was recorded as a function of temperature between 100 and 305 K using a continuous-wave 0.5 mW beam from a 1310 nm diode laser (see Figure 3.5a).

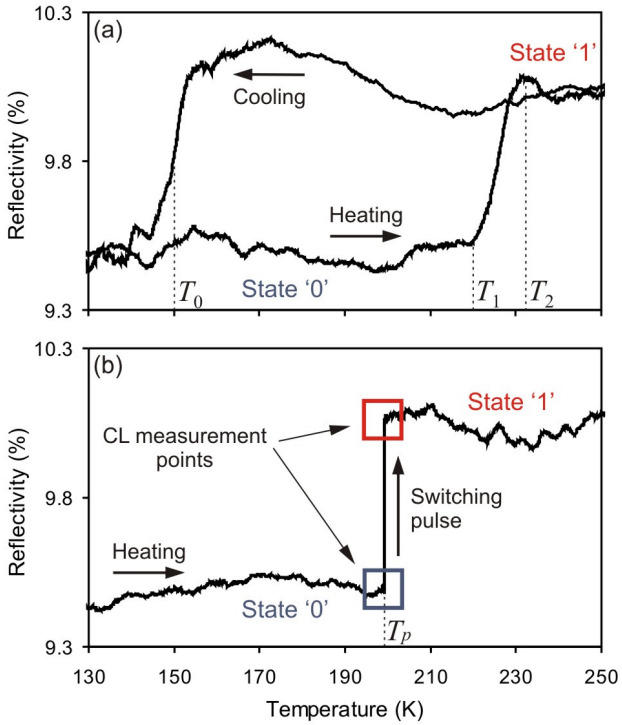

Figure 3.5. (a) Reflectivity hysteresis of a gallium nanoparticle film on a fibre end face (measured via the fibre) as function of cryostat temperature. (b) Gallium particle film reflectivity as a function of increasing temperature, showing abrupt excitation-induced phase (memory state) switching at T_p = 200 K ($T_0 < T_p < T_1$). CL measurements are made immediately before and after the induced transition.

Phase transitions in bulk materials are characterized by a discontinuous change in the state of the body, a sudden (irreversible) rearrangement of the crystalline lattice at a specific temperature. In nanoparticles, however, transitions from lower to higher energy phases proceed through a surface-driven dynamic coexistence of forms across a size-dependent range of temperatures [19, 20]. When the two forms involved have different dielectric coefficients, this gives rise to a continuous change in optical properties, such as the smooth step change in reflectivity between $T_1 = 220\,\mathrm{K}$ and $T_2 = 233\,\mathrm{K}$ shown in Fig. 3.5a, which is associated with the melting of gallium's β crystalline phase [16, 17]. The recorded transition temperature is lower than the listed β-gallium melting point of 257 K due to a combination of size-dependent melting point suppression and a

systematic offset linked to the relative positioning of the sensor and fibre tip. With decreasing temperature, the reverse phase transition occurs only after substantial overcooling at $T_0 = 150\,\mathrm{K}$. This phase bistability underpins the gallium particles' memory functionality [21, 23] (peculiarities of phase transitions in nanoparticles are discussed in Subsection 1.4.2).

To demonstrate CL readout of nanoparticle phase (memory) state, a series of experiments was performed. In each case, the nanoparticle film was placed initially in the low reflectivity ('0' logic) solid phase by cooling to the minimum available temperature of about 100 K. Its temperature was then increased and fixed at a point $T_p = 200\,\mathrm{K}$ just below the phase transition point and a CL spectrum was obtained by scanning a 5.5×4.4 μm^2 region within the core area (square M in Figure 3.4b) with a low current (< 2.3 nA) electron beam. The nanoparticle film was then switched to the high reflectivity ('1' logic) liquid state by either optical or electron beam excitation. In the former case, a single 1 μs pulse from the 1550 nm diode laser, with a fluence of ≥ 0.3 fJ/nm^2, was used to induce a structural phase-change. In the latter, switching was initiated by a single 40 ms, 5 keV electron beam scan across a 12×9.6 μm^2 area encompassing the core (square S in Figure 3.4b) with a beam current of ≥ 20 nA (a fluence of ≥ 35 fJ/nm^2). A second CL measurement was then performed. Throughout this process, and with increasing temperature after the second CL measurement, the reflectivity of the samples was monitored to ensure that the particles' phase state was not switched by the electron beam during the first CL measurement and to verify that it was switched abruptly by the excitation pulse prior to the second (see Figure 3.5b). The particle film was reset to the solid '0' state by cooling it to below 150 K (recent work has suggested that nanosecond optical pulses could be used to achieve this 'memory erase' function at a fixed temperature [36]).

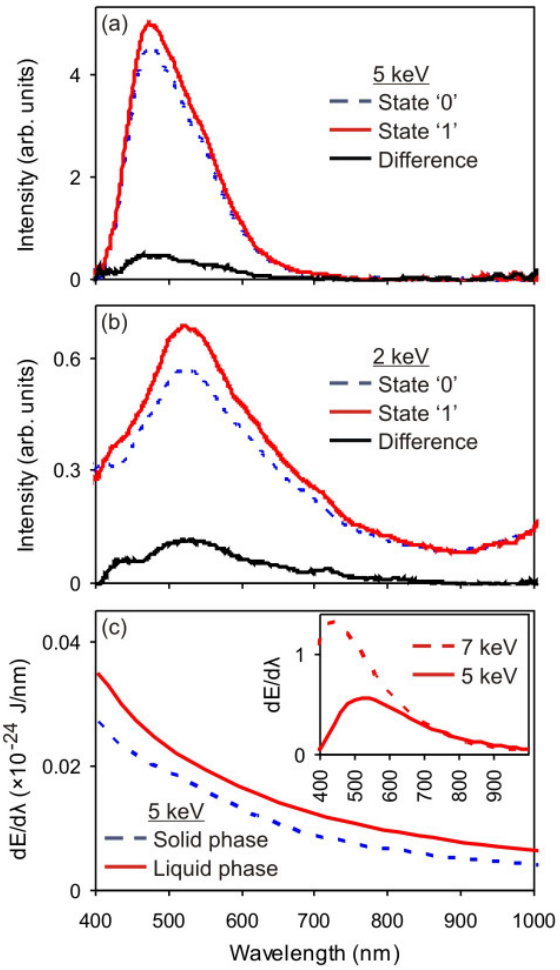

Figure 3.6. [(a) and (b)] CL spectra of gallium nanoparticle films in solid '0' and liquid '1' states together with the difference spectra. (a) CL spectra obtained with a 5 keV, 2.3 nA electron beam, after subtraction of silica luminescence. (b) CL spectra obtained with a 2 keV, 1 nA beam (silica contribution negligible). (c) Calculated backward transition radiation emission induced by a 5 keV electron from 15 nm thick homogenous solid and liquid gallium films on silica substrates. The inset shows total CL emission (in all directions) from a freestanding, 60 nm diameter spherical particle of liquid gallium in vacuum, for 5 and 7 keV electron trajectories through the centre of the particle.

CL measurements were performed at 5 and 2 keV electron energies, with beam currents of 2.3 and 1 nA, respectively. Results are shown in Figures 3.6a and 3.6b together with corresponding difference spectra relating to the increase in emission associated with the solid-to-liquid transition in the nanoparticles. The

absolute signal intensity is higher at 5 keV because the electrons have a longer penetration depth; however, at this voltage, the recorded spectra contain a significant component relating to the luminescence of the fibre, excited by electrons having passed through the gallium nanoparticle film. This artifact was eliminated via measurements on a bare fibre tip. At 2 keV, the silica luminescence contribution is negligible and the relative change in signal magnitude on phase switching is larger (20 % as compared to 11 %). The spectral peaks redshift and broaden with decreasing acceleration voltage, from 475 +80/−35 nm at 5 keV to 520 +130/−100 nm at 2 keV.

Light emission from metal nanostructures, induced by electron bombardment, results from a complex combination of several mechanisms; transition radiation and plasmon-mediated emission are dominant [29]. There may also be a contribution from recombination emission, because solid phases of gallium show interband transitions (at 520–1000 nm for α-Ga [30], and 400, 700, and 950 nm for β-Ga [37]) via which light can be emitted. Liquid gallium retains some atomic order, similar to that of the metastable solid phases [17], and may therefore possess transition bands at similar wavelengths. Numerical models can qualitatively reproduce certain characteristics of the observed emission spectra but no single model can currently account for the full complexity of electron-induced radiation emission from a closely-spaced ensemble of truncated spheroidal particles on a substrate (particularly where the exact particle size and geometry are functions of phase state). To a first approximation, a closely packed nanoparticle monolayer may be treated as a homogenous film of equivalent mass thickness (15 nm in the present case). Figure 3.6c shows backward transition radiation emission (integrated over a solid angle of 2π), calculated using formulae [38] from Subsection 1.6.2, resulting from 5 keV electron beam excitation of solid and liquid gallium films on silica substrates. Dielectric constants for β-gallium are not available, so values for fractionally disordered α-gallium with optical conductivity similar to β-gallium [39] were used for the solid phase. Dielectric constants for liquid gallium were taken from [33]. This calculations show higher emission from the liquid phase, as observed experimentally, but do not reproduce the emission peaks, shown in Figures 3.6a and 3.6b, because the model does not

account for plasmon-mediated emission. Calculations of the total CL emission (in all directions) from a single, freestanding, 60 nm spherical liquid gallium particle in vacuum, performed using the boundary element method [40] (see Subsection 1.6.3), illustrate the experimentally observed trend for redshifting and broadening of the signal peak with decreasing electron acceleration voltage (see inset to Figure 3.6c). However, such calculations are sensitive to the assumed particle geometry and do not account for interactions between neighboring particles.

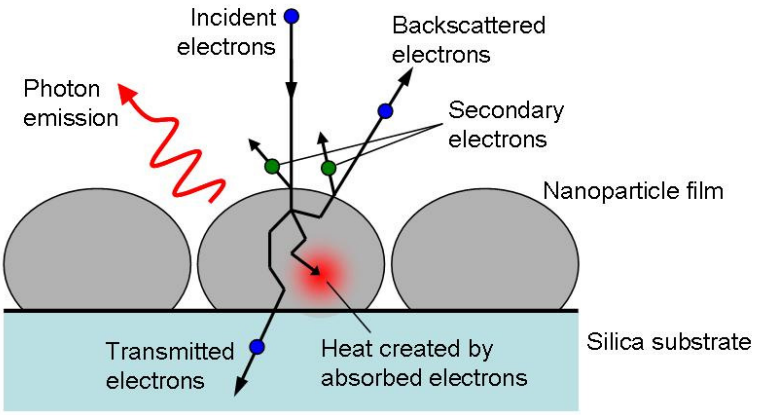

Figure 3.7. Schematic of incident electrons-nanoparticle interactions.

The operational energy requirements of nanoparticle-based phase-change memory elements are potentially very low. In a nonvolatile format, they require no holding power and the thermodynamic minimum switching requirement for a β-to-liquid transition in a 60 nm diameter spherical particle, 30 K below its melting point, is about 35 fJ (based on specific and latent heat values from [17]). While the incident energies per particle used in the present studies are at least two orders of magnitude higher than this, only a small fraction of the incident energy is actually absorbed by the particle. The optical absorption coefficient at 1550 nm, for a film of closely packed 60 nm diameter particles, is estimated to be less then 10 %, using the model [41] presented in Subsection 1.3.2. Whereas the energy absorption coefficient for a 5 keV electron beam in a homogenous gallium film, of the equivalent mass thickness, is of the order of 1 % (according to the model [34] described in Subsection 1.5.3). Also in the latter case not all of the absorbed

energy will go towards heating the particle: some is reradiated in the form of secondary electrons and photons. The schematic of incident electrons-nanoparticle interactions is shown on Figure 3.7.

3.5 Electron beam addressing and readout of high-density nanoparticle phase-change memory

While, in the previous Section, switching and readout was demonstrated on a large ensemble of nanoparticles; the proof-of-principle of nanoparticle phase-change memory requires, in addition, the demonstration of addressing individual particles, or at least group of particles.

For this purpose a nanoparticle film was prepared under the same conditions as described in the previous Section (Figure 3.8a). Data was encoded in the structural phase of the particles: β-solid phase = logic state '0', liquid phase = logic state '1'. Here a 'volatile' mode of operation was demonstrated, with the holding power required to retain written data provided by a 3 mW continuous-wave (CW) 1550 nm DFB (distributed-feedback) diode laser (connected to the setup shown in Figure 3.4a, instead of the pulsed 1550 nm laser). 'Writing' (from state '0' to '1') was achieved by a transient 20 keV electron beam excitation, and readout was performed via CL measurements using a low-power 2 keV electron beam.

The gallium nanoparticles were initially stabilized in state '0' at a temperature of 100 K, below their solidification temperature (see Figure 3.8d). An initial readout hyperspectral imaging scan of twelve individual points in a 4×3 array (within a 4×3.2 μm^2 area) was performed using a 2 keV, 350 pA electron beam with a spot diameter of ~500 nm, which encompassed less than 50 particles at each point (Figure 3.8a). At each point, the CL spectrum was recorded (Figure 3.8b) and the emission intensity was integrated between 450 and 600 nm. These values are presented as a grey-scale intensity map in Figure 3.8c[i]. The CW 1550 nm laser was then switched on to generate a local increase in the temperature of the nanoparticles, bringing them to a point (still in state '0') within the hysteresis loop where excitation-induced switching is possible.

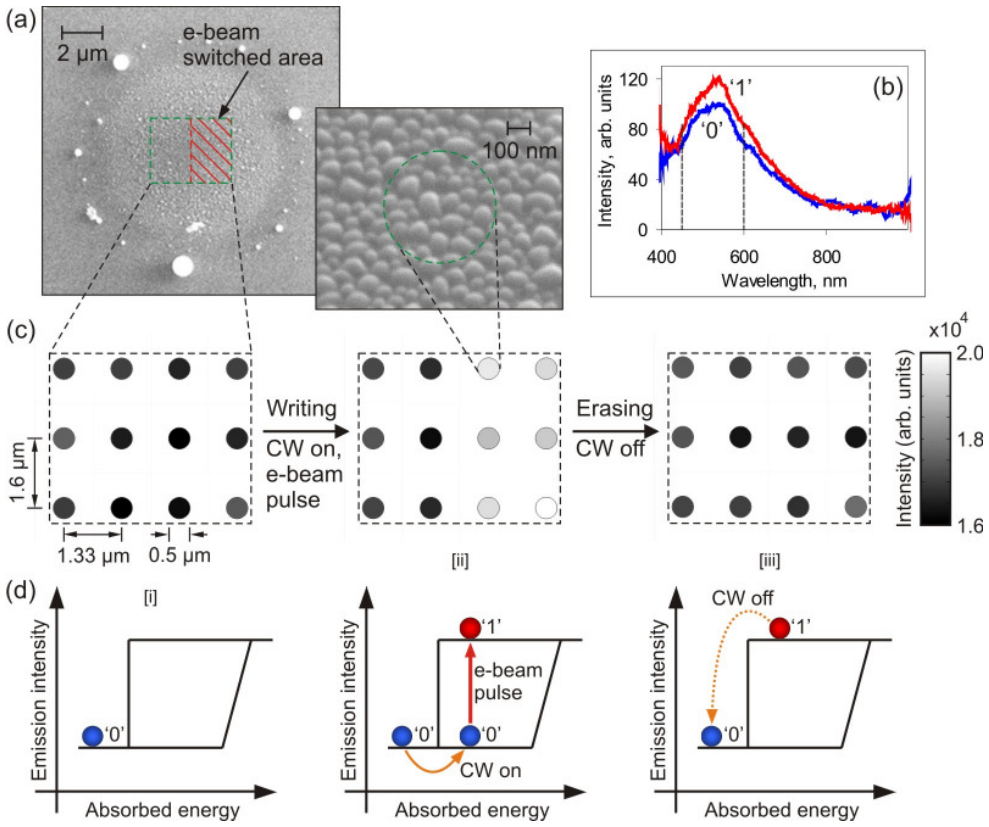

Figure 3.8. Selective electron beam induced switching and CL readout of two halves of a gallium nanoparticle film. (a) Secondary electron images of a gallium nanoparticle film grown on the core area of a single-mode fibre end face. (b) Typical CL readout spectra from one of the twelve sample points in states '0' and '1', obtained using 2 keV electrons. (c) Readout scans showing integrated CL emission intensity between 450 and 600 nm from twelve points from the area of the nanoparticle film shown in (a) at different stages of the memory cycle: [i] all elements in state '0' at low temperature; [ii] half of the elements switched to state '1' and held there by the presence of CW laser light; [iii] Switched elements restored to '0' state (erased) by switching off the CW laser (allowing the particles to cool). (d) Schematic illustrations of the stages of memory cycle corresponding to (c).

The right-hand half of the test area (encompassing six of the twelve sample points) was exposed to a single 40 ms, 20 keV electron beam scan with a current of 30 nA (a fluence of 210 fJ/nm^2). A second CL readout scan of the same twelve points, with the low power 2 keV electron beam, revealed an at least 15 % increase in emission intensity from the six points exposed to the higher power

beam, and no change in emission from the six unexposed points on the left (Figure 3.8c[ii]), thereby demonstrating the selective switching of the right-hand memory bits from state '0' to state '1' by the higher power electron beam. Switching off the CW laser restores the switched memory elements to the '0' state; a fact confirmed by a third CL readout scan illustrating the recovery of their emission levels to pre-switching levels (Figure 3.8c[iii]).

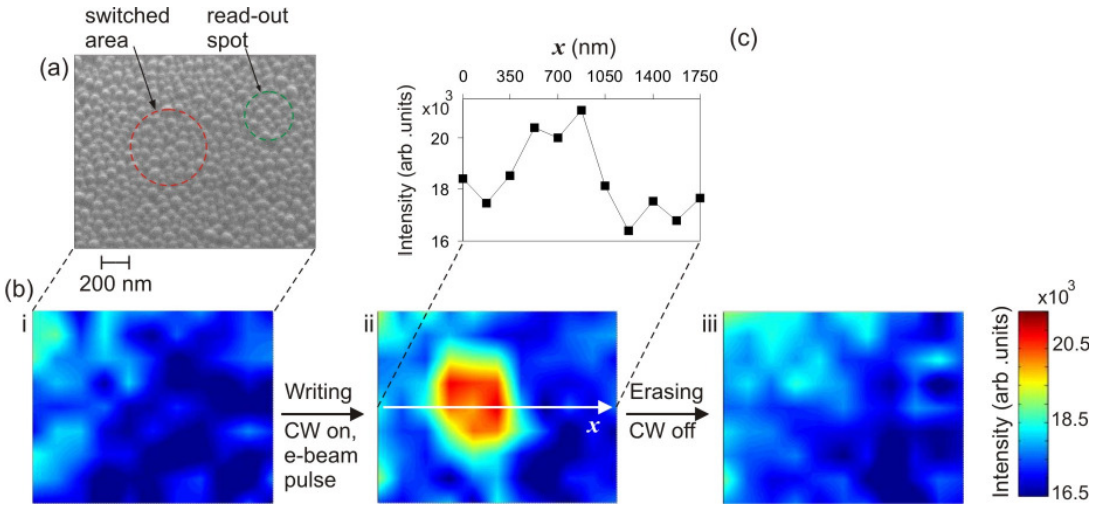

Figure 3.9. Selective electron beam induced switching and CL readout of a single memory element within a gallium nanoparticle film. (a) Secondary electron image of the 1750×1400 nm^2 area of the nanoparticle film. (b) Readout scans showing integrated CL emission intensity between 450 and 600 nm, from the sample area shown in (a), at different stages of the memory cycle. (c) Emission intensity along x axes.

For the purpose of demonstrating selective addressing and readout of a smaller group of nanoparticles, a film of low dispersion gallium nanoparticles with a mean diameter of 53 nm was prepared (Figure 3.9a, the sample shown on Figure 2.16b). The gallium nanoparticles were initially stabilized in state '0' at a temperature of 120 K, that is below their solidification temperature. The procedure of memory functionality demonstration was similar to the one described above. The readout hyperspectral imaging scans over a 1750×1400 nm^2 area of the film (11×9 sampling points) were performed at the same stages of memory cycle as above. The reading electron beam was 2 keV, 390 pA, with a

spot diameter of ~350 nm, which encompassed less than 20 particles (see Figure 3.9a). The emission maps produced by integrating CL emission in the 450–600 nm range are shown in Figures 3.9b[i-iii]. While the holding power from the CW 1550 nm laser was 3 mW, the same as above, 'writing' was performed by exposing a single spot with diameter of ~550 nm (encompassing less then 50 particles) to single 5 μs 20 keV electron beam pulse with a current of 130 nA (a fluence of ≥ 60 fJ/nm^2). The following CL readout scan revealed an increase of at least 15 % in the 450-600 nm emission from the exposed spot, and no change in the emission from the unexposed area (Figure 3.9b[ii]), thereby confirming the selective switching of one individual memory element from state '0' to state '1'. Switching off the CW 1550 nm laser restored the switched memory element to the '0' state (Figure 3.9b[iii]).

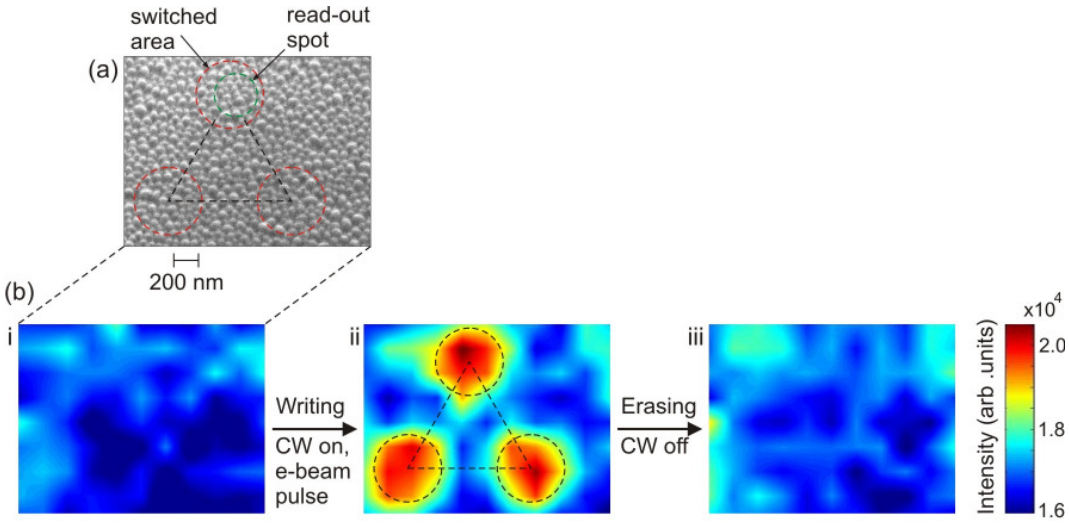

Figure 3.10. Selective electron beam induced switching and CL readout of three memory elements within a gallium nanoparticle film. (a) Secondary electron image of the 2000×1600 nm^2 area of the nanoparticle film. (d) Readout scans showing integrated CL emission intensity between 450 and 600 nm, from the sample area shown in (a), at different stages of the memory cycle.

Finally, the demonstration of writing and erasing of three memory elements was performed with the same nanoparticle film (over the area of 2000×1600 nm^2). Three spots with diameters of ~550 nm (each encompassing

less then 50 particles) with mutual separations of 1 μm (*i.e.* at the corners of an equilateral triangle) were exposed sequentially to single 20 keV electron beam pulses (Figure 3.10). The procedure of the experiment and other experimental parameters were identical to those described in the previous paragraph.

An SEM can be successfully used for the investigation and the demonstration of nanoparticle phase-change memory in laboratory conditions. However, because of its cost and size, commercial write-read data storage drives cannot be based on it. Nevertheless, the technique of electron beam addressing and CL readout of memory state may be applied in commercial devices using the Surface-conduction electron-emitter display (SED) technology. The SED technology for flat panel displays has been in development by Canon and Toshiba since 1986 [42]. In SEDs, a two-dimensional array of electron emitters is situated just opposite a phosphor screen, so that each emitter controls the CL emission from the correspondent pixel. The SED technology represents the solution of the major problems of CRT (Cathode ray tube) display: *i.e.* raster scanning and large depth and weight. It is possible that the SED technology will be used in future write-read data storage drives as well.

3.6 Enhancement of logic state contrast

Experimental results and calculations, described in the previous two Sections, show a difference of less than 20 % between solid and liquid state electron-induced light emission of gallium nanoparticles. For practical data storage applications, to facilitate error-free readout, it would be beneficial to maximize the contrast between phase (logic) states.

To this end, metallic nanoshells (surrounding a dielectric or semiconductor core) may be considered. These structures are known for the exceptional tunability of their plasmon resonances, which is achieved by varying the core and shell diameters or by changing the surrounding medium [43]. The high sensitivity of the nanoshell resonances to these parameters results from the coupling between surface plasmons on the inner and outer metallic surfaces [44]. It can thus be hypothesized that the electron beam induced emission contrast for phase-change

memory readout might be enhanced through the use of nanoshells in place of homogenous particles.

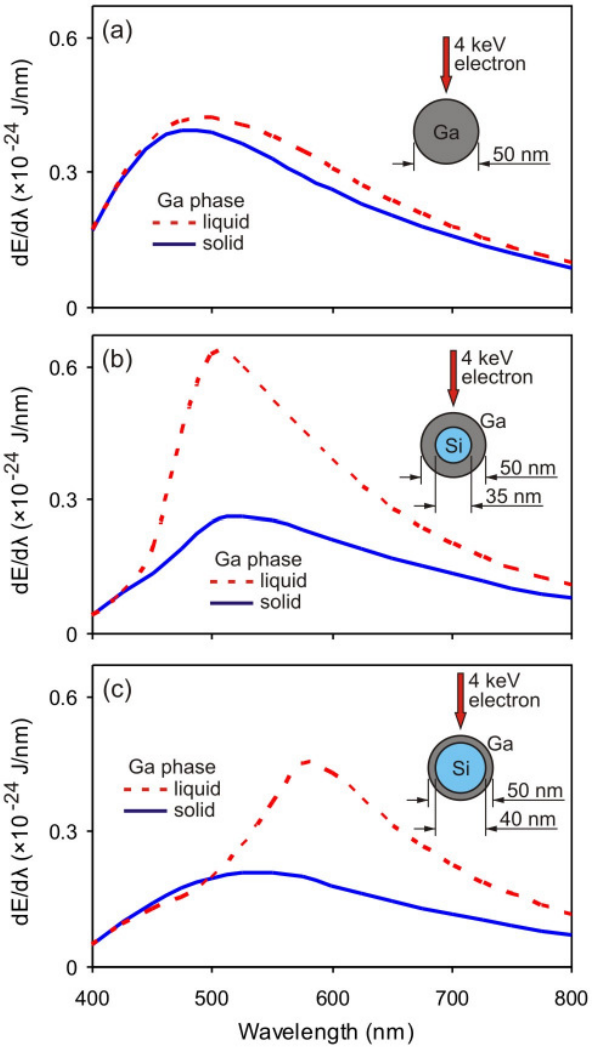

Figure 3.11. Calculated total CL emission (in all directions) from a free-standing spherical (solid/liquid) pure gallium particle (a) and from silicon core (solid/liquid) gallium coated nanoshells (b, c) in vacuum, induced by one 4 keV electron for the trajectory through the centre of the particle.

To test this idea, calculations of electron beam induced emission were performed for 50 nm pure gallium nanoparticles and gallium nanoshells of the same outer diameter using the boundary element method [40] (Subsection 1.6.3).

Figure 3.11 shows emission spectra for 4 keV electrons passing through the centres of free-standing solid and liquid pure gallium nanoparticles and nanoshells of different thicknesses on a silicon core. The calculations show that the difference between solid and liquid phase light emission from a 50 nm diameter pure gallium nanoparticle is less then 20 %. However, a gallium nanoshell with an outer diameter of 50 nm can exhibit much higher contrast between phases (more than 100 % for certain core diameters).

3.7 Conclusions

Gallium nanoparticle phase-change memory, where information is recorded into phase state of individual particles (bits), provides an intriguing possibility to achieve small element size (about tens of nanometers) and small writing energy (femtojoule per particle range). An electron beam, with an intrinsic ability to focus in the nanoscale range, is a suitable tool to study phase-change memory functionality in gallium nanoparticles: Switching between phase states (*i.e.* 'writing') can be achieved with a higher energy electron beam while 'readout' is performed by monitoring CL response that is induced by a lower energy electron beam, thus providing a new conceptual basis for the development of high-density data storage.

As it is a simpler case to contemplate, the electron beam induced light emission from bulk gallium in its α-solid and liquid phases has been studied first. Here, for 40 keV electrons, an increase in emission intensity of up to 50 % is observed when the metal undergoes a solid-to-liquid phase transition. This result is found to be consistent with calculations of transition radiation for the two phases.

It has been shown experimentally that the phase (logic) state of gallium nanoparticle phase-change memory elements can be determined via measurements of their CL emission. Changes of up to 20 % in visible emission intensity are observed following low-fluence optical or electron beam induced phase switching of a monolayer of 60 nm particles. Calculation of electron beam induced light emission, performed for homogeneous gallium films and single gallium

nanoparticles, qualitatively reproduced the general characteristics observed in the experiment: higher emission from liquid gallium phase and emission peak.

'Volatile' mode, selectively electron beam addressed, erasable memory functionality has been demonstrated in a gallium nanoparticle film as well. Several individual bits of information (each element comprised less than fifty nanoparticles) were recorded in the structural phase of the gallium nanoparticles using a 20 keV electron beam pulse and readout via measurements of their CL emission in response to a 2 keV electron beam. This proof of principle investigation demonstrates that electron beam addressed nanoparticles may offer a route toward the development of high-density nonvolatile phase-change memories.

Finally, the possibility of enhancing emission contrast for CL readout of phase-change memory by employing nanoshells, as opposed to homogenous nanoparticles, has been analyzed numerically. Calculations suggest that the electron beam induced emission intensity for silicon/gallium core/shell structures may increase by as much as 100 %, following a solid-to-liquid transition in the gallium shell, as compared to a less than 20 % change observed experimentally and confirmed theoretically for pure gallium particles.

3.8 References

[1] R. Kirchain and L. Kimerling, *"A roadmap for nanophotonics,"* Nat. Photonics **1**, 303 (2007).

[2] A. Jenkins, *"The road to nanophotonics,"* Nat. Photonics **2**, 258 (2008).

[3] R. Zia, J. A. Schuller, A. Chandran, and M. L. Brongersma, *"Plasmonics: the next chip-scale technology,"* Materials Today **9**, 20 (2006).

[4] E. Ozbay, *"Plasmonics: Merging photonics and electronics at nanoscale dimensions,"* Science **311**, 189 (2006).

[5] D. Pacifici, H. J. Lezec, and H. Atwater *"All-optical modulation by plasmonic excitation of CdSe quantum dots,"* Nat. Photonics **1**, 402 (2007).

[6] M.-S. Hu, H.-L. Chen, C.-H. Shen, L.-S. Hong, B.-R. Huang, K.-H. Chen, and L.-C. Chen, *"Photosensitive gold-nanoparticle-embedded dielectric nanowires,"* Nat. Mater. **5**, 102 (2006).

[7] P. Ahonen, D. J. Schiffrin, J. Paprotny, and K. Kontturi, *"Optical switching of coupled plasmons of Ag-nanoparticles by photoisomerisation of an azobenzene ligand,"* Phys. Chem. Chem. Phys. **9**, 651 (2007).

[8] Y. Leroux, E. Eang, C. Fave, G. Trippe, and J. C. Lacroix, *"Conducting polymer/gold nanoparticle hybrid materials: A step toward electroactive plasmonic devices,"* Electrochemistry Communication **9**, 1258 (2007).

[9] M. Wuttig, *"Towards a universal memory?"* Nat. Mater. **4**, 265 (2005).

[10] N. I. Zheludev, *"All change, please,"* Nat. Photonics **1**, 551 (2007).

[11] A. V. Krasavin and N. I. Zheludev, *"Active plasmonics: Controlling signals in Au/Ga waveguide using nanoscale structural transformations,"* Appl. Phys. Lett. **84**, 1416 (2004).

[12] M. Rini, A. Cavalleri, R. W. Schoenlein, R. López, L. C. Feldman, R. F. Haglund, L. A. Boatner, and T. E. Haynes, *"Photoinduced phase transition in VO_2 nanocrystals: ultrafast control of surface-plasmon resonance,"* Opt. Lett. **30**, 558 (2005).

[13] K. F. MacDonald, V. A. Fedotov, and N. I. Zheludev, *"Optical nonlinearity resulting from a light-induced structural transition in gallium nanoparticles,"* Appl. Phys. Lett. **82**, 1087 (2003).

[14] M. Bernasconi, G. L. Chiarotti, and E. Tosatti, *"Ab initio calculations of structural and electronic properties of gallium solid-state phases,"* Phys. Rev. B **52**, 9988 (1995).

[15] N. R. Comins, *"The optical properties of liquid metals,"* Phil. Mag. **25**, 817 (1972).

[16] A. Di Cicco, *"Phase transitions in confined gallium droplets,"* Phys. Rev. Lett. **81**, 2942 (1998).

[17] A. Defrain *"Etats metastables du gallium, surfusion et polymorphisme,"* J. Chim. Phys. PCB **74**, 851 (1977).

[18] R. S. Berry and B. M. Smirnov, *"Phase stability of solid clusters,"* J. Chem. Phys. **113**, 728 (2000).

[19] M. Wautelet, *"Phase stability of electronically excited Si nanoparticles,"* J. Phys.: Condens. Matter **16**, L163 (2004).

[20] A. S. Shirinyan and M. Wautelet, *"Phase separation in nanoparticles,"* Nanotechnology **15**, 1720 (2004).

[21] B. F. Soares, M. V. Bashevoy, F. Jonsson, K. F. MacDonald, and N. I. Zheludev, *"Polymorphic nanoparticles as all-optical memory elements,"* Opt. Express **14,** 10652 (2006).

[22] M. Wautelet, *"Estimation of the variation of the melting temperature with the size of small particles, on the basis of a surface-phonon instability model,"* J. Phys. D **24**, 343 (1991).

[23] B. F. Soares, F. Jonsson, and N. I. Zheludev, *"All-optical phase-change memory in a single gallium nanoparticle,"* Phys. Rev. Lett. **98**, 153905 (2007).

[24] P. D. Townsend, M. Maghrabi, and B. Yang, *"Luminescence detection of phase transitions,"* Nucl. Instrum. Methods Phys. Res., Sect. B **191**, 767 (2002).

[25] Y. C. Chang, A. L. Cai, A. L. Johnson, J. F. Muth, R. M. Kolbas, Z. J. Reitmeier, S. Einfeldt, and R. F. Davis, *"Luminescence detection of phase transitions,"* Appl. Phys. Lett. **80**, 2675 (2002).

[26] K. C. Hui, C. W. Lai, and H. C. Ong, *"Electron-beam-induced optical memory effect in metallized ZnO thin films for the application of optical storage,"* Thin Solid Films **483**, 222 (2005).

[27] A. I. Denisyuk, F. Jonsson, K. F. MacDonald, N. I. Zheludev, and F. J. García de Abajo,, *"Luminescence readout of nanoparticle phase state,"* Appl. Phys. Lett. **92**, 093112 (2008).

[28] A. I. Denisyuk, K. F. MacDonald, N. I. Zheludev, and F. J. García de Abajo, *"Towards femtojoule nanoparticle phase-change memory,"* Jpn. J. Appl. Phys. **48**, 03A065 (2009).

[29] N. Yamamoto, K. Araya, A. Toda, and H. Sugiyama, *"Light emission from surfaces, thin films and particles induced by high-energy electron beam,"* Surf. Interface Anal. **31**, 79 (2001).

[30] O. Hunderi and R. Ryberg, *"Band structure and optical properties of gallium,"* J. Phys. F **4**, 2084 (1974).

[31] V. L. Ginzburg, *"Transition radiation and transition scattering,"* Phys. Scr. **T2A** 182 (1982).

[32] R. Kofman, P. Cheyssac, and J. Richard, *"Optical properties of Ga monocrystal in the 0.3–5-eV range,"* Phys. Rev. B **16**, 5216 (1977).

[33] R. S. Teshev and A. A. Shebzukhov, *"Electronic characteristics and dispersion of optical constants of liquid gallium in the 0.4–2.5-μm spectral region,"* Opt. Spectrosc. **65**, 693 (1988).

[34] K. Kanaya and S. Okayama, *"Penetration and energy-loss theory of electrons in solid targets,"* J. Phys. D. **5**, 43 (1972).

[35] K. F. MacDonald, V. A. Fedotov, S. Pochon, K. J. Ross, G. C. Stevens, N. I. Zheludev, W. S. Brocklesby, and V. I. Emel'yanov, *"Optical control of gallium nanoparticle growth,"* Appl. Phys. Lett. **80,** 1643 (2002).

[36] B. F. Soares, K. F. MacDonald, and N. I. Zheludev, *"Resetting single nanoparticle structural phase with nanosecond pulses,"* Appl. Phys. Lett. **91**, 043115 (2007).

[37] O. Hunderi, *"The band structure in monoclinic β-Ga,"* J. Phys. F **5**, 883 (1975).

[38] V. E. Pafomov and I. M. Frank, *"Transition radiation at two parallel interfaces,"* Sov. J. Nucl. Phys. **5**, 448 (1967).

[39] O. Hunderi and R. Ryberg, *"Amorphous gallium – a free electron metal,"* J. Phys. F **4**, 2096 (1974).

[40] F. J. García de Abajo and A. Howie, *"Retarded field calculation of electron energy loss in inhomogeneous dielectrics,"* Phys. Rev. B **65**, 115418 (2002).

[41] V. A. Fedotov, V. I. Emel'yanov, K. F. MacDonald, and N. I. Zheludev, *"Optical properties of closely packed nanoparticle films: spheroids and nanoshells,"* J. Opt. A **6**, 155 (2004).

[42] http://www.canon.com/technology/canon_tech/explanation/sed.html

[43] R. D. Averitt, D. Sarkar, and H. J. Halas, *"Plasmon resonance shifts of Au-coated Au_2S nanoshells: Insight into multicomponent nanoparticle growth,"* Phys. Rev. Lett. **78**, 4217 (1997).

[44] E. Prodan and P. Nordlander, *"Structural tunability of the plasmon resonances in metallic nanoshells,"* Nano Lett. **3**, 543 (2003).

Chapter 4
Transmitting optical antenna based on gold nanorods

4.1 Synopsis

Functionality of transmitting optical antennae based on pairs of coupled gold nanorods has been demonstrated by means of a scanning electron microscopy – cathodoluminescence (SEM–CL) technique.

An introduction to light emission sources with an electron beam pump and a review of investigations of localized surface plasmons in metallic nanostructures using spatially resolved CL, are given in Section 4.2. The same section describes the idea of making optical antennae based on metallic nanorods and reviews experimental studies performed so far for such nanostructures. Investigation of the plasmonic properties of isolated and coupled gold nanorods is described in Section 4.3. It has been demonstrated that pairs of coupled gold nanorods can act as transmitting optical antennae, which effectively convert the energy from a nanoscale source of excitation created by a focused electron beam into far-field radiation detected by means of CL. Enhanced CL emission is observed for electron beam illuminating points in the vicinity of the junction between coupled nanorods.

4.2 Introduction

An example of a classical light source, which uses high-energy electrons to produce radiation, is a free-electron laser [1]. The origin of light emission in such a system is bremsstrahlung radiation produced by decelerated electrons. However, these systems are large; in contrast, miniature free-electron light sources and lasers could be designed by employing the Smith-Purcell effect.* This idea is being studied experimentally and theoretically nowadays for the cases of the electron beam passing near various periodic nanostructures, such as grating horns [3] and strings of nanoparticles [4].

Metallic nanostructures can also exhibit strong electron-beam-induced light emission, which occurs via a plasmon-mediated mechanism. Investigation of metallic nanostructures by means of a spatially resolved CL mapping, performed with a focused electron beam, was first conducted by Yamamoto *et al.* [5]. It was demonstrated that CL images reveal surface plasmon modes in spherical silver nanoparticles. Later, this technique was applied for exploring localized surface plasmons in silver nanostructures (such as touching spheres, whiskers, stripes [6], nanorods [7]) and gold nanostructures (such as nano-ridges [8], nanorods [9], annular resonators [10], and gratings [11]).

Structures comprising arrangements of metallic nanorods have recently attracted considerable attention as potential optical antennae. Such antennae would be able to efficiently couple the energy of free-space radiation to a confined region of subwavelength size, or to modify the amount of energy emitted and the direction of far-field emission from nanoscale sources [12, 13]. These components are expected to find applications in field-enhanced single-molecule spectroscopy [14] and as elements of future nanophotonic circuits [13].

---

* Smith-Purcell effect [2] is the radiation produced by a high-energy electron passing parallel to the surface of a grating (any medium with periodically modulated dielectric constants in a general case). This radiation can be considered as a special form of Cherenkov radiation where the phase velocity of the light is altered by the periodic grating.

An optical antenna can be designed from a pair of closely-spaced nanorods, whose surface plasmons are coupled. Therefore, such nanorod pairs are commonly called coupled nanorods [15]. Experimental studies of nanorod and nano-antenna structures have largely been conducted using a combination of optical far-field and near-field scanning probe microscopy techniques. The former enables the investigation and comparison of plasmonic resonances of nanostructures [16], while the latter facilitates the interrogation of the enhanced fields in the gaps between antenna elements [17]. The possibility for tuning the scattering response of optical antennae has been also analyzed numerically [18].

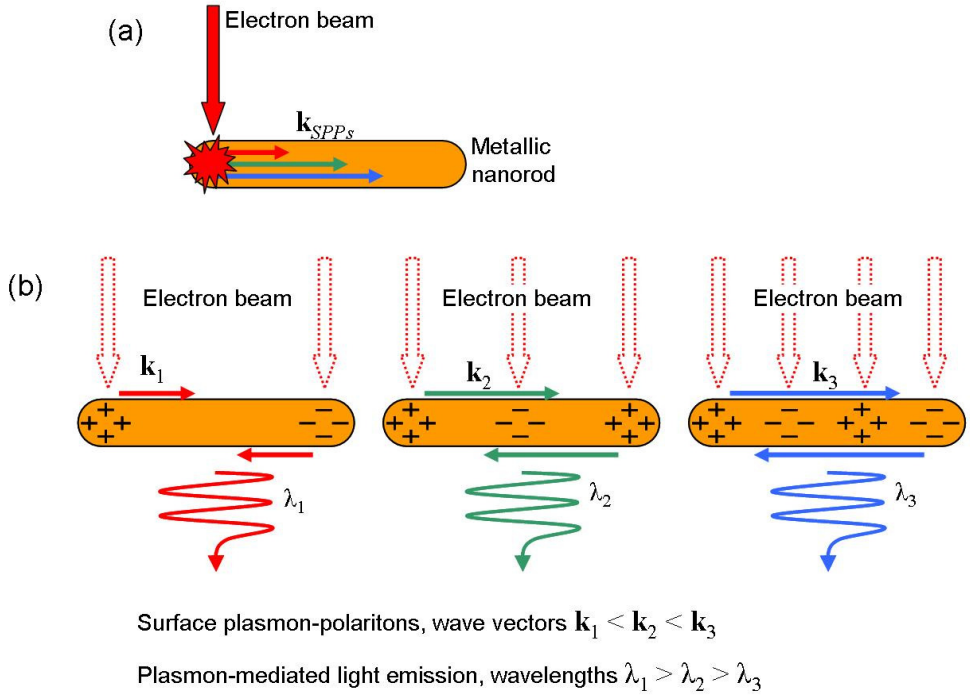

Figure 4.1. Illustration of standing wave plasmonic modes in metallic nanorods revealed via the SEM-CL technique. (a) A focused electron beam illuminating a nanorod creates a broadband SPP source. (b) Interference between SPPs propagating along the rod and reflected at its ends produces standing plasmon waves, which scatter to free-space light. Light emission maxima occur when the incident electron beam illuminates antinode positions of the standing plasmon waves.

However, it has recently been shown that electron energy loss and CL spectroscopy performed in electron microscopes provides an alternative method of mapping the plasmonic modes of metallic nanorods [6–8, 19, 20]. A focused electron beam, such as those found in transmission and scanning electron microscopes, impacting on a metal surface acts as a nanoscale, mobile, broadband surface plasmon polariton (SPP) source [21, 22]. These plasmons scatter to free-space light that can be collected in the far field by CL analysis. In the case of single gold and silver nanorods, such techniques reveal plasmonic standing wave modes resulting from interference between the excited SPPs and back-scattered SPPs reflected from the ends of the rod [6, 8] (see Figure 4.1). Plasmonic modes in coupled gold nanorods were also investigated by means of electron energy loss spectroscopy, which revealed symmetric and asymmetric coupled modes in such nanostructures [20].

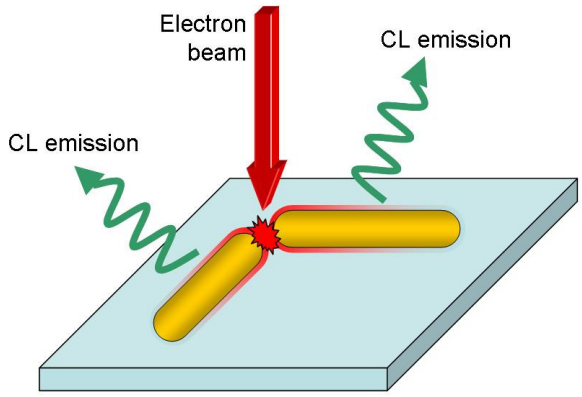

Figure 4.2. Schematic of a transmitting optical antenna with an electron beam pump. A pair of coupled gold nanorods efficiently converts the energy from a nanoscale excitation created by a focused electron beam into far-field CL emission. Enhanced emission is observed for electron beam injection points in the vicinity of the rod's junction.

Pairs of coupled gold nanorods have recently been studied by means of SEM–CL analysis [23]. It has been shown that such complex metallic nanostructures can effectively convert the energy from a nanoscale source of excitation (created by a focused electron beam) in far-field radiation (detected by means of CL). Enhanced CL emission is observed for electron beam injection

points in the vicinity of the rod's junction. The observed effect demonstrates the ability of coupled metallic nanorods to act as a transmitting optical antenna with an electron beam pump (see Figure 4.2). The following section details the functionality of a transmitting optical antenna based on coupled gold nanorods. Plasmonic characteristics of coupled gold nanorods are given in comparison to the ones of isolated gold nanorods.

4.3 Transmitting optical antenna with an electron beam pump

Gold nanorods were synthesized by the seed-mediated growth method and then dispersed on a silicon substrate[*]. Imaging and CL analyses were performed in a scanning electron microscope (SEM) equipped with a spectroscopic CL system (setup as described in Section 2.3). By scanning a sample point by point with the focused 40 keV (4.5 nA) electron beam and synchronously recording the light emission spectrum generated at every pixel, 'hyperspectral' images (HSI) of the sample were obtained. The HSI 'data cube' has two spatial axes, defining the co-ordinates of electron beam injection points in the sample plane, and a spectral axis. It can be analyzed to yield, for example, point spectra and/or single-

[*] The sample (gold nanorods dispersed on a silicon substrate) was prepared by Dr. M. D. Arnold and Prof. M. J. Ford from the Institute for Nanoscale Technology, University of Technology, Australia.

Seed-mediated growth of gold nanorods [24–26] is performed in a chemical solution consisting of water, cetyl-trimethyl ammonium bromide (CTAB), $HAuCl_4$, $AgNO_3$, ascorbic acid and gold nanoparticle seeds (with a mean diameter between 3 and 4 nm). In this solution, seeds become the template for gold atoms (from $HAuCl_4$) to join. However, CTAB molecules cover certain crystal facets of gold nanoparticles, which prevent these facets from accepting arriving gold atoms. This enables one-dimensional growth of gold nanoparticles in the shape of rods. Upon increasing CTAB concentration, rod length increases while the width of the rods decreases. Silver ions (from $AgNO_3$) play the role of a complexing agent for lessening repulsion between neighboring CTAB molecules on the gold surface. Ascorbic acid is a reducing agent, which donates electrons to other elements and compounds.

wavelength spatial intensity maps [11] (the HSI technique is detailed in Subsection 2.3.2).

The recorded spectral range was limited to 450–850 nm where the signal-to-noise ratio was sufficiently high. To obtain light emission images, the electron beam scanned 21 columns on 17 rows (CL emission images in this chapter typically show less than the full 17 rows to emphasise the region of interest) with the emitted light being simultaneously measured. The silicon CL background signal was subtracted from the data and CL emission spectra were normalized.

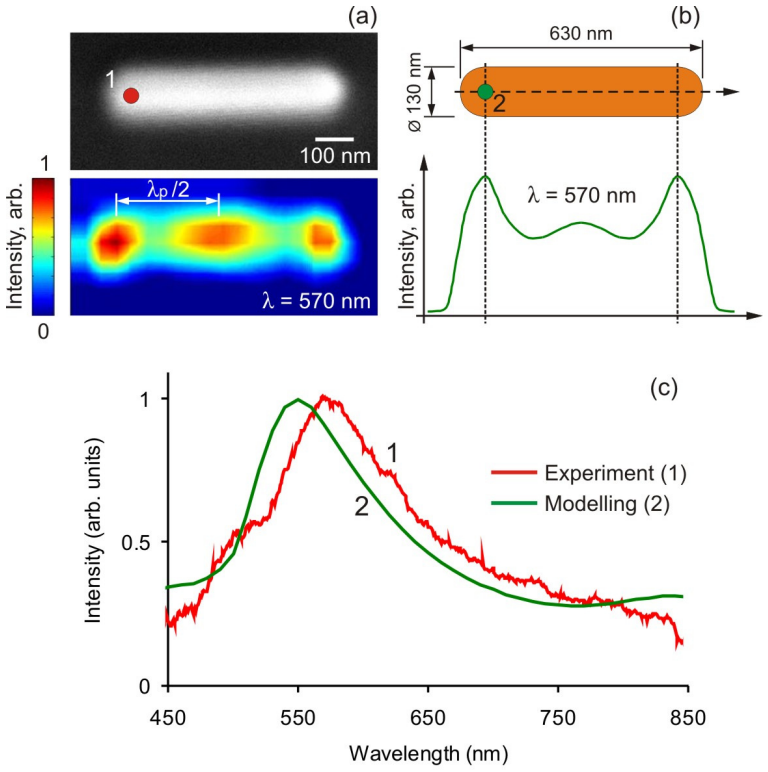

Figure 4.3. (a) Electron image and CL emission map taken at a wavelength of 570 nm for an isolated gold nanorod. (b) Drawing of the isolated gold nanorod used in the modelling; and, below, the modelled CL emission intensity at a wavelength of 570 nm for electron beam scanning along the rod's axis of rotation. (c) Experimental and modelled CL emission spectra taken for electron beam injection points, marked on (a) and (b) with numbers and colours.

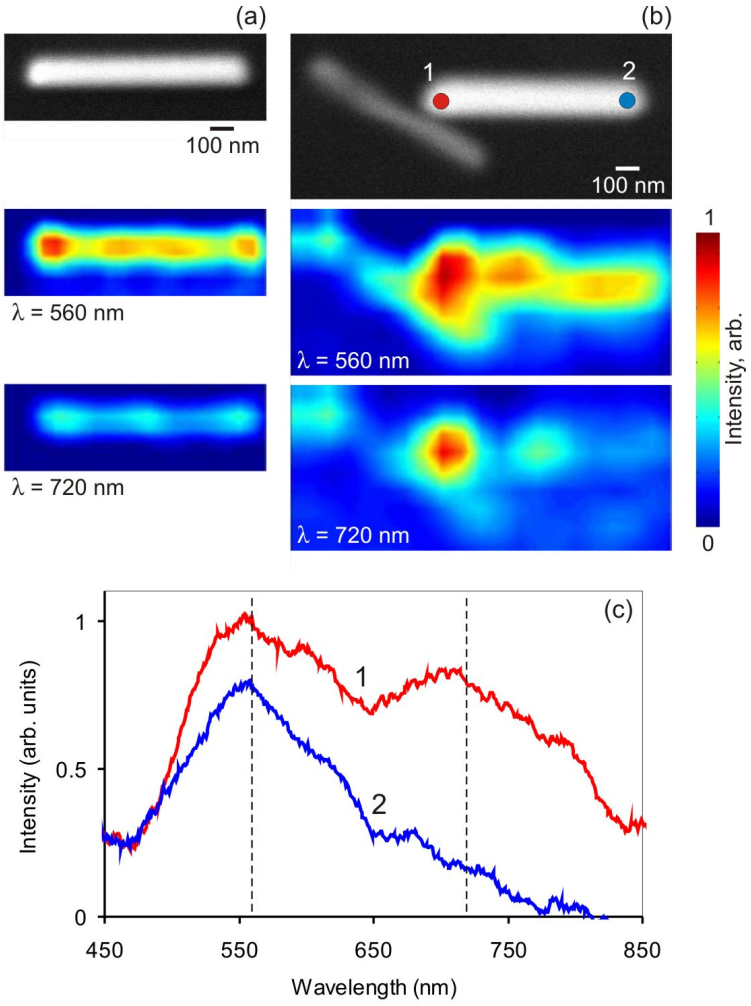

Figure 4.4. Electron images of an isolated gold nanorod (a) and a pair of coupled gold nanorods (b), note that the bigger rod in the pair has a similar size to the isolated rod in (a). Below, CL maps taken at wavelengths of 560 and 720 nm are shown for both nanostructures. (c) CL spectra taken for electron beam injection points, marked on (b) with numbers and colours.

HSI of single gold nanorods (Figures 4.3a and 4.4a) reveals the kind of plasmonic standing wave modes that were recently reported by Vesseur *et al.* [8]. For instance, the emission spectrum from the rod (shown in Figure 4.3a) for an electron beam injection point at one end of the rod has a characteristic single peak at 570 nm (Figure 4.3c). The emission map of the rod taken at this wavelength shows the pattern of three maxima. The distance between two neighboring

maxima corresponds to $\lambda_p/2$, where λ_p is the SPP wavelength [6, 8]. Thus the SPP in the gold nanorod (in Figure 4.3a) has a wavelength of $\lambda_p = 530$ nm (or a wavenumber $k \approx 12$ μm^{-1}) and an energy of 2.2 eV (corresponding to 570 nm wavelength of light emission).

The experimentally observed plasmonic features of the single gold nanorod (in Figure 4.3a) agrees well with modelled CL emission from that rod (diameter/length of 130/630 nm, with hemispherical ends) performed using the boundary element method [27] (detailed in Subsection 1.6.3). Modelled results illustrated the CL emission pattern of three maxima along the rod's axis of rotation at a wavelength of 570 nm (Figure 4.3b) and a CL spectrum with a single emission peak for the electron beam illuminating a point at one end of the rod (Figure 4.3c).

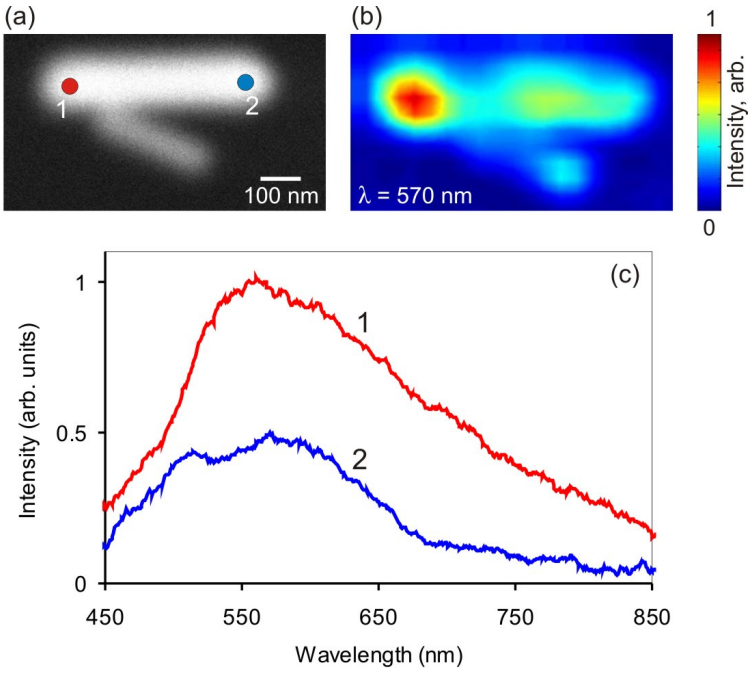

Figure 4.5. (a) Electron image and (b) CL emission map taken at a wavelength of 570 nm for a pair of coupled gold nanorods. (c) CL emission spectra taken for electron beam injection points, marked on (a) with numbers and colours.

In the case of pairs of coupled gold nanorods (Figures 4.4b; 4.5a,b; and 4.6a,b) light emission is found to be substantially stronger for electron beam injection points around the rods' junction than for any other point on the structure. The case of the rod pair, shown in Figure 4.4b, can be compared with the isolated gold nanorod (Figure 4.4a), which has a similar size to the bigger rod in the pair. The CL emission spectrum for the point of junction of the rod pair has two maxima, one at 560 nm and the other at 720 nm. CL emission maps of the isolated and the coupled nanorods (Figures 4.4a,b) taken at these wavelengths illustrate that light emission for the junction area of the rod pair is especially strong at 720 nm. Emission intensity at 720 nm for this point is at least twice higher than for any other point of the rod pair and any point of the isolated rod. CL emission maps of the bigger rod in the pair (apart from the points near to the junction area) reveal a plasmon mode structure similar to the one of the isolated nanorod.

The behavior of coupled metallic nanorods as transmitting optical antennae can be explained in terms of the electromagnetic 'local density of states'. In general, the physical quantity of density of states (DOS) [28, 29] describes the number of states per unit energy range that are available to be occupied. In solid state physics, electronic DOS is defined as the number of electron states at each energy level (or within a given energy range). The electronic DOS determines, for instance, transition rates between valence and conduction bands in semiconducting materials. The local density of states (LDOS) is the spatially resolved DOS. For example, the electronic LDOS corresponds to the density of the probability of finding an electron of energy E at a given point $\mathbf{r}$. In optics, electromagnetic DOS is defined as the number of photons (or plasmons, for instance) per unit frequency. The electromagnetic LDOS is related to the electric field intensity at a given position $\mathbf{r}$ and at a given frequency ω [30]. Therefore, the electromagnetic LDOS reflects the electromagnetic field enhancement in the system, as demonstrated for the cases of metallic nanostructures in [31].

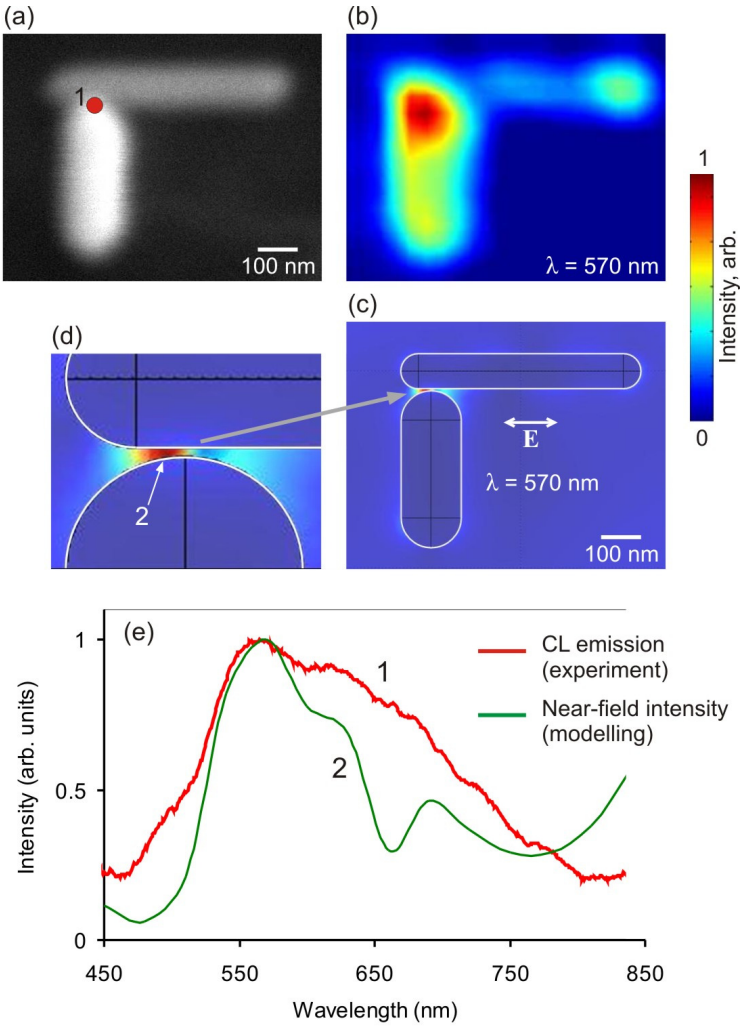

Figure 4.6. (a) Electron image and (b) CL map taken at a wavelength of 570 nm for a pair of coupled gold nanorods. (c) Modelled near-field map at a wavelength of 570 nm for a pair of gold nanorods illuminated with polarized electromagnetic radiation (polarization plane is shown with the arrow); the pair of rods has the same size and geometry as the rod pair shown in (a). Near-field intensity enhancement is found in the gap between the rods, as shown on the magnified image in (d). (e) Experimental CL emission spectrum taken for an electron beam injection into the area of the rods' junction marked on (a) as the red circle "1"; modelled spectrum of the near-field intensity in the gap between the rods marked on (d) as "2".

It has been established that a pair of coupled metallic nanorods, when illuminated with light, exhibits a near-field intensity enhancement in the gap between the rods at the resonance frequency [15]; this suggests that the

electromagnetic LDOS in that region and at that frequency should be high. Recently, it has also been demonstrated that the electromagnetic LDOS of a sample can be probed with an electron beam via electron energy loss spectroscopy [32]. The close link between electron energy loss and light emission in metallic nanostructures suggests that their electromagnetic LDOS can also be probed by CL spectroscopy. In the current case of coupled nanorod pairs, the enhanced CL emission was observed when an electron beam targeted the junction region between coupled rods, which is a reflection of the high LDOS in those areas. High electromagnetic LDOS gives rise to enhanced electron energy loss leading to increased surface plasmon generation and therefore light emission. In contrast, when an electron beam targets the distal end of a coupled rod, the LDOS it encounters is lower (essentially the same as that which it would find in an isolated rod), therefore the light emission is lower.

The previous reasoning suggests that near-field and CL maps of metallic nanostructures should be similar. To test this hypothesis, a near-field intensity map (Figure 4.6c) and spectrum (Figure 4.6e), for a pair of coupled gold nanorods illuminated with polarized electromagnetic radiation, were modelled numerically[*]. The pair of rods had the same sizes and geometry as the rod pair in the experiment (Figure 4.6a). The modelling revealed a near-field intensity enhancement at a wavelength of 570 nm in the gap between the rods (Figures 4.6d,e). This coincides well with the experimentally observed enhancement of CL emission at a wavelength of 570 nm for electron beam injection at the rods' junction, as shown in Figure 4.6b. This result confirms the expected reciprocity between 'transmitting' and 'receiving' operating modes of optical antennae, equivalent to the well known behavior of radio wave antennae.

[*] Modelling of the near-field intensity for the coupled gold rod pair was performed by G. Adamo using the finite element method in COMSOL Multiphysics [33].

4.4 Conclusions

Nanoscale resolution CL has been employed to investigate plasmonic characteristics of single and coupled gold nanorods. It has been demonstrated that electron-beam-excited pairs of coupled gold nanorods can act as transmitting optical antennae; *i.e.* they can efficiently convert the energy from a nanoscale source of excitation (created by a focused 40 keV electron beam) into far-field visible radiation (detected by means of CL). Enhanced CL emission was observed for electron beam injection points in the vicinity of the junction between coupled rods, which can be explained by the increased local density of electromagnetic states in such areas. The modelled near-field map, for a pair of coupled nanorods illuminated with light, illustrated near-field intensity enhancement in the gap between the nanorods.

4.5 References

[1] S. Khan, *"Free-electron lasers,"* J. Mod. Opt. **55**, 3469 (2008).

[2] S. J. Smith and E. M. Purcell, *"Visible light from localized surface charges moving across a grating,"* Phys. Rev. **92**, 1069 (1953).

[3] A. Bakhtyari and J. H. Brownell, *"Horn resonator boosts miniature free-electron laser power,"* Appl. Phys. Lett. **82**, 3150 (2003).

[4] F. J. García de Abajo, *"Smith-Purcell radiation emission in aligned nanoparticles,"* Phys. Rev. E **61**, 5743 (2000).

[5] N. Yamamoto, K. Araya, F. J. García de Abajo, *"Photon emission from silver particles induced by a high-energy electron beam,"* Phys. Rev. B **64**, 205419 (2001).

[6] N. Yamamoto, M. Nakano, and T. Suzuki, *"Light emission by surface plasmons on nanostructures of metal surfaces induced by high-energy electron beams,"* Surf. Interface Anal. **38**, 17251730 (2006).

[7] R. Gómez-Medina, N. Yamamoto, M. Nakano, and F. J. García de Abajo, *"Mapping plasmons in nanoantennas via cathodoluminescence,"* New J. Phys. **10**, 105009 (2008).

[8] E. J. R. Vesseur, R. de Waele, M. Kuttge, and A. Polman, *"Direct observation of plasmonic modes in Au nanowires using high-resolution cathodoluminescence spectroscopy,"* Nano Lett. **7**, 2843 (2007).

[9] E. J. R. Vesseur, R. de Waele, H. J. Lezec, H. A. Atwater, F. J. García de Abajo, and A. Polman, *"Surface plasmon polariton modes in a single-crystal Au nanoresonator fabricated using focused-ion-beam milling,"* Appl. Phys. Lett. **92**, 083110 (2008).

[10] C. E. Hofmann, E. J. R. Vesseur, L. A. Sweatlock, H. J. Lezec, F. J. García de Abajo, A. Polman, and H. A. Atwater, *"Plasmonic modes of annular nanoresonators imaged by spectrally resolved cathodoluminescence,"* Nano Lett. **7**, 3612 (2007).

[11] M. V. Bashevoy, F. Jonsson, K. F. MacDonald, Y. Chen, and N. I. Zheludev, *"Hyperspectral imaging of plasmonic nanostructures with nanoscale resolution,"* Opt. Express **15**, 11313 (2007).

[12] J.-J. Greffet, *"Nanoantennas for light emission,"* Science **308**, 1561 (2005).

[13] M. L. Brongersma, *"Engineering optical nanoantennas,"* Nat. Photonics **2**, 270 (2008).

[14] T. H. Taminiau, F. D. Stefani, F. B. Segerink, and N. F. van Hulst, *"Optical antennas direct single-molecule emission,"* Nat. Photonics **2,** 234 (2008).

[15] J. Aiapurua, G. W. Bryant, L. J. Richter, F. J. García de Abajo, B. K. Kelly, and T. Mallouk, *"Optical properties of coupled metallic nanorods for field-enhanced spectroscopy,"* Phys. Rev. B **71**, 235420 (2005).

[16] O. L. Muskens, V. Giannini, J. A. Sánchez-Gil, and J. Gómez Rivas, *"Optical scattering resonances of single and coupled dimer plasmonic nanoantennas,"* Opt. Express **15**, 17736 (2007).

[17] N. Yu, E. Cubukcu, L. Diehl, M. A. Belkin, K. B. Crozier, F. Capasso, D. Bour, S. Corzine, and G. Höfler, *"Plasmonic quantum cascade laser antenna,"* Appl. Phys. Lett. **38**, 17251730 (2006).

[18] A. Alù and N. Engheta, *"Tuning the scattering response of optical nanoantennas with nanocircuit loads,"* Nat. Photonics **2**, 307 (2008).

[19] M. Bosman, V. J. Keast, M. Watanabe, A. I. Maaroof , and M. B. Cortie, *"Mapping surface plasmons at the nanometre scale with an electron beam,"* Nanotechnology **18**, 165505 (2007).

[20] M.-W. Chu, V. Myroshnychenko, C. H. Chen, J.-P. Deng, C.-Y. Mou, and F. J. García de Abajo, *"Probing bright and dark surface-plasmon modes in individual and coupled noble metal nanoparticles using an electron beam,"* Nano Lett. **9**, 399 (2009).

[21] M. V. Bashevoy, F. Jonsson, A. V. Krasavin, N. I. Zheludev, Y. Chen, and M. I. Stockman*, "Generation of traveling surface plasmon waves by free-electron impact,"* Nano Lett. **6**, 1113 (2006).

[22] J. T. van Wijngaarden, E. Verhagen, A. Polman, C. E. Ross, H. J. Lezec, and H. A. Atwater, *"Direct imaging of propagation and damping of near-resonance surface plasmon polaritons using cathodoluminescence spectroscopy,"* Appl. Phys. Lett. **88**, 221111 (2006).

[23] A. I. Denisyuk, G. Adamo, Kevin F. MacDonald, N. I. Zheludev, M. D. Arnold, M. J. Ford and F. J. García de Abajo, *"Transmitting optical nano-antenna,"* Manuscript in preparation.

[24] N. R. Jana, L. Gearheart, and C. J. Murphy, *"Seed-mediated growth approach for shape-controlled synthesis of spheroidal and rod-like gold nanoparticles using a surfactant template,"* Adv. Matter. **13**, 1389 (2001).

[25] T. K. Sau and C. J. Murphy, *"Seeded high yield synthesis of short au nanorods in aqueous solution,"* Langmuir **20**, 6414 (2004).

[26] B. Nikoobakht and M. A. El-Sayed, *"Preparation and growth mechanism of gold nanorods (NRs) using seed-mediated growth method,"* Chem. Mater. **15**, 1957 (2003).

[27] F. J. García de Abajo and A. Howie, *"Retarded field calculation of electron energy loss in inhomogeneous dielectrics,"* Phys. Rev. B **65**, 115418 (2002).

[28] C. Kittel, *"Introduction to solid state physics,"* 7th edition, New-York: Wiley, 1996.

[29] M. Fox, *"Optical properties of solids,"* Oxford: Oxford University Press, 2001.

[30] A. Dereux, C. Girard, and J.-C. Weeber, *"Theoretical principles of near-field microscopies and spectroscopies,"* J. Chem. Phys. **112**, 7775 (2002).

[31] I. I. Smolyaninov, A. V. Zayats, A. Gungor, and C. C. Davis, *"Single-photon tunneling via localized surface plasmons,"* Phys. Rev. Lett. **88**, 187402 (2002).

[32] F. J. García de Abajo, A.G. Pattantyus-Abraham, N. Zabala, A. Rivacoba, M. O.Wolf, and P. M. Echenique, *"Cherenkov effect as a probe of photonic nanostructures,"* Phys. Rev. Lett. **91**, 143902 (2003).

[33] J. Jin, *"The finite element method in electromagnetics,"* 2nd edition, New-York: John Wiley & Sons, 2002.

Chapter 5

Summary and future work

5.1 Summary

Nanoscale resolution cathodoluminescence (CL) has been used to demonstrate and investigate the functionality of potential nanophotonic components based on metallic nanoparticles: phase-change memories and optical antennae.

An integrated experimental setup based on a scanning electron microscope (SEM) was developed for the fabrication, and *in situ* characterization, of nanoparticles (see Chapter 2). The setup was equipped with an effusion cell for gallium nanoparticle growth, a liquid nitrogen cooled cryostat to control sample temperature in the range from 90 to 315 K, and a spectroscopic CL measurement system allowing the acquisition of electron-beam-induced light emission from samples across the wavelength range from 350 to 1150 nm.

Tunable control over the size of gallium nanoparticles, formed by light-assisted self-assembly from an atomic beam, has been demonstrated (see Chapter 2). The experiments revealed a decrease in mean particle diameter (from 68 to 45 nm) with increasing infrared laser intensity (from 160 to 630 $W \cdot cm^{-2}$) during deposition, and the production of larger particles for longer deposition times.

Gallium nanoparticle phase-change memory, where information is recorded into the phase state of individual particles (bits), provides an intriguing possibility to achieve small element size and small writing energy. For the first time, it has been shown that information can be written into the structural phase of bistable gallium nanoparticles by electron beam excitation and readout achieved

via measurements of their CL emission (see Chapter 3). Change of up to 20 % in visible emission intensity is observed following low fluence (≥ 35 fJ/nm^2), electron-beam-induced, solid-to-liquid phase switching of a monolayer of 60 nm particles. This offers a basis for the development of high-density phase-change memories. For example, individual binary (two-phase) elements within a close-packed array of 60 nm particles addressed by an electron beam, could provide a storage density of about 0.2 Tbit/in^2. Developing this concept, selectively electron beam addressed, erasable memory functionality has been demonstrated within a gallium nanoparticle film. Several individual bits of information (each element comprised of less than fifty nanoparticles) were recorded in the structural phase of the gallium nanoparticles using a 20 keV electron beam pulse and readout achieved via measurements of their CL emission in response to a 2 keV electron beam. The calculation of electron beam induced light emission, for homogeneous gallium films and single gallium nanoparticles, qualitatively reproduced the general characteristics observed in the experiments: higher light emission from the liquid gallium phase and emission peak. Finally, the possibility of enhancing CL emission contrast by employing gallium nanoshells, as opposed to homogenous nanoparticles, has been suggested and analyzed numerically.

Optical antennae are expected to become essential elements of future nanophotonic circuits. For the first time, it has been experimentally demonstrated that electron-beam-excited pairs of coupled gold nanorods can act as transmitting optical antennae; *i.e.* they can efficiently convert the energy from a nanoscale source of excitation (created by a focused 40 keV electron beam) into far-field visible radiation (detected by means of CL). Enhanced light emission was observed for electron beam injection points in the vicinity of the junction between coupled nanorods which can be explained by the increased local density of electromagnetic states in that area.

5.2 Future work

Investigation of phase-change memory functionality in metallic nanoparticles may be continued in the following way. Firstly, research work can be directed for the

investigation of new techniques for the fabrication of nanostructured samples. In particular, the fabrication of gallium nanoshells would increase the CL readout contrast greatly (as analyzed numerically in Subsection 3.6). Such nanoshells may probably be obtained by means of the technique of metallic nano-object growth on prepatterned substrates. Secondly, a more detailed study of phase transitions in nanoparticles is important as well. One question to investigate is the dynamics of phase transitions stimulated by ultrashort pump pulses, the probing can be achieved by means of time-resolved CL. That would be helpful for the understanding of phase-change dynamics in nanostructures and for the demonstration of ultimate switching times.

Furthermore, although gallium nanoparticles are a good 'playground' for the investigation of phase-change functionality on the nanoscale, the low temperatures at which the phase transitions occur prevent gallium from being used for commercial applications. Thus, there is a need to search for materials that exhibit a remarkable change of optical properties created by phase transitions but also possess phase-change functionality in nanoparticles closer to room temperature. The desired properties can probably be found in such polymorphic metals as indium or bismuth.

The architecture of nanoparticle phase-change memory is not yet designed. Due to the diffraction limit, the addressing and readout of such a memory cannot be achieved by classical far-field optics. However, a serious investigation is now being performed to solve the problem of light focusing below the diffraction limit. Also, small and inexpensive electron beam addressing devices may probably be created on the basis of the surface-conduction electron-emitter display (SED) technology. Another possibility is to create nanophotonic integrated circuits by embedding switchable nanoparticles into photonic crystal and plasmonic waveguides.

Numerous avenues of investigation may be followed in relation to the demonstrated transmitting optical antennae. For instance, various geometries of optical antennae, based on complex metallic nanostructures, can be explored numerically and experimentally with the purpose of achieving maximized near- to far-field conversion rates, as well as defined directivity and polarizability of light

emission. Another issue to study is surface plasmon dynamics in complex metallic nanostructures, which may be performed by means of time-resolved CL analysis.

Transmitting optical antennas may find a potential application in field-enhanced spectroscopy and as elements of future nanophotonic circuits. In particular, such antennas may control the output of nanolasers to achieve a defined direction and polarization of the radiation.

Appendix A

Sample list

Gallium nanoparticle films

Prepared on cleaved ends of single mode optical fibres (SMF-28)

Sample number	Date of preparation	Conditions and result of sample preparation	Experiments performed with the sample
1	2005/11/24	Not successful: contamination	
2	2005/12/01	Not successful: contamination	
3	2005/12/06	Not successful: contamination	
4	2005/12/07	Not successful: contamination	
5	2005/12/08	Not successful: contamination	
6	2005/12/09	Not successful: contamination	
7	2005/12/10	Not successful: contamination	
8	2005/12/11	Not successful: contamination	
9	2005/12/12	Not successful: contamination	
10	2005/12/13	Not successful: contamination	
11	2005/12/14	Not successful: contamination	
12	2005/12/15	Not successful: contamination	
13	2006/01/14	Not successful: contamination; The SEM effusion cell broke; subsequent samples were prepared in a separate ultra high vacuum chamber and characterized in the SEM	
14	2006/02/20	Ok	Optical pump-probe
15	2006/02/27	Ok	
16	2006/02/28	Ok	

17	2006/03/02	Ok	Electron beam pump, optical probe
18	2006/03/03	Ok	
19	2006/03/04	Ok	
20	2006/03/16	SEM effusion cell repaired; first nanoparticle sample successfully prepared in the SEM (cryostat equipped with a copper cold finger); subsequent samples were prepared and characterized in the SEM	Optical pump-probe
21	2006/03/19	Testing the influence of various deposition parameters on the nature of the nanoparticles grown; Subsequent depositions were performed on fibres coated on the sides with a gold film to provide a conductive path	
22	2006/03/20		
23	2006/03/25		
24	2006/03/26		
25	2006/03/29		
26	2006/04/05		
27	2006/04/07		
28	2006/04/08		
29	2006/04/12		
30	2006/04/25		
31	2006/04/30	Ok	White light transmission through nanoparticle film
32	2006/05/04	Ok	SEM imaging during deposition
33	2006/05/05		
34	2006/05/09	Testing the influence of various deposition parameters on the nature of the nanoparticles grown: - control laser intensity, - presence of the electron beam, - temperature of the effusion cell	
35	2006/05/11		
36	2006/05/13		
37	2006/05/16		
38	2006/05/23		
39	2006/05/25		
40	2006/05/26		
41	2006/05/28		
42	2006/05/29		
43	2006/05/31		
44	2006/06/01		
45	2006/06/03		
46	2006/06/04	Fibre tip kept at room	

47	2006/06/06	temperature; control 1550 nm nanosecond laser; increase of mean particle diameter with increasing laser intensity during deposition	
48	2006/06/08		
49	2006/06/10		
50	2006/06/11		
51	2006/06/12		
52	2006/06/14		
53	2006/06/20		
54	2006/06/22	Fibre tip kept at cryogenic temperature; control 1550 nm nanosecond laser; decrease of mean particle diameter with increasing laser intensity during deposition	
55	2006/06/23		
56	2006/06/24		
57	2006/06/28		
58	2006/07/08	Ok	White light transmission through nanoparticle film
59	2006/08/01	Ok	First results on CL readout of nanoparticle phase state
60	2006/08/08		
61	2006/11/20	Ok	Further CL analysis of nanoparticles
62	2006/12/01	Not successful: high cryostat temperature	
63	2006/12/22	Ok	
64	2007/01/11	Not successful: high cryostat temperature	
65	2007/01/15		
66	2007/02/02	Ok	CL analysis of nanoparticles
67	2007/02/18	Electron beam assisted deposition; increase of mean particle diameter with increasing electron beam intensity	
68	2007/02/27		
69	2007/03/02		
70	2007/03/04		
71	2007/03/18	Ok	CL analysis of nanoparticles
72	2007/03/30	Ok	
73	2007/08/09	Ok	Nanoparticle hysteresis study under nanosecond laser pulses
74	2007/09/12		

75	2007/10/04	Fibre tip kept at cryogenic temperature; control 1550 nm nanosecond laser; increase of mean particle diameter for longer deposition times	Selective electron beam addressing and CL readout
76	2007/10/07		
77	2007/10/10		
78	2007/10/12	SEM effusion cell broke	
79	2008/02/02	SEM effusion cell repaired; Sample preparation not successful: high chamber pressure	
80	2008/02/04		
81	2007/02/05	Fibre tip kept at cryogenic temperature; control 1550 nm nanosecond laser; investigation of the influence of deposition time and fibre tip temperature on nanoparticle growth	Selective electron beam addressing and CL readout
82	2008/02/12		
83	2008/02/14		

Bulk gallium samples

Sample number	Date of preparation	Description	Experiments performed
1	-	mm thick bulk gallium film deposited on a glass substrate	No CL emission change observed for gallium undergoing solid-to-liquid phase transition
2	2007/07/18	mm size gallium droplets on fibre tips	Reflectivity and CL emission change detected for gallium undergoing solid-to-liquid phase transition
3	2007/07/20		
4	2007/07/23		
5	2007/07/31	mm size gallium droplets on the cryostat surface	CL emission changes detected for gallium undergoing solid-to-liquid phase transition
6	2007/08/01		

Gold gratings

Used for the determination of the electron beam spot size

Sample number	Description	Period, nm
1	Gratings in 200 nm gold film on silicon wafers (with 5 nm chromium adhesion layer). Samples prepared by Dr. Y. Chen (Rutherford Appleton Laboratory, UK)	300
2		400
3		500

Gold nanorods

Description	Experiments performed
Gold nanorods on a silicon substrate prepared by Dr. M. D. Arnold and Prof. M. J. Ford (Institute for Nanoscale Technology, University of Technology, Australia)	SEM–CL analysis of single and coupled gold nanorods

Appendix B

Refereed publications

[1] **Transmitting optical nano-antenna.**

A. I. Denisyuk, K. F. MacDonald, N. I. Zheludev, M. D. Arnold, M. J. Ford, and F. J. García de Abajo, *Manuscript in preparation*.

[2] **Towards femtojoule nanoparticle phase-change memory.**

A. I. Denisyuk, K. F. MacDonald, N. I. Zheludev, and F. J. García de Abajo, *Japanese Journal of Applied Physics* **48**(3), 03A065 (2009).

[3] **Luminescence readout of nanoparticle phase state.**

A. I. Denisyuk, K. F. MacDonald, N. I. Zheludev, and F. J. García de Abajo, *Applied Physics Letters* **92**(9), 093112 (2008). Selected for *Virtual Journal of Nanoscale Science & Technology* **17**(11), 2008.

[4] **Emission hotspots in complex metal nanostructures.**

A. I. Denisyuk, G. Adamo K. F. MacDonald, N. I. Zheludev, B. Rodríguez-González, I. Pastoriza-Santos, M. Spuch-Calvar, L. M. Liz-Marzán, M. D. Arnold, M. J. Ford, F. J. García de Abajo, in *Nanometa 2009*, paper WED4f.3.

[5] **High-density nanoparticle phase change memory.**

A. I. Denisyuk, K. MacDonald, and N. I. Zheludev, in *Quantum Electronics and Photonics 18 at Photon08, Abstract book,* p. 156.

[6] **Towards femto-Joule nanoparticle phase-change optical memory.**

A. I. Denisyuk, K. F. MacDonald, and N. I. Zheludev, in *International Symposium on Optical Memory and Optical Data Storage (ISOM / ODS'08)*, paper TD05-32.

[7] **Cathodoluminescence readout of high-density nanoparticle phase change memory.**

A. I. Denisyuk, K. F. MacDonald, and N. I. Zheludev, in *Conference on Lasers and Electro-Optics / Quantum Electronics and Laser Science (CLEO / QELS 2008),* paper QThD1.

[8] **Hyperspectral cathodoluminescent imaging of plasmonic excitations with nanoscale resolution.** (invited)

N. I. Zheludev, M. Bashevoy, A. Denisyuk, and F. Jonsson in *Plasmonics: Nanoimaging, Nanofabrication, and their Applications III at SPIE Optics and Photonics Congress* (2007), paper 6642-05.

[9] **Optical size control in growth of gallium nanoparticles.**

A. I. Denisyuk, F. Jonsson, and N. I. Zheludev in *8th International Congress on Optical Particle Characterization (OPC 2007), Book of Abstracts,* p. 26.

[10] **Phase-change memory functionality in gallium nanoparticles.**

A. I. Denisyuk, F. Jonsson, and N. I. Zheludev in *8th International Congress on Optical Particle Characterization (OPC 2007), Book of Abstracts,* p. 102.

[11] **Phase-change memory functionality in gallium nanoparticles.**

A. I. Denisyuk, F. Jonsson and N. I. Zheludev, in *Conference on Lasers and Electro-Optics/ International Quantum Electronics Conference (CLEO / Europe – IQEC 2007),* paper CC4-4.

[12] **Cathodoluminescence read-out of the structural phase of gallium nanoparticles.**

A. I. Denisyuk, F. Jonsson, and N. I. Zheludev, in *International Conference on Coherent and Nonlinear Optics / International Conference on Lasers, Applications, and Technologies (ICONO / LAT 2007),* paper I10/III-4.

[13] **Optimization of optical size control in gallium nanoparticle growth.**

A. I. Denisyuk, F. Jonsson, and N. I. Zheludev in *International Conference on Coherent and Nonlinear Optics / International Conference on Lasers, Applications, and Technologies (ICONO / LAT 2007),* paper I02/VII-4.

[14] **Dynamic structural equilibrium in self-assembled nanoparticles at the fiber tip: probing with second harmonic generation.**

B. F. Soares, F. Jonsson, K. F. MacDonald, A. I. Denisyuk, and N. I. Zheludev in *Quantum Electronics and Photonics 17 at Photon06, Abstract book,* p. 148.

[15] **Nonlinear optical interactions in mixed-state metal nanoparticles undergoing a structural transformation.**

B. F. Soares, F. Jonsson, K. F. MacDonald, A. I. Denisyuk, and N. I. Zheludev in *Plasmonics: Metallic Nanostructures and their Optical Properties IV at SPIE Optics and Photonics* (2006), paper 6323-71.

[16] **Nanophotonics under a scanning electron microscope: studying resonator-less all-optical switching and memory functionality in gallium nanoparticles.** (invited)

K. F. MacDonald, M. V. Bashevoy, A. I. Denisyuk, F. Jonsson, B. F. Soares, and N. I. Zheludev in *Conference on Lasers and Electro-Optics / Quantum Electronics and Laser Science (CLEO / QELS 2006),* paper QTuJ2.